DEVELOPMENT OF A PARACORPOREAL RESPIRATORY ASSIST LUNG (PRAL)

by

Robert George Svitek

B.S. in Bioengineering, University of Pittsburgh, 2000

Submitted to the Graduate Faculty of

the School of Engineering in Partial Fulfillment

of the Requirements for the degree of

Doctor of Philosophy

University of Pittsburgh

2006

UNIVERSITY OF PITTSBURGH

SCHOOL OF ENGINEERING

This dissertation was presented

by

Robert G. Svitek

It was defended on

June 6, 2006

and approved by

Harvey S. Borovetz, PhD, Professor

William R. Wagner, PhD, Professor

Brack G. Hattler, MD, PhD, Professor

William J. Federspiel, PhD, Professor

Dissertation Director: William J. Federspiel, PhD, Professor

DEVELOPMENT OF A PARACORPOREAL RESPIRATORY ASSIST LUNG

Robert G. Svitek, PhD

University of Pittsburgh, 2006

A Paracorporeal Respiratory Assist Lung (PRAL) was developed for supplemental gas exchange to allow the native lungs of acute lung failure patients time to heal. The device consisted of a rotating annular microporous hollow fiber membrane bundle. The rotation augmented the gas exchange efficiency of the device at constant flowrate thereby uncoupling gas exchange and flowrate. The rotating fibers also enabled the PRAL to pump the blood without the need for an additional pump or arterial cannulation. A prototype was manufactured with an overall surface area of 0.42 m^2, and CO_2 removal rates were 101 ml/min at a blood flowrates of 0.75 L/min. When rotated at 1500 RPM, CO_2 removal increased by 92 % and O_2 transfer increased by 88% over the stationary bundle during an in vitro bovine blood study. The pumping of the rotating fiber bundle was assessed, and at 1500 RPM the PRAL generated 750 ml/min against 52 mmHg pressure in water. Hemolysis of the device was assessed using in vitro bovine blood from a slaughterhouse. Plasma free hemoglobin levels were higher than the control, and we found that the roughness of the rotating fibers was the cause of much of the blood trauma.

TABLE OF CONTENTS

LIST OF TABLES

LIST OF FIGURES

PREFACE

I would like to thank my thesis advisor and mentor Dr. William Federspiel for the opportunity to work in the Medical Devices Laboratory. His guidance has taught me how to solve challenging engineering problems by formulating mathematical models to understand the physics of the problem and also by teaching me how to design and execute experiments. He has also provided me the opportunity to gain valuable industrial experience by allowing me to collaborate with Alung Technologies, Inc. during the initial research and development phase of the commercialization of the PRAL. I hope that the work presented here will be a valuable contribution to the future work performed at the Medical Devices Laboratory.

I would also like to thank my committee members Dr. Harvey Borovetz, Dr. William Wagner, and Dr. Brack Hattler who devoted their time to help guide this research. Their expertise spans many years of research and development on oxygenators at the University of Pittsburgh. I was very fortunate to have an advisor and committee members that are regarded as the experts in the field.

I am very appreciative of all the people that have helped me along the way at the Medical Devices Laboratory. The lab has always maintained a spirit of cooperation across the various projects, and the input from others was helpful in analyzing results from a different perspective. I wish everybody at the lab the best of luck in achieving his or her future goals.

Finally, I would like to thank my wife Gennifer who has supported and encouraged me during college and graduate school. Her patience and understanding has allowed me to focus on a career that I hope will be very rewarding as we begin our family. I look forward to a happy and exciting future.

This work was funded by the Commonwealth of Pennsylvania, the National Tissue Engineering Consortium (NTEC), U.S. Army Medical Research and Material Command Grant Number DAMD17-02-0717, and also by National Institutes of Health (NIH), the National Heart, Lung, and Blood Institute (NHLBI) Grant Number RO1 HL70051.

1.0 BACKGROUND

1.1 INTRODUCTION

Lung disease is the number three killer in America and is responsible for nearly 350,000 deaths every year [1]. The current treatment of lung disease utilizes mechanical ventilation, which can lead to further lung damage due to high pressure and volume delivered to the lungs. An alternative treatment utilizes an artificial lung to supply O_2 and remove CO_2 to enable the lungs of the patient to heal. This chapter describes a prevalent lung disease, Chronic Obstructive Pulmonary Disease (COPD), and the current treatments that utilize mechanical ventilation or a membrane oxygenator. The basic principles of gas exchange in a membrane oxygenator are described and current applications of the membrane oxygenator are also discussed. The objective of this project is to develop a self-pumping, highly efficient membrane oxygenator and the basic goals of the project are described in this chapter.

Chronic Obstructive Pulmonary Disease (COPD) is a lung disease characterized by airflow obstruction, dyspnea, and increased blood CO_2 content and affects approximately 4%-10% of adults [2]. In 1998, almost 662,000 hospitalizations were attributed to COPD, and 2,530,000 hospitalizations (7.0% of total hospitalizations) had COPD listed as a contributing cause of the hospitalization. The estimated direct medical costs in 1993 for treating COPD were $14.7 billion. Deaths associated with COPD have

increased steadily in the United States over the past 20 years, and in 1998 over 105,000 people died from COPD [3]. Death rates for COPD have continued to increase without regard to sex or race in the United States from 1960 to 1992 [4] (Figure 1.1).

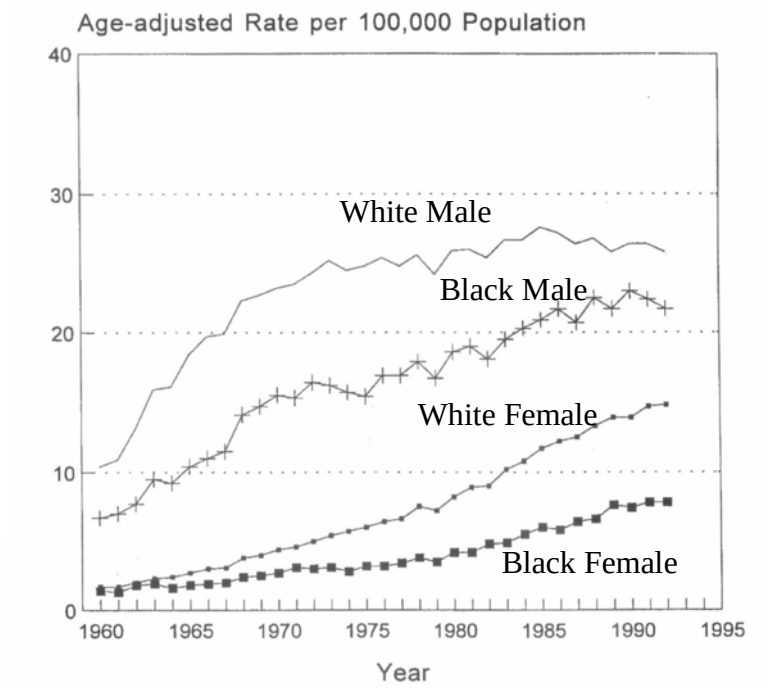

Figure 1.1: Number of deaths per 100,000 caused by COPD from 1960-1992 [4].

Acute exacerbations of COPD are caused by bacterial and viral infection, pollution, and environmental temperature changes [5]. The exacerbations are associated with increased breathlessness accompanied by cough and sputum production. Blood pH is one marker of the severity of the exacerbation and is accompanied by a rise in arterial CO_2 levels. Warren et al found that a pH < 7.26 was linked to a poor prognosis and death was associated with increasing age and a low pH [6]. On average, patients requiring medical treatment with COPD have three acute exacerbations per year [7].

Acute exacerbations may be reversible if the lungs can be temporarily supported and allowed to heal [8-12]. Severe exacerbations are associated with respiratory failure and hospital admission. Recently, non-invasive ventilation (NIV) has been explored as a treatment regimen for acute exacerbations, but often fails to return pH and arterial CO_2 to normal levels [13]. Inhaled corticosteroids and bronchodilators are being investigated to reduce exacerbations in patients with COPD, but have yet to demonstrate increased survival over the long term [10].

The most common treatment for severe acute exacerbation of COPD is invasive mechanical ventilation, involving patient sedation and intubation. Mechanical ventilation delivers oxygen to the lungs using high volumes and pressures to achieve adequate gas exchange. The increased volume and pressure causes increased expiratory muscle recruitment and increased work of breathing [8]. The additional workload on the lungs causes inflammation, mucous plugging, and bronchospasm that increase the workload further [11]. The cycle continues as the condition of the patient worsens and often results in multi-organ failure and death [5]. One study found that barotraumas, damage to the lungs due to high-pressure ventilation, developed in 19% of patients with COPD, treated with mechanical ventilation [14]. Mechanical ventilation is uncomfortable and painful resulting in poor sleep cycles, which may prolong ventilator time and costs [11]. These conditions cause alveolar damage, which further aggravates the respiratory insufficiency in many patients and results in unsuccessful therapy.

The goal of mechanical ventilation is to temporarily supply oxygen and remove carbon dioxide to allow the lungs to rest and return to spontaneous breathing. The survival rate of patients treated with mechanical ventilation is inversely correlated with

the amount of time spent on the ventilator [15]. Chances for successful therapy increase the sooner the patient can be extubated and returned to unassisted breathing. Premature extubation followed by reintubation has been associated with increased mortality (27% versus 2.6% if successfully extubated) [15]. The length of time a patient spends on a ventilator is crucial for determining the outcome of the therapy, and optimized weaning protocols have yet to be established. Increased time spent on the ventilator also increases the risk of developing nosocomial pneumonia. Ventilator-associated pneumonia causes higher medical costs and prolonged hospitalization [16]. Heyland et al. found that patients who developed ventilator-associated pneumonia spent an average of 4.3 days longer than patients who did not develop pneumonia [17]. Several other studies have suggested that mortality attributable to ventilator-associated pneumonia is greater than 20% [18].

1.2 PRINCIPLES OF GAS EXCHANGE IN BLOOD OXYGENATORS

An alternative treatment to mechanical ventilation employs a blood oxygenator (artificial lung) to assist gas exchange and to help restore respiratory function while alleviating the complications with mechanical ventilation. The therapy relies on implementation of the oxygenator through intravascular [19-23], intrathroacic [24-26], or paracorporeal [27-29] placement of the device. The latest technology in blood oxygenator design exchanges O_2 and CO_2 through microporous, hollow fiber membranes potted together in a bundle configuration. Figure 1.2 is a picture of a commercially available oxygenator (Capiox, Terumo Cardiovascular Systems, Ann Arbor, Michigan) and a microscopic

view of the hollow fiber membrane bundle that provides the gas exchange ability of the device. Pure O_2 or air flows through the lumens of the fibers and blood flows around the outside of the fibers.

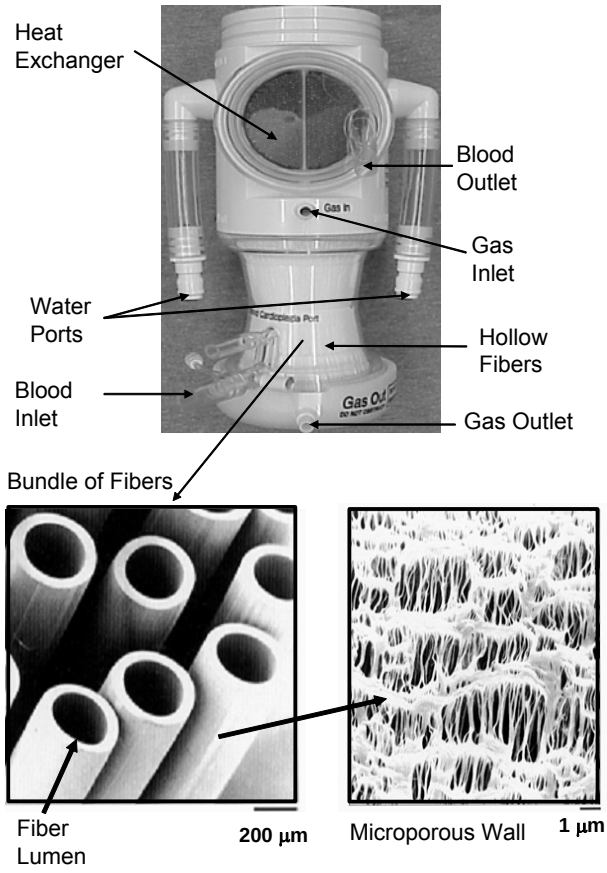

Figure 1.2: Commercially available membrane oxygenator (top); bundle of hollow fiber membranes (bottom left); microporous structure of fibers (bottom right).

Oxygen exchange is determined by the fiber bundle geometry and surface area, gas side partial pressure, hemoglobin concentration, and blood flowrate. Oxygen diffuses from the fibers where the pO_2 is high, into the blood where the pO_2 is low. Oxygen binds to hemoglobin until full saturation, and any excess O_2 is dissolved into the plasma. The rated flow of an oxygenator is a term used to describe the minimum flowrate at which

blood can enter the device with 75% hemoglobin saturation and leave the oxygenator with 100% hemoglobin saturation [30].

Carbon dioxide is removed from the blood where the concentration of CO_2 is high, into the fibers where it is swept away by the low CO_2 concentration gas within the fibers (Figure 1.3). Carbon dioxide exchange is determined by the fiber bundle geometry and surface area, gas side partial pressure, and blood flowrate. CO_2 is transported in the blood as dissolved CO_2, CO_2 bound to hemoglobin, and bicarbonate [31]. Due to the higher storage capacity of blood for CO_2 than O_2, CO_2 exchange is less dependent on blood flowrate than O_2 exchange. At the rated flow, the CO_2 removal rate exceeds the O_2 delivery rate for blood oxygenators that use microporous hollow fiber membranes.

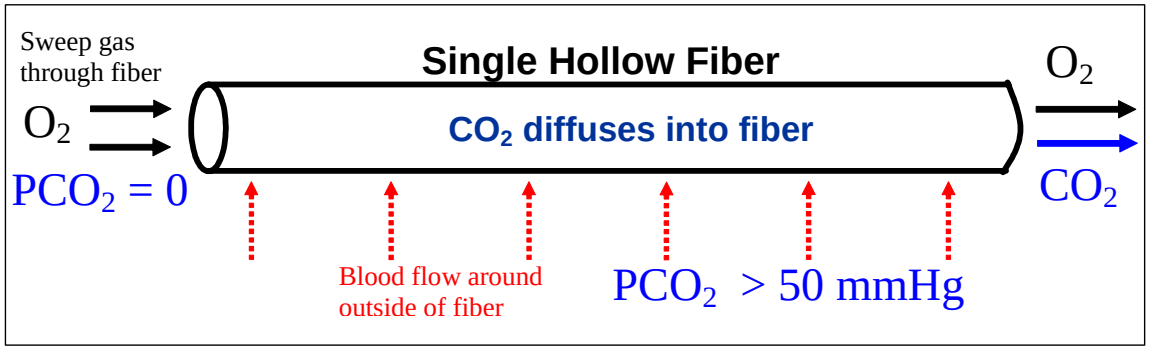

Figure 1.3: A schematic of CO_2 removal in a single fiber within an artificial lung. CO_2 diffuses along its gradient into the fiber where it is swept away.

Gas exchange in blood oxygenators is determined by the relative mass transfer resistances of the gas inside the fibers, the fiber membrane wall, and on the blood side of the fibers. For microporous oxygenators, the resistance of the gas and the membrane are negligible [32]. The blood side mass transfer resistance is due to a concentration boundary layer near the outer fiber wall that results from blood flow around the fibers.

The kinematic viscosity and the velocity of the blood are key factors that determine the size of this boundary layer. A detailed analysis of the equations governing mass transfer in membrane oxygenators is described in Chapter 9. Commercially available artificial lungs are passive, i.e. they have stationary fibers mandating the velocity of the blood to be directly dependent on the flowrate through the device. Therefore, fiber bundle surface area is increased until adequate gas exchange can be achieved at a given flowrate.

1.3 CO_2 REMOVAL DEVICES

The blood oxygenator can be intracorporeal or extracorporeal. Intravenous devices are a subset of intracorporeal devices and are designed to be inserted into a vein through a surgical or percutaneous incision in the leg. The IVOX was one such intravascular device that underwent human clinical trials in the mid 1990s [33]. The IVOX was capable of removing 30% of CO_2 production in a normocapnic adult, but human clinical trials were halted when the gas exchange levels were deemed insufficient. The Hattler Catheter (HC) is another intravascular oxygenator that is in development and awaiting clinical trials. Like the IVOX, the HC is inserted through the femoral vein into the vena cava. The HC employs a centrally located pulsating balloon that increases the mixing of blood around the fibers to enhance gas exchange 50-300% above a non-pulsating device [19]. The highly integrated membrane oxygenator (HIMOX) is another intravascular gas exchange device that incorporates a pump within the bundle to help move blood across the fibers. This technology is in the early phases of development

and current research focuses on the insertion and deployment of the device [34-36]. Intravascular blood oxygenators have limited gas exchange ability because the restriction of vessel size limits the surface area of the device. Intravascular oxygenators also suffer from limited patient mobility [37, 38].

Extracorporeal CO_2 removal (ECCO2R) was tested in the late 1970s by Kolobow and Gattinoni [39-48] This technique incorporated mechanical ventilation and a blood oxygenator to supplement the CO_2 removal. The blood was taken from the patient and passed through a pump, artificial lung, and heat exchanger. A simplified version of ECCO2R is arteriovenous CO_2 removal (AVCO2R), in which the pump is eliminated in place of an arterial cannulation and low resistance hollow fiber membrane oxygenator. The arteriovenous pressure gradient drives blood through the oxygenator at a flowrate proportional to the arteriovenous gradient and inversely proportional to the resistance of the oxygenator and cannula. AVCO2R was tested in an acute animal model of ARDS and demonstrated the ability to remove 100-200 ml/min of CO_2 [29, 49, 50] at flowrates of 0.75-1.5 L/min. Studies of AVCO2R recently expanded into human clinical trials [50, 51]. Mechanical ventilation parameters such as tidal volume, minute ventilation, and peak pressure were reduced as a direct result of the low flow CO_2 removal of AVCO2R. This technology is currently being commercialized by a German based company called Novalung [52, 53]. AVCO2R has several drawbacks. The arterial cannulation can lead to blood loss due to the high arterial blood pressure in the vessel in combination with the anticoagulated patient. Another drawback is the large surface area (2.5 m^2) required by the oxygenator to provide adequate gas exchange [54, 55]. The large surface area can lead to thrombosis in areas of stagnation, and neutrophil activation related to

adsorbed proteins and shear forces [56-59]. Reducing the surface area of the membrane oxygenator is possible by increasing the gas exchange efficiency of the device. This increased efficiency can be achieved by incorporating active mixing into the membrane oxygenator, such as a pulsating balloon [19, 20, 60-62] or a rotating fiber bundle [63].

In this project, we propose to design a system that improves upon the clinical success of AVCO2R by eliminating the arterial cannulation and eliminating the dependence on the patient arteriovenous pressure gradient to provide flow. The design objectives of the system are:

1) CO_2 removal rates of 100-120 ml/min at a blood flowrate of 0.75 L/min or less.
2) Fiber membrane surface area less than 0.5 m^2.
3) Priming volume less than 300 ml.
4) Generate pumping pressure of 80-100 mmHg at a flowrate of 0.75 L/min to enable percutaneous insertion of a dual lumen venous cannula.
5) In vitro hemolysis levels comparable to a commercially available oxygenator.

The proposed system is envisioned to provide CO_2 removal to allow the native lungs time to heal. The low flowrate and priming volume of the system are targeted to create an approach that can be implemented as easily as acute hemodialysis. To achieve these objectives, the device incorporates a rotating fiber bundle to increase the gas exchange efficiency above that achieved with commercially available passive oxygenators. The rotating fiber bundle also generates pressure to facilitate pumping, which enables a percutaneous insertion of a dual lumen venovenous cannula.

This thesis describes the design and development of the Paracorporeal Respiratory Assist Lung (PRAL). A model of CO_2 removal versus flowrate is provided in Chapter 2 to show feasibility of removing 100-120 ml/min of CO_2 at flowrates less than 0.75 L/min. Chapter 2 also describes other oxygenator technologies that have utilized rotation to enhance gas exchange. Finally, detailed drawings and the manufacturing procedures for building PRAL prototypes is provided.

Chapter 3 discusses the gas exchange and pumping results for each PRAL prototype. The gas exchange was tested in water for all prototypes and in blood for the Generation III design. The pumping was tested in water and a glycerol-water blood analogue solution. We investigated uniform radial flow in the PRAL fiber bundle in Chapter 4. A model was developed to predict gas exchange in the different PRAL prototype designs. This model is discussed in Chapter 5. A technique called selective perfusion was used to measure gas exchange in localized regions of the fiber bundle in each prototype. The model predicted that gas exchange increases with porosity of the fiber bundle. Chapter 6 shows the model predictions and then describes how 3 fiber bundles were manufactured with increased porosity. Gas exchange efficiency was measured in water for each bundle. Chapter 7 covers the experimental hemolysis of the PRAL and Chapter 8 discusses calculations of shear stress due to the rotating fiber bundle. Chapter 9 is a theoretical model of CO_2 exchange in hollow fiber oxygenators. The theory is tested on two different fiber bundle designs.

2.0 PARACORPOREAL RESPIRATORY ASSIST LUNG (PRAL)

2.1 INTRODUCTION

The goal of this project is to develop a Paracorporeal Respiratory Assist Lung (PRAL) to provide CO_2 removal at a low blood flowrate for the treatment of respiratory failure, particularly acute exacerbations of COPD. A representation of the PRAL connected to a patient is shown in Figure 2.1. The PRAL is comprised of an annular hollow fiber membrane bundle that is rotated to increase the gas exchange efficiency of the device and pump blood. A percutaneous dual lumen cannula, which is inserted through the femoral vein and placed into the vena cava, provides blood flow to and from the PRAL.

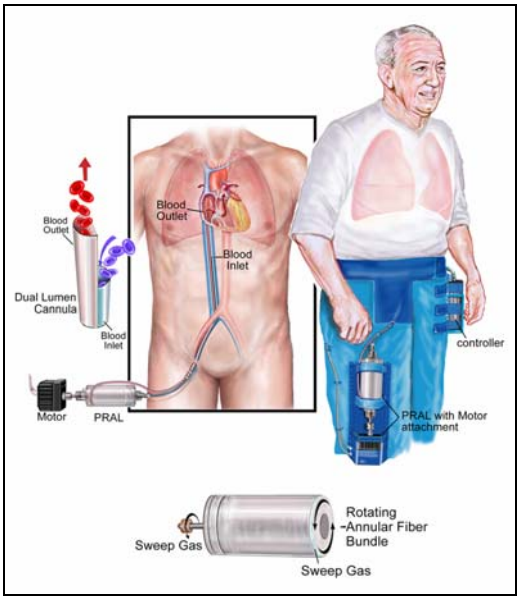

Figure 2.1: Schematic of PRAL connected to patient.

The rotating fiber bundle provides several distinct advantages over current passive (i.e. no mechanical motion), oxygenators like that used in AVCO2R (see Chapter 1). Gas exchange can be augmented by increasing the fiber bundle rotation rate while maintaining a constant low blood flowrate. Passive oxygenators depend on increased flowrate to achieve higher levels of gas exchange. The increase in gas exchange efficiency due to rotation also enables a lower membrane surface area than that required by passive oxygenators. The reduction in surface area leads to decreased platelet activation and reduced thrombosis due to surface-related effects [55]. Additionally, the rotating fiber bundle generates pumping pressure to enable cannulation from the venous side without the need for an arterial cannulation. Unlike the PRAL, the passive oxygenators used in AVCO2R require a separate pump, or rely on the arteriovenous pressure gradient of the patient, to provide flow through the device. Venous cannulation of the PRAL may reduce the inherent blood loss and bleeding risks associated with arterial cannulation [55].

The following sections give a summary of previous work on oxygenators that implement rotation to provide gas exchange enhancement and pumping ability. Also, the methods for building PRAL prototypes used in this research are described. The gas exchange and pumping performance of the prototypes is described in Chapter 3.

2.2 ROTATION IN OTHER OXYGENATOR TECHNOLOGIES

Several investigators in the 1970s used rotation to increase gas exchange in artificial lungs made from flat microporous membrane sheets [64-66]. These devices were large in size due to the inherently low gas exchange surface area to blood volume ratio of membrane sheets. Other investigators have attempted to use rotation in disk shaped oxygenators, but the devices exhibited high hemolysis levels due to their complex construction and operation [67-69]}.

Gaylor fabricated the Taylor-Vortex oxygenator in the mid 1970s, a device with enhanced gas exchange as a function of rotation [64]. This device was composed of a rotating inner cylinder and stationary outer housing, both lined with sheets of microporous membranes. Oxygen gas exchange efficiency in blood was 240 ml/min/m^2 for a 0.3 m^2 device at 5 LPM blood flow. Although this efficiency was considerably higher than passive artificial lungs at the time, the device was 25 cm in diameter and 63 cm in length, which resulted in an inordinately large device.

Makarewicz and Mockros [70] manufactured a pumping artificial lung (PAL) by rotating an annular bank of hollow fiber membranes within the housing of a modified Biomedicus BP-80 pump head. The 0.6 m^2 device exhibited CO_2 transfer efficiencies of 37-120 ml/min/m^2 from 1-5 LPM blood flow and generated 1.0 LPM flow against 100 mmHg pressure at 1500 RPM. Unlike the Taylor-Vortex oxygenator, gas exchange was independent of rotation rate [22]. Thus, gas exchange enhancement was only achieved by increasing the flowrate through the artificial lung. The concept of a rotating fiber bundle to increase gas exchange in an artificial lung was patented in 1999 by Dr. James

Maloney [71]. In vivo gas exchange in a dog produced O_2 exchange of 40 ml/min at 200 RPM to 60 ml/min at 600 RPM. The rotating fiber bundle also generated pumping pressure eliminating the need for a separate pump.

Wu et al. [72] described a rotating disk oxygenator that enhanced gas exchange with rotation and pumps with the intent of ambulatory respiratory support for 21 days for adults. A 0.50 m^2 prototype exhibited CO_2 exchange efficiency of 370 ml/min/m^2 in blood at 5 L/min. The device pumped to pressures of 400 mmHg at 5 L/min at a rotation rate of 2000 RPM. Hemolysis caused by rotation was comparable to ventricular assist devices (VAD) with a normalized index of hemolysis (NIH) of 0.068 g/100L. This technology is being developed by a company called Ension, Inc., and another application of the rotating disk oxygenator is to provide cardiopulmonary support in the pediatric patient population [73].

CardioVention, Inc. commercialized the CORx™ integrated cardiopulmonary bypass circuit. This system was comprised of a passive oxygenator combined with a centrifugal pump into one compact unit, roughly the size of a can of soda. This device also incorporated an air elimination technology. The artificial lung was composed of microporous polypropylene hollow fibers with a total surface area of 1.2 m^2. The compact nature of the system led to reduced hemodilution of the patient and less overall foreign surface-blood contact. An in vivo study in calves showed that the CORx system exhibited better gas exchange, more constant hematocrit, and comparable hemolysis to a standard oxygenator during a 6 hour period [74]. The disadvantage of this system and any other system that integrates a separate pump with a bundle of hollow fibers was the passive nature of the device. The only way to increase the relative velocity between the

fibers and the blood in the CORx was to increase the overall flowrate through the device.

2.3 FEASIBILITY OF LOW FLOW CO_2 REMOVAL

We investigated the possibility of removing 100-120 ml/min of CO_2 at flowrates of less than 750 ml/min by developing a model based on the CO_2 dissociation curve in blood. CO_2 elimination by the membrane oxygenator can be calculated as: $VCO_2 = Q_b(C_{in} - C_{out})$ where VCO_2 is the carbon dioxide removed from the blood by the oxygenator (ml CO_2/min), Q_b is the flowrate of blood through the oxygenator (ml blood/min), C_{in} is the concentration of CO_2 coming into the oxygenator (ml CO_2/ml blood), and C_{out} is the concentration of CO_2 in the blood leaving the oxygenator (ml CO_2/ml blood). Carbon dioxide is present in the blood in the form of dissolved CO_2, bicarbonate ions (HCO3), and CO_2 bound to hemoglobin. The concentration can be expressed in terms of the partial pressure through an empirical relationship of the CO_2 dissociation curve [31]: $C = 0.11489 P_{CO2}^{0.3773}$ (C is the concentration in ml CO_2/ml blood; P_{CO2} is the partial pressure in mmHg). Using these relationships, the CO_2 removal rate as a function of blood flowrate was plotted for different outlet CO_2 partial pressure (Figure 2.2). At a blood flowrate of 400 ml/min or greater, 100-120 ml/min of CO_2 can be removed, leaving the pCO_2 in the blood exiting the oxygenator at 10 mmHg or greater.

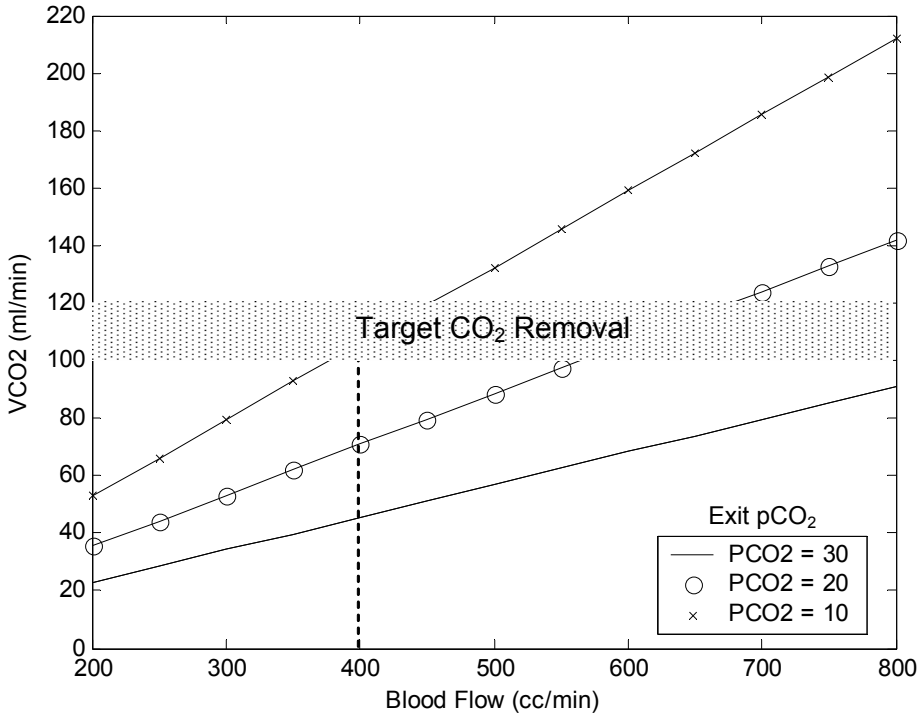

Figure 2.2: CO_2 removal versus flow rate at different inlet CO_2 concentrations.

The model predicted that the target CO_2 removal can be achieved at flowrates as low as 400 ml/min. Three generations of PRAL prototypes were then manufactured and tested.

2.4 MANUFACTURING PRAL PROTOTYPES

The rationale for each PRAL prototype design was based on experimental gas exchange results, which are described in Chapter 3. The fiber bundles for each design were annular in shape and the ends of the bundle were made to enable gas flow by gluing the bundle of fibers together in a 1 cm annular ring and toming the ends of the fibers to allow gas to flow through the lumens of the fibers. The procedure of gluing and toming the fibers is known as ‘potting’ the bundle. The glued part of the fiber bundle is

known as the fiber bundle 'potting'. The first generation PRAL prototype consisted of a rotating fiber bundle that was potted directly to a rotating diffuser. The second generation consisted of a stationary fiber bundle with a rotating diffuser in the center of the bundle. The third generation consisted of a rotating fiber bundle with a stationary diffuser. Table 2-1 summarizes the three PRAL generations and their dimensions.

Table 2-1: Description of PRAL Generations.

	Generation I	Generation II	Generation III
Mode of Rotation	**Rotating Fibers/ Rotating Diffuser**	**Stationary Fibers/ Rotating Diffuser**	**Rotating Fibers/ Stationary Diffuser**
Surface Area (m2)	0.42	0.42	0.42
Fiber Bundle Outer Diameter (cm)	7.0	7.0	7.0
Fiber bundle Thickness (cm)	1.0	1.0	0.2
Number of Fiber Layers	25	25	7
Fiber Bundle Length (cm)	4.0	4.0	13.0
Number of Fiber Bundle Designs	1	1	5
Number of Diffuser Designs	2	1	3

2.4.1 Generation I

Generation I prototypes had a rotating fiber bundle and diffuser. The complete Generation I prototype is shown schematically in Figure 2.3 and the actual prototype is shown in Figure 2.4. Blood entered the center of the device through a 3/8" custom barb inlet, was channeled radially across the bundle by the diffuser, and exited a 3/8" barb connector. The gap between the bundle and outer housing was 6 mm. Gas flowed

through a luer fitting at the blood inlet side of the device. Two roller bearings (P/N R6, MSC Industrial Direct Company Inc., Melville, NY) were located at the motor end of the housing and were used to enable rotation and maintain concentricity. An additional roller bearing was at the inlet side of the device inside the housing end cap. Four seals prevented blood from entering into the gas pathway. At the interface of blood and gas, a 3/8" ID rubber double lip seal was used (P/N 6119, Chicago Rawhide, Chicago, IL). Between the bearings, a ¼" single lip seal was used (P/N 711803, Chicago Rawhide, Chicago, IL).

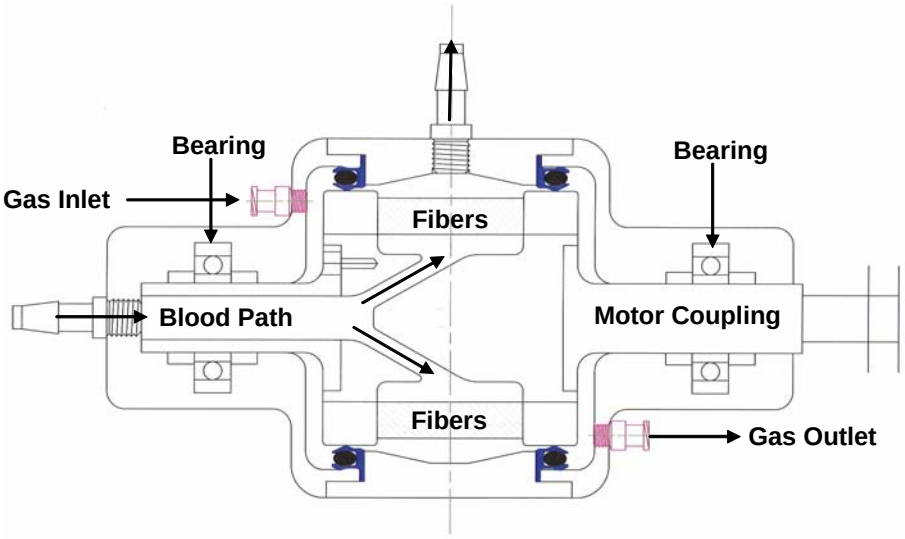

Figure 2.3: Drawing of Generation I PRAL device.

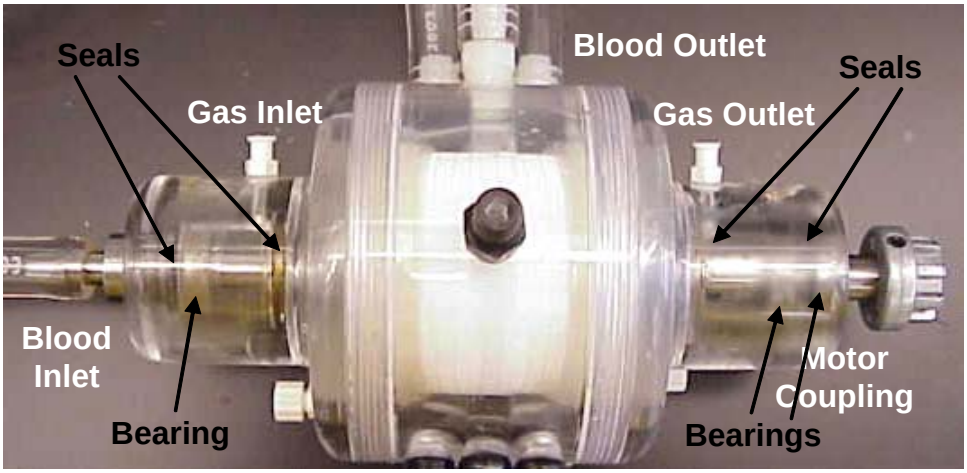

Figure 2.4: Generation I PRAL prototype.

Fiber bundle prototypes were manufactured by wrapping fiber fabric around the diffuser that was coupled directly to the rotating shaft of the motor. Two diffusers were manufactured; the Four hole diffuser had four 5 mm holes located 90° apart, and the Even diffuser had 5 rows of 3.5 mm holes located 22.5° apart (Figure 2.5). Once wrapped, the fibers were potted to the outer edge of the diffuser using a two-part polyurethane adhesive (Cas Chem, Bayonne, NJ), which was injected into a Delrin™ (DuPont) potting fixture. The potted fibers were then tomed in a custom fixture to open the ends of the fibers for gas flow through a common manifold. Two acrylic endcaps having the same diameter as the fiber bundle were placed over the fiber bundle ends, the rotating shaft, and the blood inlet. The endcaps provided a barrier between the blood and gas pathways. The endcaps were attached to the bundle using rubber sleeves that stretched over the bundle and end cap assembly. The rubber sleeves were made by dipping a custom mandrel into polyurethane. The seals (P/N 6119, Chicago Rawhide, Chicago, IL) separating the blood and gas pathways were then placed into the housing endcaps, and this assembly was tested for leaks between the pathways.

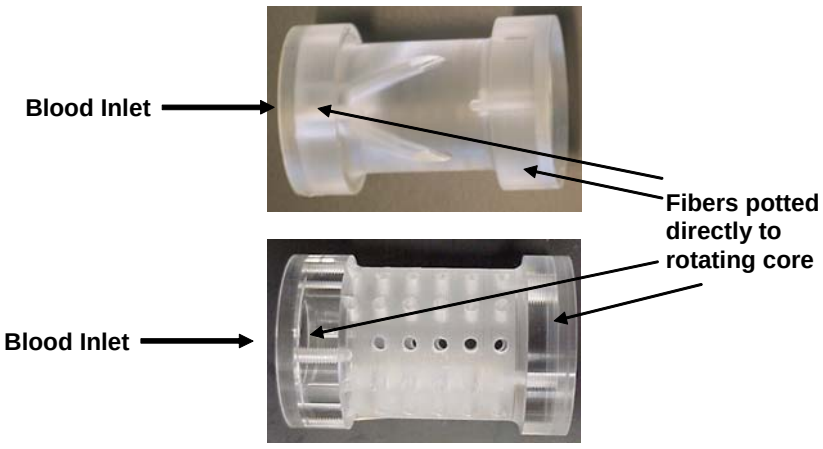

Figure 2.5: Generation I PRAL center diffusers. Top: Four hole diffuser. Bottom: Even diffuser.

2.4.2 Generation II

Generation II had a rotating diffuser and stationary fiber bundle (Figure 2.6 & Figure 2.7). Fiber bundle prototypes were manufactured by wrapping the fiber fabric around two acrylic caps, which allowed the rotating diffuser to be screwed into the center of the bundle. Once wrapped, the fibers were potted using the same fixture and methods described for Generation I. The blood and gas pathways were separated using two Teflon rings (Part X201133, Bal Seal Engineering Company, Inc, Foothill Ranch, CA) that sealed the stationary fiber bundle and outer housing. The acrylic diffuser coupled directly to the shaft that rotated the bundle and contained four slits that channeled flow across the bundle. The blood inlet passed into the rotating core through a rubber single lip seal (P/N 711803, Chicago Rawhide, Chicago, IL).

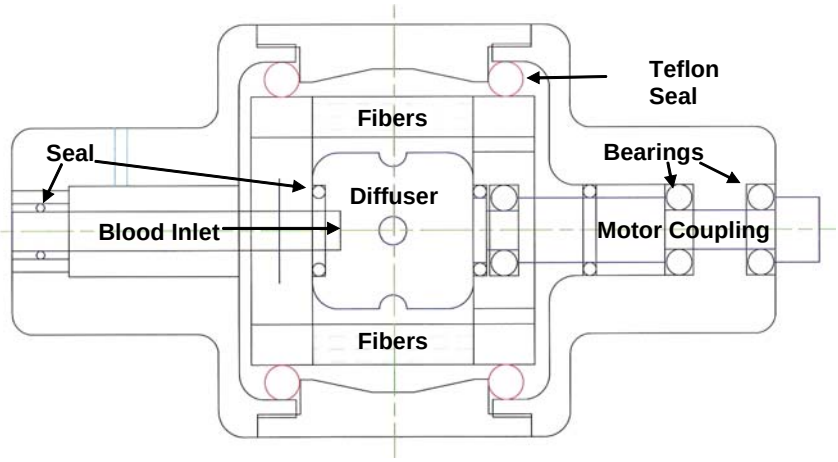

Figure 2.6: Drawing of Generation II PRAL device.

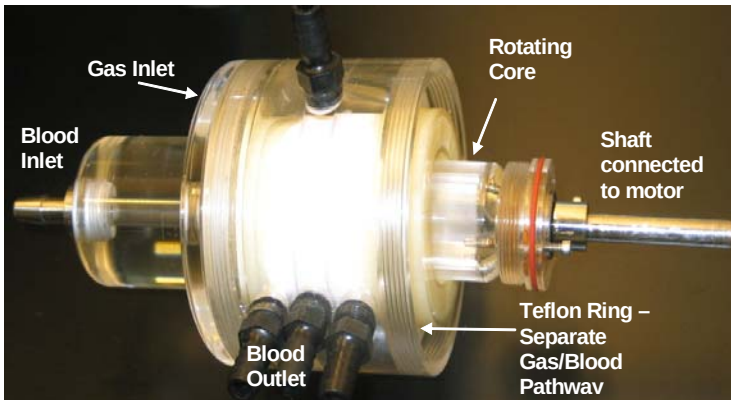

Figure 2.7: Generation II PRAL prototype.

2.4.3 Generation III

Generation III had a rotating fiber bundle with a stationary core. A schematic of Generation III is shown in Figure 2.8 and Figure 2.9, and a picture of the prototype is shown in Figure 2.10. Fiber bundles were manufactured by wrapping the fiber fabric around a cage support structure that enabled rotation of the bundle without applying torque to the fibers. The cage structure coupled directly to the shaft that rotated the

bundle. Two different support structures were manufactured. One was a strut cage, and the other was a porous cage (see Figure 2.11). The strut cage was made by soldering 1.5 mm stainless steel rods to a stainless steel ring (O.D. 6.6 cm) to which the fiber bundle was potted. Once wrapped, the fibers were potted to the support structure using a two-part polyurethane adhesive (Cas Chem, Bayonne, NJ) injected into a DelrinTM (DuPont, Wilmington, DE) potting fixture. The potted fibers were then tomed in a custom fixture to open the ends of the fibers for gas flow through a common manifold. The potted bundle was placed over the stationary diffuser. A threaded cap provided a blood-gas barrier between the bundle and the diffuser. The same acrylic endcaps as in Generation I were placed over the fiber bundle ends onto the threaded cap, but over the rotating shaft and blood inlet. The endcaps provided a barrier between the blood and gas pathways. The endcaps were attached to the bundle using sleeves that stretched over the bundle and end cap assembly. The sleeves were made by dipping a custom mandrel into polyurethane. The stationary core was screwed to the blood inlet which was fixed into the upstream end cap with a 0.50" set screw. The bundle assembly was then placed into the outer housing and end-caps were screwed to the housing.

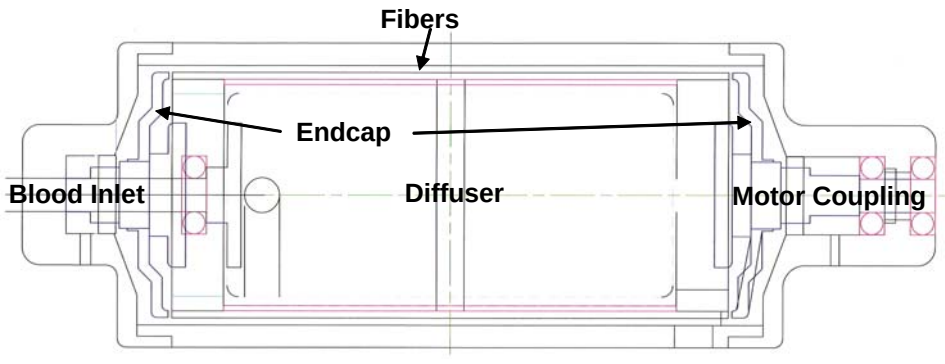

Figure 2.8: Drawing of Generation III PRAL device.

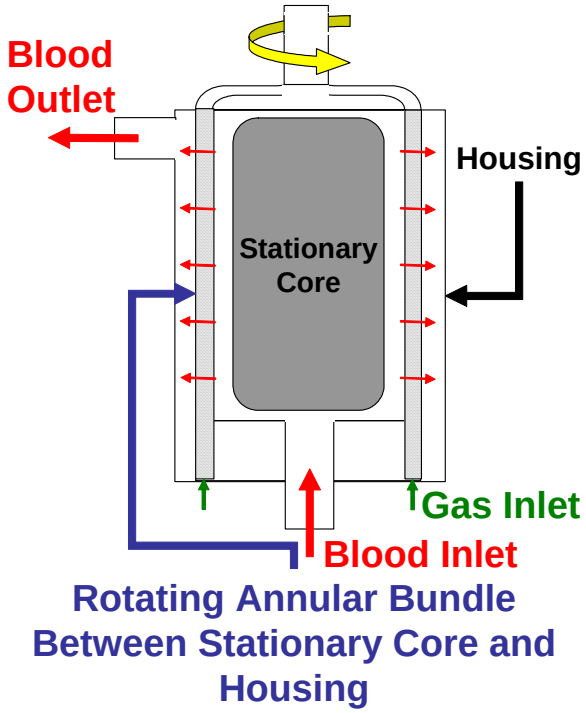

Figure 2.9: Schematic of Generation III PRAL.

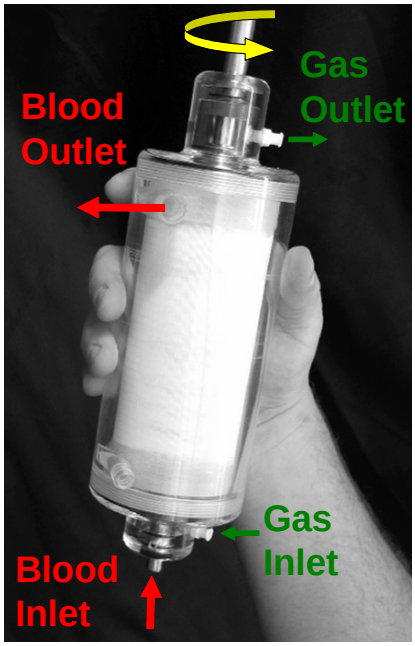

Figure 2.10: Generation III PRAL prototype.

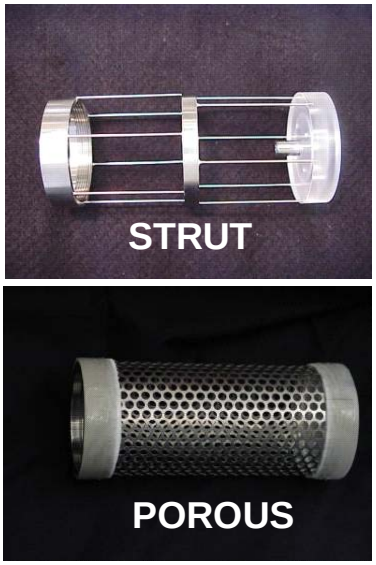

Figure 2.11: Fiber bundle cage designs for Generation III PRAL.

Three stationary center diffusers were made from acrylic for the Generation III prototype and are shown in Figure 2.12. The length of each diffuser was 12 cm. Flow entered the hole in the center of the diffuser and was channeled across the fibers depending on the hole pattern of the diffuser. The Four-hole diffuser is shown in the far left hand side of Figure 2.12. The flow entered at the proximal end of the fiber bundle through a ¼" diameter hole and exited out of four radial 10 mm diameter holes.

Figure 2.12: Stationary center diffusers. Left: Four-hole Diffuser. Middle: Even Diffuser. Right: Axial Diffuser

The Even diffuser is shown in the middle of Figure 2.12. This diffuser had a center bore diameter of 1 inch and had four rows of five radial holes that decrease in size along the length of the device from 6, 5, 4, 3.5, and 3.5 mm in diameter. The Axial diffuser is shown in the far right hand side of Figure 2.12. This diffuser had an inlet hole with a diameter of ½ inch and consisted of one row of five 7.5 mm diameter holes. Chapter 4 discusses the effect of the diffuser design on gas exchange. The following chapter describes the gas exchange and pumping tests that were performed to characterize the PRAL prototypes.

3.0 GAS EXCHANGE AND PUMPING

3.1 INTRODUCTION

The PRAL utilizes a rotating fiber bundle to increase gas exchange efficiency and pump blood. Higher gas exchange efficiency allows less fiber surface area and lower blood flowrates than in passive oxygenators. Three PRAL prototypes were manufactured (described in Chapter 2). Generation I incorporated a rotating fiber bundle that was potted directly to the center diffuser. Generation II incorporated a rotating core with a stationary fiber bundle. Generation III incorporated a rotating fiber bundle with a stationary diffuser. This chapter describes the gas exchange and pumping characterizations of each generation in water, and Generation III in bovine blood.

3.2 METHODS

3.2.1 In vitro gas exchange

The gas exchange of the PRAL prototypes was characterized in water and bovine blood from a local slaughterhouse. A flow loop was constructed for both water and blood testing that consisted of a reservoir, a centrifugal pump (for Water - March Manufacturing, LC-2CP-MD, Glenview IL; for Blood – Medtronic, Biomedicus BP-80X,

Minneapolis, MN), a commercial oxygenator (Affinity^{TM}, Medtronic, Minneapolis MN) used as a deoxygenator, and the PRAL prototype (Figure 3.1). Tygon tubing (P/N R-3603, Cole Parmer, Vernon Hills, IL) connected the outflow port of the reservoir to the inlet of the centrifugal pump. The pump was used in conjunction with a Hoffman clamp (Cole Parmer, Vernon Hills, IL) to set the flowrate. Sweep gas through the commercial oxygenator was a N_2/CO_2 mix adjusted with a gas blender (Cole Parmer, PMM2-010032, Vernon Hills, IL) to set the inlet conditions in accordance with the Association for the Advancement of Medical Devices (AAMI) standards [75]: O_2 inlet saturation 65 +/- 5% and inlet pCO_2 of 45 +/- 5 mmHg. The test fluid flowed from the commercial oxygenator into the PRAL and then back to the reservoir. The flowrate was measured using a flow probe (Transonic Systems, Inc, T110, Ithaca, NY). O_2 partial pressures at the inlet and outlet of the device were measured using a blood-gas analyzer (ABL-505 Radiometer, Copenhagen, Denmark). The concentration and saturation of hemoglobin was measured with an OSM3 Hemoximeter (Radiometer, Copenhagen, Denmark). Pure oxygen sweep gas flowed under vacuum through the PRAL fiber lumens at 6.5 L/min. The gas then flowed through a moisture trap and through a Top Trak flow meter, which displays the mass flowrate in units of L/min at a reference temperature and pressure (Sierra Instruments, 822-13-OV1 PV1-V1, Monterey CA). A vacuum pump (Barnant, 400-3910, Barrington, IL) and needle valve were used to maintain constant sweep gas flow through the device. A CO_2 analyzer (Physiodyne, CO2-44B, Quogue, NY) was used to measure the concentration of CO_2 exiting the gas stream of the PRAL. The blood was filtered with 40 μm pore size filters (P/N SQ40S, Pall Biomedical, Fajardo, PR) on the day of collection to remove any hair or extraneous particles due to the

collection process, and Gentamycin (0.1 g/mL blood) was added to prevent infection. The gas exchange for Generation I was evaluated in water at 1.5 and 3.0 L/min. The gas exchange for Generation II was evaluated in water at 1.5 L/min. The gas exchange for Generation III was evaluated in water at 3.0 L/min and in blood at 0.75 L/min.

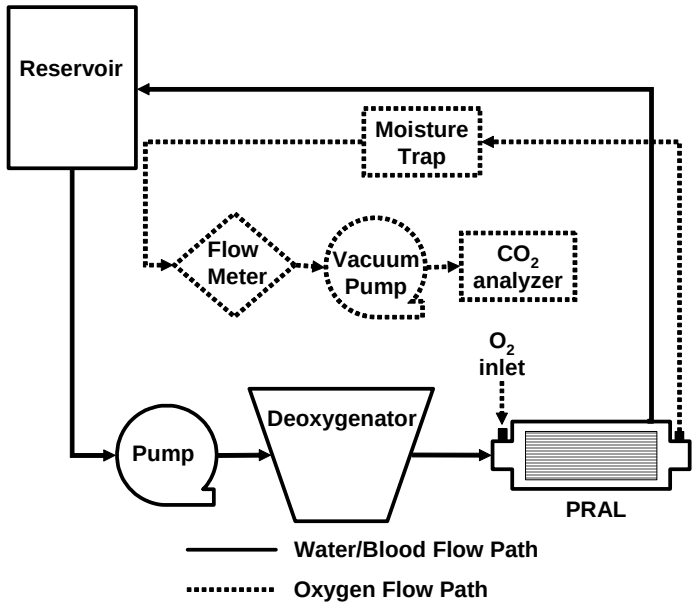

Figure 3.1: Gas exchange setup.

Oxygen transfer rates in blood (VO_2) were calculated using the following relationship [76]:

$$V_{O2} = Q\left[\alpha_{O2}(P_{O2}^{out} - P_{O2}^{in}) + C_T(S^{out} - S^{in})\right] \quad \textbf{(3.1)}$$

where Q is the blood flow rate, α_{O2} is the solubility of O_2 (3.16E-4 ml O_2/ml blood/cmHg), and $(P_{O2}^{out} - P_{O2}^{in})$ is the difference in partial pressure between the inlet and outlet of the device. C_T is the hemoglobin binding capacity of blood (0.167 ml O_2/ml blood), and $(S^{out} - S^{in})$ is the change in saturation of the hemoglobin from the inlet to the outlet. O_2 transfer in water was calculated by setting ΔS equal to zero in Equation 3.1

and using a solubility of 3.0E-4 ml O_2/ml H_2O/cmHg [77]. Carbon dioxide removal rate (V_{CO2}) was calculated from the sweep gas flowrate in units of L/min at standard temperature and pressure (Q_{OUT}^{STP}) and CO_2 fraction (F_{CO2}) exiting the PRAL:

$$V_{CO2} = Q_{OUT}^{STP} F_{CO2} \qquad \textbf{(3.2)}$$

Variations in the inlet pCO_2 can affect the overall gas exchange of the device. For example, an inlet pCO_2 of 45 mmHg will have a lower CO_2 removal rate than an inlet pCO_2 of 50 mmHg because this 5 mmHg difference in inlet conditions corresponds to a 10% difference in concentration gradient across the fiber membranes as the blood first contacts the fibers. Therefore, the CO_2 exchange was normalized (V_{CO2}^{*}) to an inlet pCO_2 of 50 mmHg to reduce the variability associated with fluctuating inlet conditions [20]:

$$V_{CO2}^{*} = V_{CO2} \frac{50}{pCO_2^{INLET}} \qquad \textbf{(3.3)}$$

In this equation, V_{CO2} is in units of ml/min and pCO_2 is in units of mmHg.

3.2.2 Pumping

The pumping ability of the PRAL was quantified in a recirculating flow loop with a reservoir, the PRAL, and tygon laboratory tubing (Figure 3.2). The reservoir was a 5 gallon plastic bucket with an inlet and outlet hole drilled ½ inch from the bottom of the bucket. Fittings with ½" bulkhead barb fittings (Cole Parmer, Vernon Hills, IL) were placed into the holes and sealed with rubber gaskets to prevent leaks. The flowrate of the fluid was measured with the Transonic flow probe that attached directly to the

tubing, and the pressure difference across the device was measured using a differential pressure transducer (Validyne Engineering Corporation, CD379, Northridge, CA). The transducer was placed into the circuit using 3/8”-3/8” luer connectors. The low side of the pressure transducer was placed less than 2 inches from the inlet of the PRAL, and the high side of the pressure transducer was placed less than 2 inches from the outlet port of the PRAL. The low and high sides were maintained at the same elevation. Pumping at rotation rates of 500, 1000, and 1500 RPM was evaluated in water. At constant RPM, the flowrate was throttled down incrementally to zero flow (shut off head) using a Hoffman clamp (Cole Parmer, Vernon Hills, IL) placed downstream of the high side of the pressure transducer. At each flowrate, the pressure increase across the device was measured.

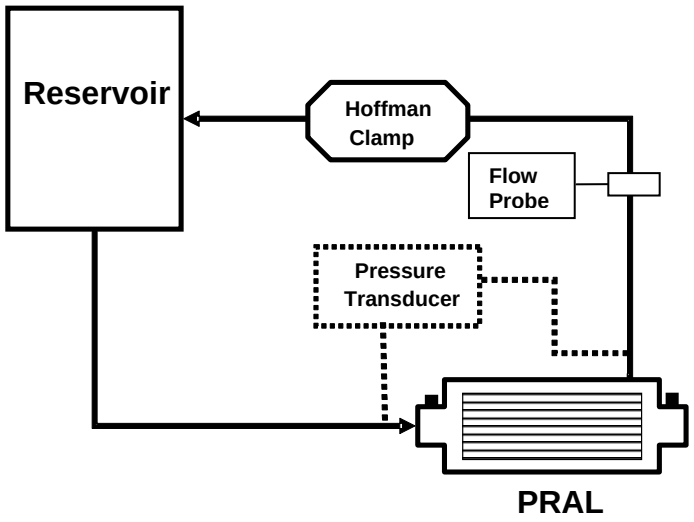

Figure 3.2: Schematic of Pumping test loop.

3.3 RESULTS AND DISCUSSION

3.3.1 Generation I – Gas exchange in water

The gas exchange rates in water flowing at 1.5 L/min for Generation I with the Even diffuser (Figure 2.5 – bottom) are shown in Figure 3.3. At zero RPM, the CO_2 removal per area was 89 ml/min/m^2 and the O_2 supplied per area was 72 ml/min/m^2. Rotation of the fiber bundle had no effect on gas exchange. At 1500 RPM, the CO_2 removal per area was 88 ml/min/m^2 and the O_2 supplied per area was 69 ml/min/m^2. The gas exchange rates in water flowing at 3 L/min are also shown in Figure 3.3. At zero RPM, the CO_2 removal per area was 136 +/- 18 ml/min/m^2 and the O_2 supplied per area was 96 +/- 7 ml/min/m^2. At 1000 RPM, the CO_2 removal per area was 130 +/- 6 ml/min/m^2 and the O_2 supplied was 93 +/- 4 ml/min/m^2.

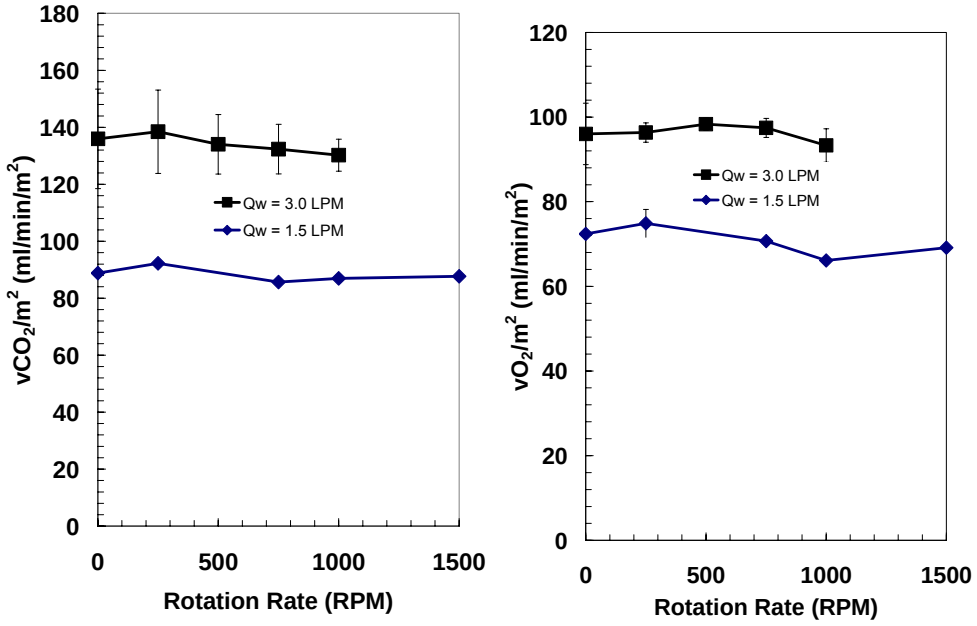

Figure 3.3: Gas exchange per area for Generation I: CO_2 (left) O_2 (right).

Gas exchange efficiency of hollow fiber membrane devices like the PRAL is dependent on the relative velocity between the fluid and the fibers. We hypothesized that relative velocity was low between the fibers and the fluid in the Generation I prototype because the fibers were potted directly to the rotating diffuser. Fluid enters the center of the diffuser with zero angular velocity and is accelerated to the same angular velocity as the fibers through the rotation of the diffuser. Therefore, the relative angular velocity between the fluid and the fibers is zero as the fluid enters the fiber bundle. The drag force of the fibers acts on the fluid elements entraining the fluid within the rotating bundle and maintaining zero relative velocity as the fluid moves radially through the bundle toward the outer fiber layers. We hypothesized that relative velocity existed in the outer fiber layers of the Generation I prototype due to the shear force imposed by the stationary housing surrounding the fiber bundle. The shear force at the housing wall opposes the drag force of the fiber bundle to generate relative velocity in the outer layers depending on the relative magnitudes of the shear and drag forces. We believed that the relative velocity in the outer layers had no effect on gas exchange with rotation because the gradient for gas transfer was reduced by the inner fiber layers before the fluid had reached the outer layers.

We tested the hypothesis that the rotating diffuser in Generation I generated no relative velocity by fabricating the Generation II prototype, which had a stationary fiber bundle and a rotating diffuser in the center of the bundle. In this prototype, the fluid entered the diffuser with zero angular velocity and was accelerated by the rotation of the diffuser before entering the stationary fiber bundle. In this design, we hypothesized that

the fluid would enter the bundle with high relative velocity and therefore exhibit an increase in gas exchange with rotation rate.

3.3.2 Generation II – Gas Exchange in Water

Rotation of the center core with a stationary fiber bundle had no effect on gas exchange in water at 1.5 L/min (Figure 3.4). At zero rotation CO_2 removal per area was 100 +/- 0 ml/min/m^2, and at 1500 RPM, CO_2 removal was 93 +/- 1 ml/min/m^2. No effect of rotation was observed on O_2 transfer. At zero rotation O_2 supplied per area was 67 +/- 1 ml/min/m^2, and at 1500 RPM, O_2 supplied was 61 +/- 1 ml/min/m^2.

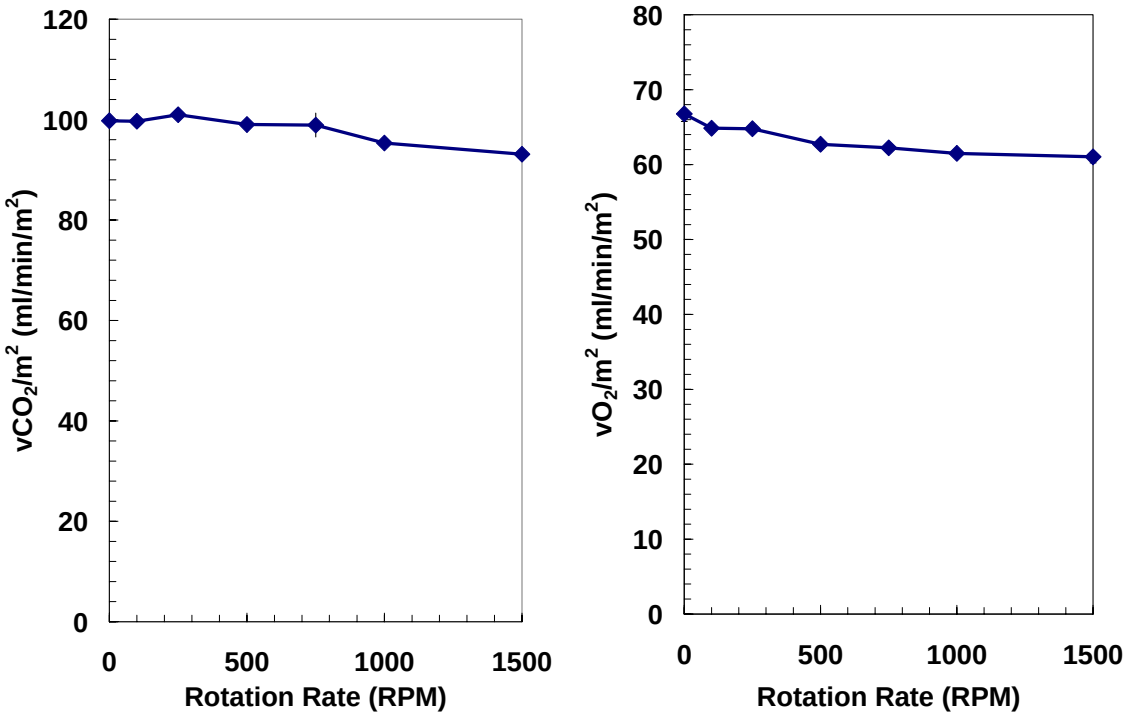

Figure 3.4: Gas exchange per area for Generation II: CO_2 (left) O_2 (right).

The Generation II prototype flow path was designed with a rotating diffuser and stationary fiber bundle so that fluid would be introduced into the bundle with high

relative angular velocity. Through experiments in water, we showed that gas exchange was not increased by rotation of the diffuser. We hypothesized that the drag force caused by the fibers in both the Generation I and II prototypes was entraining the fluid within the fiber bundle generating zero relative velocity and hence no increase in gas exchange with rotation. We formulated a mathematical model to investigate the role of the drag and shear forces acting on the fluid elements within the fiber bundle. The model predicted that the drag force due to the rotating fibers was significantly higher than the shear force resulting in zero relative angular velocity within the first outer layer of fibers. The model also predicted that the drag force increased with the thickness of the fiber bundle. The model is described in Chapter 4, and experimental measurements of gas exchange in the outer layers of fibers (experiments known as selective perfusion) are also presented in Chapter 5 to investigate the penetration of relative velocity into the fiber bundle.

We fabricated the Generation III prototype to include stationary walls on the inner and outer layers of the fiber bundle. We also decreased the thickness of the fiber bundle from 25 layers to 7 layers maintaining the same surface area as the earlier prototypes by increasing the length of the bundle from 4 cm to 13 cm. We hypothesized that stationary walls on the inside and outside of the rotating fiber bundle would create shear stress to oppose the drag force of the rotating fiber bundle. We decreased the number of layers to reduce the drag force and enable relative velocity to penetrate further into the fiber bundle than in the previous PRAL prototypes.

3.3.3 Generation III – Gas exchange in water and blood

Gas exchange increased with rotation in water for the PRAL Generation III (Figure 3.5). The CO_2 exchange per area increased from 78 +/- 4 ml/min/m^2 at zero rotation to 189 +/- 2 ml/min/m^2 at 1500 RPM. The O_2 exchange per area increased from 42 +/- 2 ml/min/m^2 at zero rotation to 104 +/- 5 ml/min/m^2 at 1500 RPM.

The gas exchange of the PRAL in blood at 0.75 L/min is shown in Figure 3.6 and Figure 3.7 as a function of rotation rate. The CO_2 removal per fiber bundle surface area was 125 +/- 4 ml/min/m^2 at 0 RPM and increased to 240 +/- 9 ml/min/m^2 at 1500 RPM. The O_2 supplied per fiber bundle surface area increased from 66 +/- 0 ml/min/m^2 to 124 +/- 6 ml/min/m^2. Maximum overall gas exchange occurred at 1500 RPM with 101 ml/min of CO_2 removed and 62 ml/min of O_2 supplied.

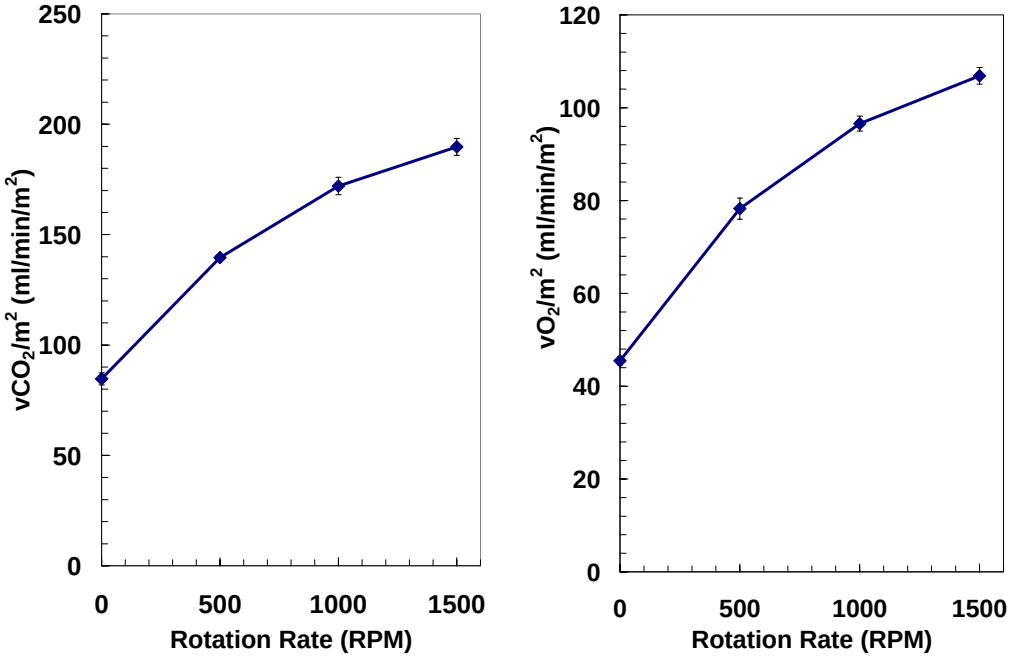

Figure 3.5: CO_2 exchange per area (left) and O_2 exchange per area (right) for Generation III.

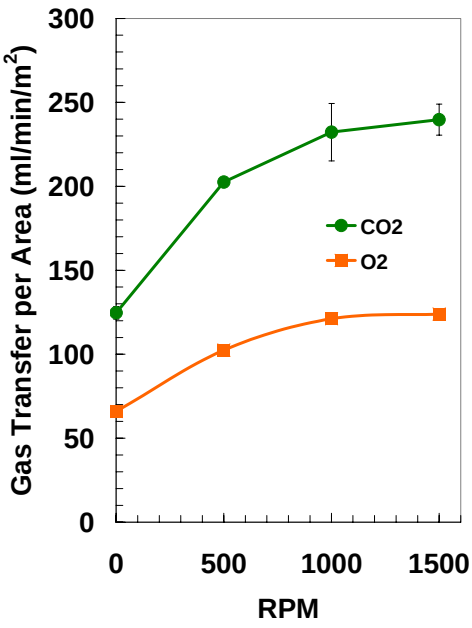

Figure 3.6: Gas transfer per area in blood at 0.75 L/min.

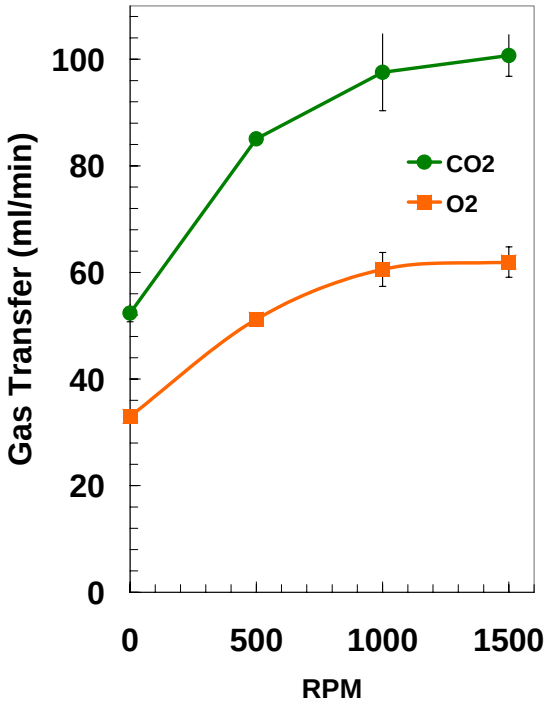

Figure 3.7: Gas transfer in blood at 0.75 L/min.

We believe that gas exchange increased with rotation in the Generation III prototype because of the shear stress generated by the stationary walls on either side of the rotating fiber bundle. In both the Generation I and II prototypes, shear was only present on one side of the fiber bundle, the outer fiber bundle surface for Generation I and the inner fiber bundle surface for Generation II. Additionally, the fiber bundle was much thinner in the Generation III prototype allowing relative velocity to penetrate deeper into the fiber layers. We investigated the penetration of relative velocity into the fiber bundle through selective perfusion experiments described in Chapter 5. We found that relative velocity penetrated all layers of the fiber bundle in the Generation III device, and only penetrated the first few layers in the Generation I and II devices. We investigated the flow in the outer gap between the rotating fiber bundle and outer housing using particle image Velocimetry (Chapter 5). We found that the rotation of the fiber bundle gives rise to Taylor vortices which penetrate through the fiber bundle providing relative velocity on the order of the radial velocity causing gas exchange enhancement with rotation. We hypothesize that these vortices are present in the Generation I and II prototypes, but the thickness of the fiber bundle reduces the number of layers exposed to the vortices. The gas exchange results indicated that rotating the fiber bundle increased the efficiency of gas transfer. At a blood flowrate of 0.75 L/min, the PRAL removed 101 ml/min CO_2 with an efficiency of 250 ml/min/m^2 thus meeting the gas exchange target. To put this in perspective, the Affinity oxygenator (Medtronic, Minneapolis MN) achieves approximately 100 ml/min/m^2 at the same flowrate. The rotating fiber bundle enables the PRAL surface area to be only 0.42 m^2 compared to 2.5 m^2 in the Affinity.

3.3.4 Generation I – Pumping in water

The pumping ability of the Generation I prototype in water at rotation rates of 1000, 500, and 250 RPM is shown in Figure 3.8. At 1000 RPM, the PRAL generated a pressure of 32 mmHg at 0.75 L/min. At 500 RPM, the PRAL generated a pressure of 7 mmHg at 0.75 L/min.

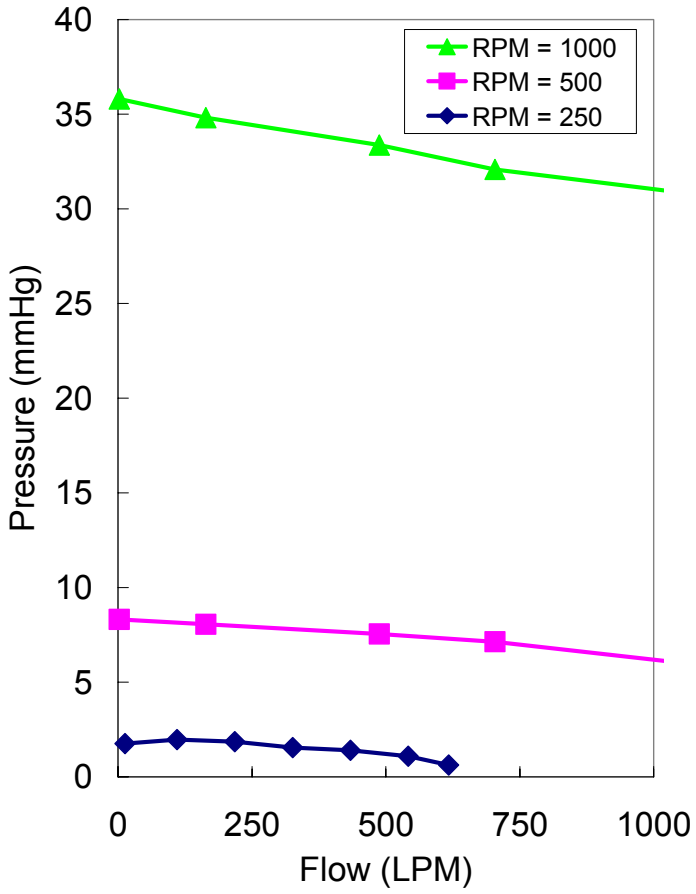

Figure 3.8: Pump curves for Generation I.

3.3.5 Generation II – Pumping in water

The pumping ability of the Generation II prototype in water at 1500 RPM is shown in Figure 3.9. The PRAL generated a pressure of 30 mmHg at 0.62 L/min. The stationary fiber bundle affected the pumping ability of the PRAL by less than 10%. With the fibers removed, the PRAL generated a pressure of 32 mmHg at 0.64 L/min.

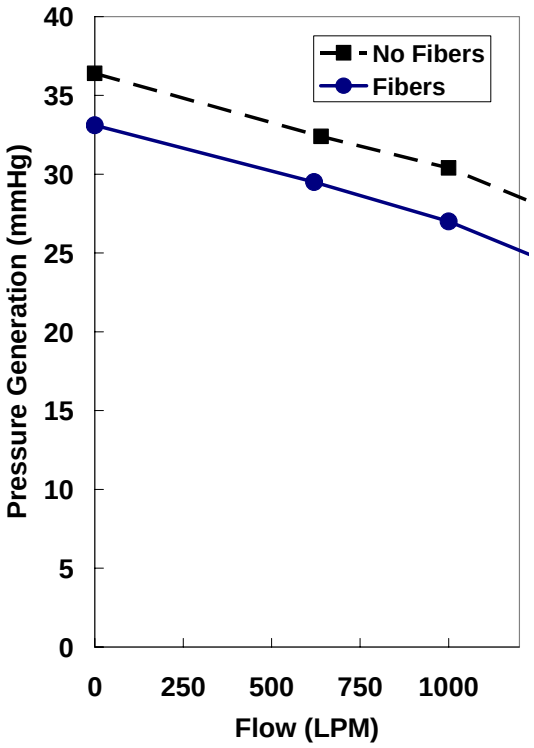

Figure 3.9: Pump curves for Generation II at 1500 RPM.

3.3.6 Generation III – Pumping

The rotating fiber bundle generated pressure that enabled the PRAL to pump. We tested the pumping ability in a glycerol/water solution with a viscosity similar to that of whole blood (μ = 3.4 cP). The comparison between water and the blood analogue are

shown in Figure 3.10. Below 1 L/min, the pump curves differ by less than 10% at each rotation rate.

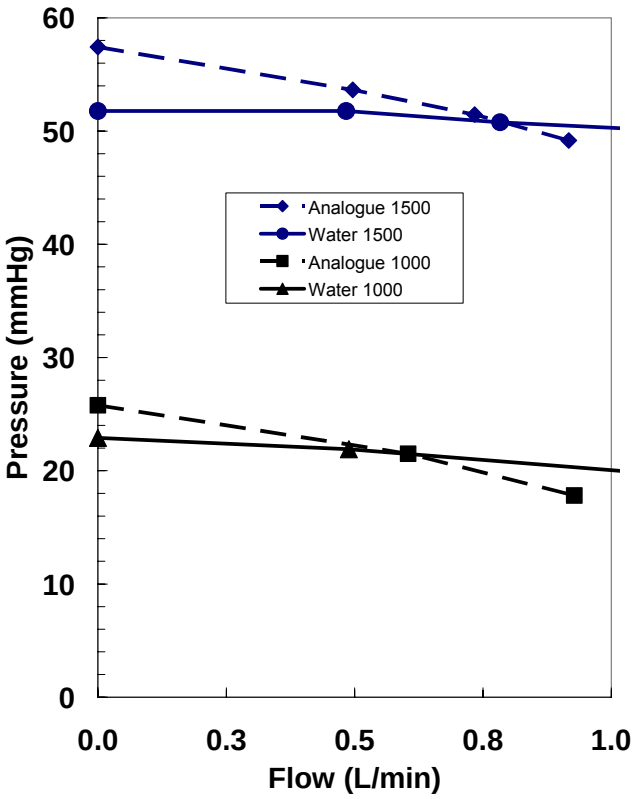

Figure 3.10: Pump curves for the Original PRAL fiber bundle in water and blood analogue solution.

During fiber bundle rotation, the fluid gains angular velocity which is converted to pressure at the outlet of the device enabling the PRAL to pump. The kinetic energy per volume (KE) can be approximated as KE~ρv^2 where ρ is the density of the fluid and v is the absolute velocity of the fluid. Therefore, the pumping pressure can be approximated as P~ρv^2. A trade-off exists between the pumping ability of the fiber bundle and the gas exchange ability. As relative velocity between the fibers and the fluid increases, the absolute velocity of the fluid decreases. If the relative velocity is zero, then the pumping

pressure generated by the rotating fiber bundle is maximal, but the gas exchange will not be affected by rotation. As the relative velocity increases, the gas exchange increases due to rotation, but the pumping ability of the device decreases. In Generation I, the relative velocity between the fibers and the fluid was zero as shown by the lack of increase in gas exchange with rotation. In Generation III, the relative velocity was increased with rotation since the gas exchange was increased. Our PIV studies indicated that the relative velocity was on the order of the radial velocity. If we subtract out the radial velocity from the angular velocity, we can estimate the absolute velocity of the fluid exiting the fiber bundle. Although relative velocity exists within the PRAL fiber bundle and increases gas exchange, the absolute velocity is still within 90% of the angular velocity of the fiber bundle enabling the Generation III fiber bundle to generate nearly the same pressure as the Generation I prototype.

We estimated the pressure that the PRAL needed to generate from the pressure-flow relationship of a dual lumen cannula commonly used in pediatric ECMO (Origen Biomedical, [78]). The cannula is 18 Fr and in the flow range of 0.5-0.75 L/min the pressure drop ranges from 80-100 mmHg. Figure 3.11 is the Generation III pumping ability with the estimated pressure drop of the proposed cannula (hatched region). The PRAL prototype generated 52 mmHg at 750 ml/min at 1500 RPM, approximately half of the required pumping ability.

Dimensional analysis is one approach for estimating the effect of geometric variables on the pump performance curves [79]. The dependent variables are the head generated by the pump, *h*, the angular frequency of the fiber bundle, ω, the outer diameter of the fiber bundle *d,* and the flowrate*, Q*. The rotation rate that will generate 80-100 mmHg

pressure can be calculated by transforming the dependent variables into two dimensionless groups, the head coefficient defined as $C_H = \frac{gh}{\varpi^2 d^2}$ and the flow coefficient defined as $C_Q = \frac{Q}{\varpi d^3}$ where *g* is the gravitational constant. Transforming the data in this way collapses the pump curves into one universal curve (Figure 3.12) that can be used to estimate the PRAL pumping ability at any angular frequency. The theoretical pumping ability at 2000 RPM is shown in Figure 3.11 as a solid line. At this angular frequency, the PRAL pump curve is within the pressure-flow characteristics of the cannula, indicating that this cannula can be used for our application.

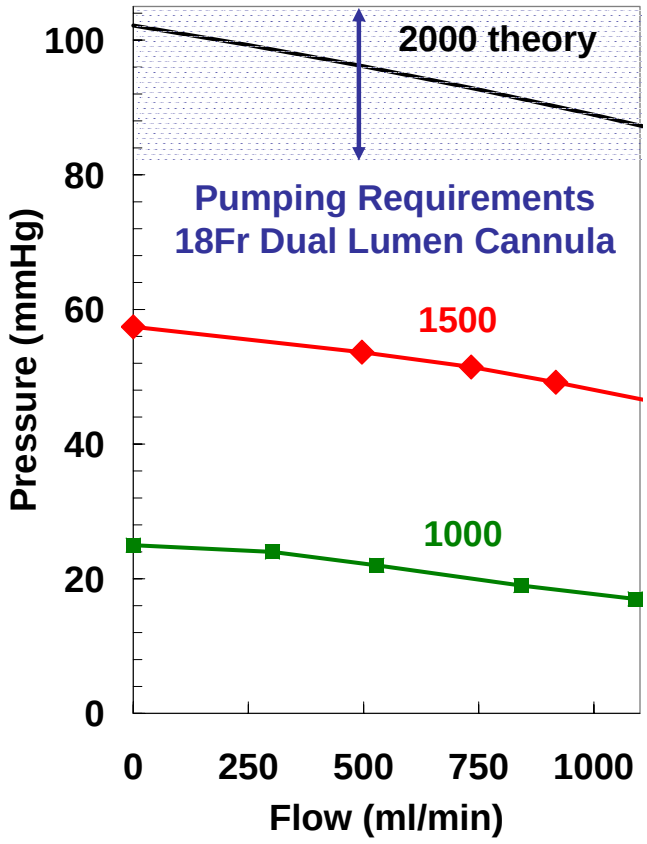

Figure 3.11: Theoretical pump curve meets pumping requirements.

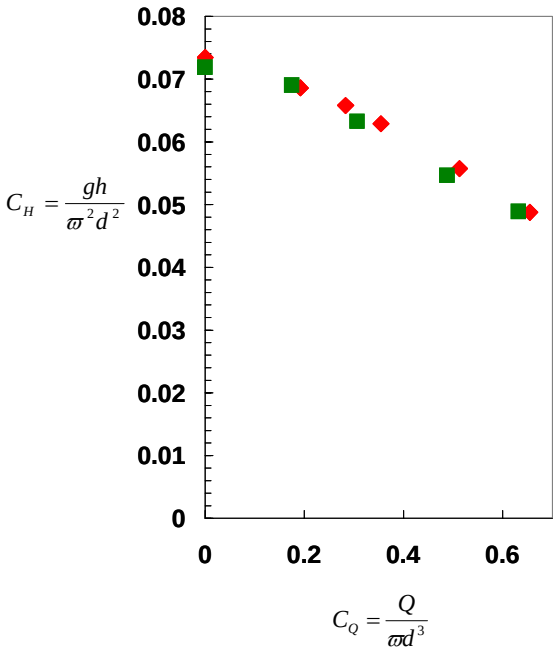

Figure 3.12: Nondimensionalized pump curves.

3.4 SUMMARY

The goal of the PRAL was to provide CO_2 removal at a blood flowrate less than 0.75 L/min to allow the native lungs time to heal. The fiber bundle was rotated to increase gas exchange and enable the PRAL to pump. Generation I and II prototypes did not exhibit an increase in gas exchange with rotation. The Generation III PRAL exhibited an increase in gas exchange with rotation of the fiber bundle. The main differences between Generations I and II and Generation III was that Generation III was manufactured with 7 layers instead of 25 and rotated between two stationary walls. We have shown that the pumping in the Generation III design is adequate to provide flow through an 18 Fr commercially available cannula.

The remaining chapters in this thesis describe the experimental and computational methods and results that were used to gain an understanding of the mechanism for gas exchange enhancement that was present in Generation III, but not in Generations I and II.

4.0 EVALUATION OF UNIFORM FLOW IN THE PRAL

4.1 INTRODUCTION

The Generation III PRAL exhibited increased gas exchange with rotation whereas the Generation I and II PRAL did not. The fiber bundle thickness of the Generation III prototype was only 7 layers compared to 25 layers in the previous designs. The decreased thickness of the Generation III fiber bundle led to an increased penetration of relative angular velocity into the fiber bundle during rotation and therefore increased gas exchange. Decreasing the thickness of the fiber bundle also decreased the resistance to flow in the radial direction of the bundle. If the resistance is too low, the radial flow entering the bundle will jet along the path of least resistance becoming nonuniform through the fiber bundle and leading to lower overall gas exchange. We evaluated 3 diffuser designs for their effect on flow distribution by measuring gas exchange for each design. We injected light sensitive dye into the flow to observe the uniformity of flow as it exited the fiber bundle. We also measured the local concentration of O_2 and CO_2 in the outer gap surrounding the fiber bundle to test for uniformity. We determined that the resistance in the Generation III fiber bundle is high enough to create uniform radial flow independent of the diffuser design.

4.2 GAS EXCHANGE IN WATER FOR EACH DIFFUSER

Gas exchange was tested in the mock loop described in Chapter 3 for each diffuser. The diffusers are shown in Figure 4.1. Gas exchange was evaluated for rotation rates from 0 to 1500 RPM. The water flowrate was 3.0 L/min and the sweep gas flowrate was 3.0 L/min.

Figure 4.1: Diffusers tested for uniform flow. Left: Four Hole Diffuser. Middle: Even Diffuser. Right: Axial Diffuser.

The design of the center diffuser design had no effect on gas exchange (Figure 4.2). At zero rotation, the CO_2 removal was 51 +/- 2 ml/min/m^2, 52 +/- 2 ml/min/m^2, and 50 +/- 1 ml/min/m^2 for the Even Diffuser, Axial Diffuser, and Four Hole Diffuser, respectively. At 1500 RPM, the CO_2 removal was 97 +/- 3 ml/min/m^2, 106 +/- 1 ml/min/m^2, and 109 +/- 3ml/min/m^2 for the Even Diffuser, Axial Diffuser, and Four Hole Diffuser, respectively (Figure 4.2). At 1500 RPM, The CO_2 removal was slightly higher for the Four Hole Diffuser, but not substantially different from the other diffuser designs.

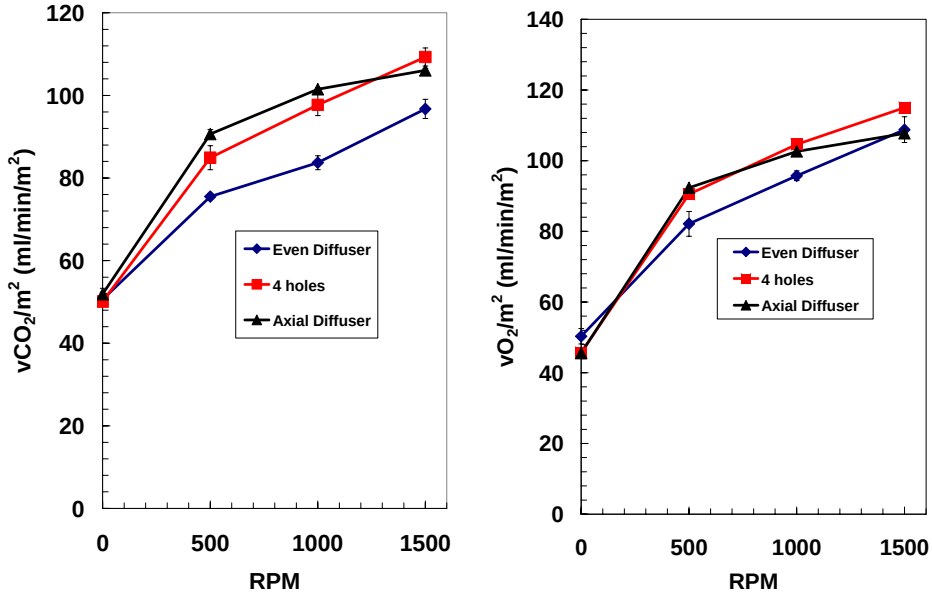

Figure 4.2: Gas transfer per area for different diffuser designs.

4.3 QUALITATIVE FLOW VISUALIZATION

The setup for flow visualization is shown in Figure 4.3. Water was pumped in a single pass loop from a reservoir through the PRAL at no rotation and into a sink drain. Light sensitive dye (Food Coloring, Giant Eagle, Pittsburgh, PA) was injected as a 10 cc bolus upstream of the centrifugal pump. The dye became well-mixed into the bulk flow within the centrifugal pump, then flowed into the PRAL. The dye entered the PRAL inlet at 3 L/min and images of the PRAL were recorded with a digital camcorder. The images were broken into individual frames and viewed using IrfanView 3.0 software.

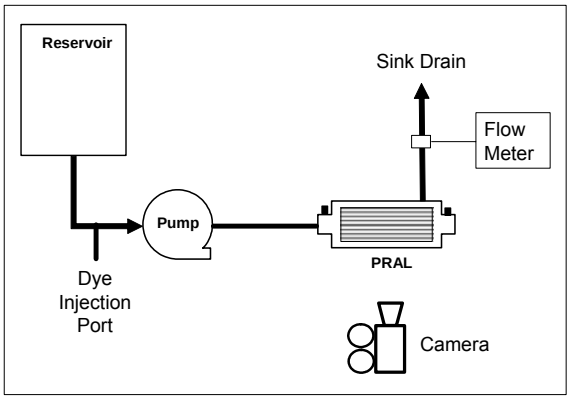

Figure 4.3: Schematic of Flow Visualization Setup.

All three stationary diffusers were tested, and the strut cage was used in all designs. Figure 4.4(a) and Figure 4.4(b) show snapshots of flow through the fiber bundle with the Even Diffuser as the dye initially enters the fiber bundle and several seconds later. Initially, the flow appears to be entering the fiber bundle very nonuniformly at the downstream end of the device, but over time the fluid became more uniformly distributed throughout the bundle. This process was repeated for each diffuser three times. In all cases, the flow became uniform within several seconds after the first appearance of dye indicating that regardless of the diffuser design the resistance of the fiber bundle caused flow to become uniform.

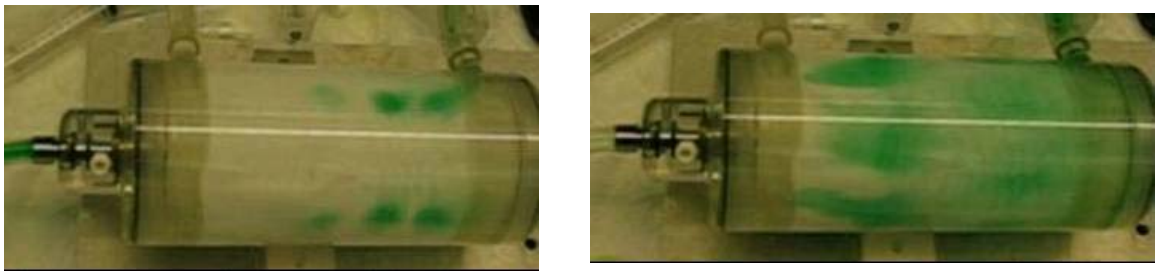

Figure 4.4: Flow visualization (a) as dye first enters the fiber bundle; (b) several seconds after dye has entered the fiber bundle.

The flow visualization studies confirmed that flow through the fiber bundle was uniform. Although the flow appeared to be nonuniform at first, the flow became uniform within several seconds. The reason for this was that the transit time for the flow to reach the upstream half of the bundle was longer than the transit time for fluid penetrating the bundle at the downstream half. Therefore, the dye appeared at the downstream end of the bundle first, and then appeared everywhere as the dye reached all areas of the bundle. The uniform flow visualized in these studies validated the experimental result that gas exchange was independent of the diffuser design.

4.4 OUTER GAP AXIAL CONCENTRATION

We measured concentrations of O_2 and CO_2 in the outer gap between the rotating fiber bundle and stationary housing at 0 and 1500 RPM for the Four Hole diffuser. The concentrations of O_2 and CO_2 were measured at three axial positions along the length of the fiber bundle. Three 1 mm holes were drilled and tapped at a distance from each other of 5.5 mm so that luer connections could be used to draw samples (Figure 4.5). Samples were drawn at each axial location simultaneously into a syringe. The samples were drawn slowly to prevent disrupting the flow in the gap.

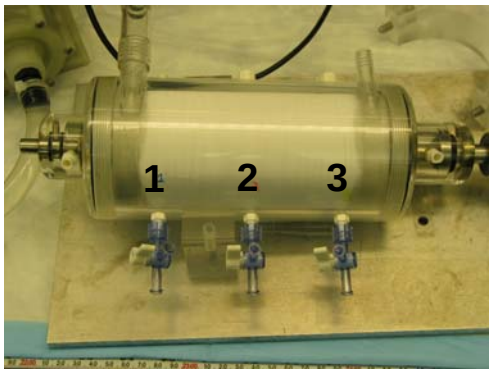

Figure 4.5: Ports along axial length of bundle.

The pO_2 and pCO_2 concentrations for each axial port are plotted in Figure 4.5 for zero rotation and a bundle rotation rate of 1500 RPM. At zero rotation, the pCO_2 values were the same for all three axial ports. During rotation at 1500 RPM, the pCO_2 values decreased from 32 +/- 3 mmHg at Port 1 to 19 +/- 0 mmHg at Port 3 (p=0.0004). The results trended the same way for O_2. The stationary bundle pO_2 values were the same for all three axial ports. During rotation at 1500 RPM, the pO_2 values increased from 302 +/- 3 mmHg at Port 1 to 504 +/- 0 at Port 3 (p=0.00009).

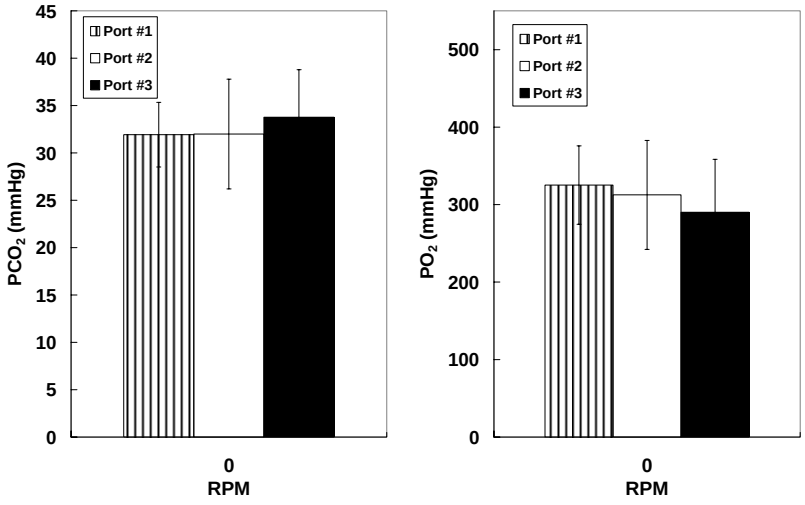

Figure 4.6: Axial partial pressure along the length of the bundle at no rotation. Left: PCO_2; Right: PO_2.

The axial concentration measurements at zero rotation confirmed that flow through the bundle was uniform because the concentration was the same at all axial points. If flow through the bundle was nonuniform, we expect that the concentration would have varied along the length of the bundle. At regions of lower flow, the pCO_2 would have dropped to lower levels than at regions of higher flow.

Uniform flow in the PRAL fiber bundle depends on the resistance of the fiber bundle compared to the magnitude of the kinetic pressure exiting the holes in the diffuser. The kinetic pressure at one of the holes in the Four Hole diffuser was calculated as $P_{kin} \approx \frac{1}{2}\rho V^2$ where ρ is the density of the fluid, and V is the velocity of the fluid exiting the hole calculated as the flowrate divided by the cross-sectional area of the hole. If the pressure drop across the bundle is greater than the kinetic pressure of the flow exiting the diffuser hole, then the flow will be uniform. We placed pressure taps immediately upstream and downstream of the PRAL and measured pressure drop across the device as a function of flowrate at zero RPM. We also measured the pressure drop across the device without the fiber bundle in the device to determine the pressure drop across the inlet and outlet ports. The pressure drop across the inlet and outlet ports was subtracted from the pressure drop across the complete device to determine the pressure drop across the fiber bundle. Figure 4.7 is a plot of the pressure drop across the bundle as a function of flowrate and the kinetic pressure at one of the holes in the diffuser. The pressure drop across the bundle is at least 10 times the kinetic pressure of the fluid exiting one of the holes in the diffuser at all flowrates. Therefore, the resistance of the fiber bundle creates uniform flow within the PRAL.

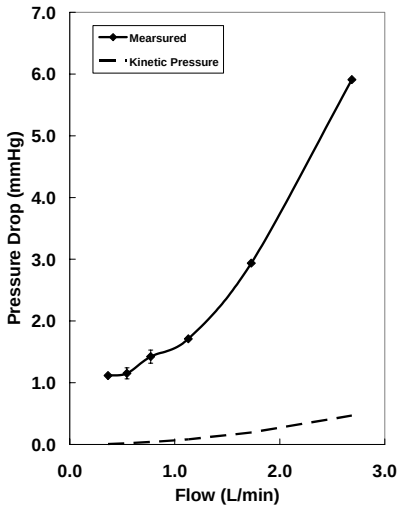

Figure 4.7: Pressure drop across PRAL device (solid line) and kinetic pressure of jet in Four Hole diffuser (dashed).

4.5 SUMMARY

In the PRAL, nonuniform flow would lead to lower overall gas exchange. The current design of the PRAL contains seven layers of fibers which creates enough resistance to prevent nonuniformities in the flow as shown by the experiments in this Chapter. At zero rotation and 1500 RPM the difference in CO_2 and O_2 exchange per area was less than 12% among the diffuser designs (Figure 4.2). The flow visualization experiments provided a qualitative understanding of how fluid exits the bundle uniformly. The axial concentration measurements and pressure drop measurements validated that the resistance of the fiber bundle creates uniform flow in the PRAL.

5.0 MECHANISMS FOR GAS EXCHANGE ENHANCEMENT DUE TO ROTATION IN THE PRAL

5.1 INTRODUCTION

Gas exchange rates in hollow fiber membrane oxygenators are dependent on the velocity difference (relative velocity) between the blood and the fibers. One of the goals in rotating the fiber bundle (or diffuser) in the PRAL is to increase relative velocity to augment gas exchange without increasing the flowrate of blood through the device. The magnitude of the relative velocity in the fiber bundle depends on the balance of shear and drag forces acting on the fluid within the fiber bundle. The drag force is due to the tightly packed fibers that tend to entrain the fluid during rotation. The shear force results from the stationary walls surrounding the bundle that acts in the direction opposite of fiber bundle rotation. If the drag force is much greater than the shear force the fluid elements become entrained in the rotating fiber bundle and gas exchange is not a function of rotation rate. In the gas exchange tests discussed in Chapter 3, rotation had no effect on gas exchange in the Generation I and II PRAL prototypes, whereas in the Generation III prototype a rotation rate of 1500 RPM produced a 93% increase in gas exchange. We developed a mathematical model of the drag and shear forces within the fiber bundle to determine the relative velocity profile within the fiber bundle for each PRAL prototype. The relative velocity was then input into a mass transfer correlation to predict the gas exchange rates as a function of rotation rate. The model predicted that the drag force was high enough to reduce the relative angular velocity to zero within the first few layers of fibers. The penetration of relative velocity into the bundle was tested

experimentally by performing selective perfusion experiments. In these experiments, different layers of the fiber bundle sweep gas pathway were occluded so that gas exchange would only occur in targeted layers of the bundle.

5.2 ANALYTICAL MODEL OF RELATIVE VELOCITY IN THE FIBER BUNDLE

We developed a mathematical model to calculate the relative velocity within the rotating fiber bundle and predict CO_2 removal in water. The velocity within the fiber bundle was calculated by performing a differential momentum balance on the fiber bundle:

$$\rho\left[V_r \frac{\partial V_\theta}{\partial r} + \frac{V_r V_\theta}{r}\right] = \mu_e \frac{\partial^2 V_\theta}{\partial r^2} + \frac{\mu}{k}\left(U - V_\theta\right) \qquad \textbf{(5.1)}$$

The left hand side represents the mass per total volume (fluid and fibers) times the acceleration of fluid within the fiber bundle. The first term on the right hand side represents the shear force per volume, and the second term is the drag force per volume due to the rotating fibers. Since the bundle thickness (t_b) is much smaller than the mean radius of the bundle (R_m) (t_b/R_m~0.06), $\frac{1}{r}\frac{\partial}{\partial r}\left(r\frac{\partial^2 V_\theta}{\partial r}\right) \cong \frac{\partial^2 V_\theta}{\partial r^2}$ where V_r is the radial velocity, ρ is the density of water, V_θ is the absolute angular velocity in the bundle, and U is the fiber bundle rotation rate. The expression ($U-V_\theta$) is the relative velocity between the rotating fibers and the fluid as it traverses the bundle. The term $\frac{\mu}{k}\left(U - V_\theta\right)$ represents the drag force per unit volume and is expressed as a linear function of the relative velocity between the fluid and the fibers. The model assumed an isotropic

porous medium with the permeability, *k* derived from the Blake-Kozeny porous media model $k = \frac{d_f \varepsilon^2}{150\,(1-\varepsilon)^2}$ [80] where d_f, is the fiber diameter, ε is the bundle porosity, μ_e is a Brinkman viscosity that assumes matching of the shear stress at the fluid-fiber interface [80] defined as $\mu_e = \mu(1 + 2.5(1-\varepsilon))$, μ is the viscosity of the fluid. In addition to angular velocity, the fluid moves through the bundle in the radial direction. The radial velocity was calculated by dividing the flowrate by the bundle cross-sectional area $V_{rad} = \frac{Q}{2\pi r \varepsilon L}$.

For Generation I, the boundary condition at the inner radius of the fiber bundle was zero angular velocity, V_θ=0 because the diffuser and bundle rotate together. The boundary condition at the outer radius of the fiber bundle was constant shear stress determined as $\tau = \mu \frac{\omega R_o}{\delta_{gap}}$ where R_o is the outer radius of the fiber bundle, and δ_{gap} is the gap width between the rotating bundle and stationary housing. For the Generation I prototype, R_o = 3.5 cm and δ_{gap} was 10 mm. The left hand side of Equation 5.1 was assumed to be zero because a dimensional analysis indicated that the left hand side was an order of magnitude lower than either the drag force or the shear force. Equation 5.1 was solved using the built in ordinary differential solver 'ODE23' in MATLAB. The solution to this equation is the absolute angular velocity of the fluid. The relative angular velocity was determined by subtracting the absolute angular velocity from the fiber bundle velocity: $V_{\theta,rel} = U - V_\theta$. The gas exchange of the rotating fiber bundle was then calculated by the relationship

$$V_{CO2} = k_w A \Delta P_{LM} \qquad \textbf{(5.2)}$$

In this equation, k_w is the mass transfer coefficient in water, A is the fiber bundle surface area, and $\Delta P_{LM} = \frac{(P_{in} - P_{out})}{\ln\left(\frac{P_{out} - P_g}{P_{in} - P_g}\right)}$ is the log-mean partial pressure difference between the CO_2 in the water and the gas within the fibers. The mass transfer coefficient was determined from an empirical correlation of the form: $Sh = a\,\mathrm{Re}^b\,Sc^{1/3}$ [81, 82] where Sh is the Sherwood number, Re is the Reynolds number, and Sc is the Schmidt number. The Sherwood number is defined as: $Sh = \frac{k_w d_f}{\alpha_w D_w}$ where αw is the solubility of CO_2 in water and D_w is the diffusivity of CO_2 in water. The coefficients a,b depend on the fiber bundle geometry and were determined experimentally in a stationary fiber bundle by measuring the gas exchange as a function of flowrate. The details of determining the coefficients a,b are described in Chapter 9. The Reynolds number is defined as $\mathrm{Re} = \frac{\rho V_{rel} d_f}{\mu}$ where d_f is the diameter of an individual fiber, ρ is the fluid density and μ is the fluid viscosity. The magnitude of the relative velocity (angular and radial) was determined as $V_{rel} = \sqrt{V_{\theta,rel}^{\ 2} + V_r^2}$. The expression for the mass transfer coefficient becomes:

$$k_w = a\alpha_w D_w^{\ 2/3} d_f^{(b-1)} \upsilon^{(1/3-b)} \left(V_{rel}\right)^b \qquad \textbf{(5.3)}$$

This expression was inserted into Equation 5.2 at each rotation rate to predict the gas exchange of the rotating fiber bundle.

The model was evaluated at 3 L/min and assumed that the sweep gas flow was high enough that the partial pressure of CO_2 in the fibers was P_g=0. Figure 5.1 is a plot of the relative angular velocity in the Generation I fiber bundle normalized to the radial velocity at 750 RPM versus the normalized radial distance into the bundle. At the inner radius (r/h = 0), the fluid enters the bundle with zero relative angular velocity because the diffuser and fiber bundle rotate together. According to the model, the angular relative velocity remains zero throughout the bundle because the fluid is entrained in the rotating fiber except in the 10% of the bundle nearest the stationary housing (r/h = 0.9 through r/h =1). The model predicts that the shear stress caused by the stationary housing penetrates into the bundle and creates a relative velocity that is 60% of the radial velocity in the outer fiber layer. The CO_2 removal in Generation I as a function of rotation is shown in Figure 5.2 along with the experimental measurements at 3 L/min. The predictions are consistent with the gas exchange measurements that rotation had no effect on gas exchange.

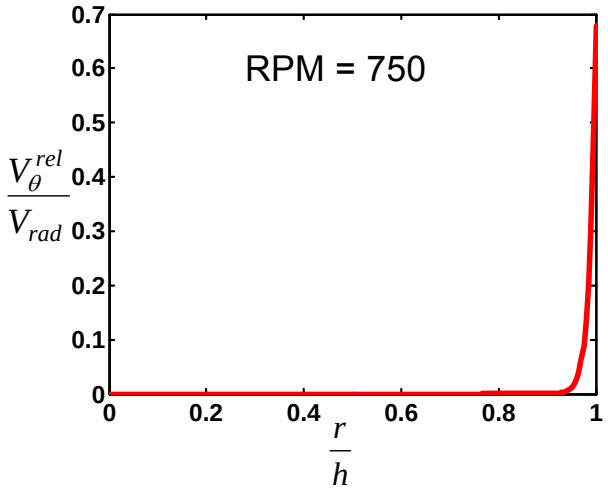

Figure 5.1: Generation I – Normalized relative velocity as a function of normalized radial distance into fiber bundle.

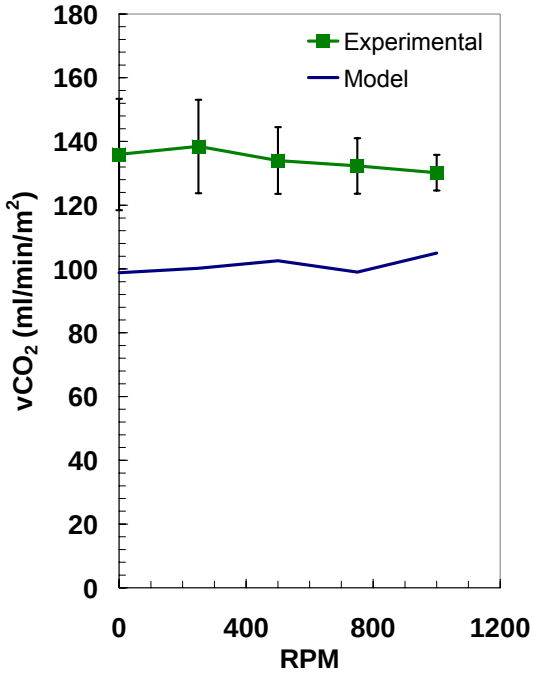

Figure 5.2: Generation I – Gas exchange predictions compared to experimental measurements.

Although gas exchange was independent of rotation, the model predicted that relative angular velocity was present in the outer 10% of the fiber bundle (1-3 layers).

The mathematical model was also used to predict the relative velocity in the Generation II prototype. The boundary condition at the inner radius of the fiber bundle was $V_\theta = \omega R_i$ consistent with the angular velocity of the rotating diffuser. The model predicted relative angular velocity decreased exponentially to zero within the first 1-3 layers of the fiber bundle. The gas exchange prediction was independent of rotation consistent with the experimental measurements. In the Generation II prototype the model predicted that the drag force was significantly higher than the shear stress within the bundle which resulted in zero relative velocity throughout most of the bundle. We used selective perfusion experiments to investigate the penetration of relative angular

velocity into the fiber bundle predicted by the model and evaluate gas exchange as a function of rotation in the fiber layers adjacent to the surfaces surrounding the fiber bundle.

5.3 SELECTIVE PERFUSION – GENERATION I AND II

The mathematical model predicted that relative velocity existed in the fiber layers adjacent to the stationary wall surrounding the fiber bundle in Generation I and the fiber layers adjacent to the rotating core in Generation II. We evaluated these predictions experimentally by measuring gas exchange in specific layers of the fiber bundle. This method has been called selective perfusion and has been used previously to obtain localized measurements of CO_2 removal in different regions of the bundle in a pulsating balloon catheter [83]. Fiber layers were blocked off using either pressure sensitive adhesive (tape) rings or silicone sealant. Figure 5.3 is a schematic of the cross-section of the fiber bundle with the fibers open (left) and selective perfusion of the inner layer (middle) and selective perfusion of the outer layer (right).

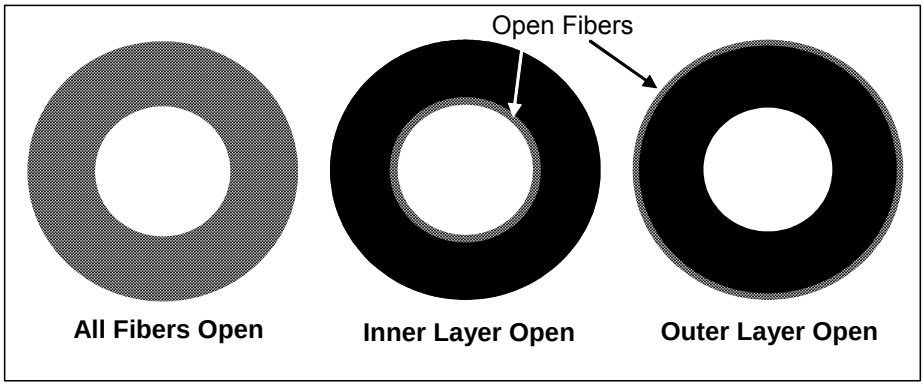

Figure 5.3: Schematic of selective profusion for Generation I and II.

For the Generation I prototype, we measured the gas exchange in the outer 1-3 layers adjacent to the stationary housing by blocking off the remaining inner fiber layers with pressure sensitive adhesive. We measured gas exchange in the inner 5-10 layers adjacent to the rotating core by blocking off the outer fiber layers with pressure sensitive adhesive (Figure 5.3). For the Generation II prototype, we measured the gas exchange for the inner 1-3 fiber layers adjacent to the rotating core by blocking off the outer fiber layers with silicone sealant (Figure 5.3 – middle bundle).

The surface area was verified by measuring the pressure drop versus flowrate of sweep gas through the unblocked regions of the bundle. The bundle was submersed in a water reservoir with one end placed just above the water level so that the fiber lumens were open to atmosphere. The submersed end of the bundle was connected to a custom cap that sealed the fibers from water at one end of the cap and enabled gas flow through a 3/8" connector at the other end of the cap. The fiber bundle was clamped to the reservoir to hold the bundle securely without getting water into the open end of the fibers. Sweep gas flowed through the bundle under positive pressure applied by a pump and flowrate was controlled with a needle valve upstream of the bundle. The pressure was measured upstream of the custom endcap using a manometer (Dwyer Model 202.5, range 0-2 in H_20). The number of fibers was then determined as $\#\ fibers = \frac{128\mu LQ}{\Delta P \pi d_f^4}$ where μ is the viscosity of the sweep gas, L is the length of the fiber bundle, Q is the sweep gas flowrate, ΔP is the pressure drop across the bundle, and d_f is the inner fiber diameter. The gas exchange surface area was determined

as $SA = \#\ fibers * \frac{\pi}{4} d_f^4$. The surface area was averaged over all the sweep gas flow rates tested.

During the selective perfusion experiments, the gas exchange loop was the same as that described in Chapter 3. Selective perfusion studies for Generation I and Generation II were performed at 1.5 L/min and 23º C. The sweep gas flowrate through each region during the selective perfusion experiments was 6.5 L/min. The surface area for each fiber region tested in the selective perfusion experiments was independent of gas flowrate and is shown in Figure 5.4.

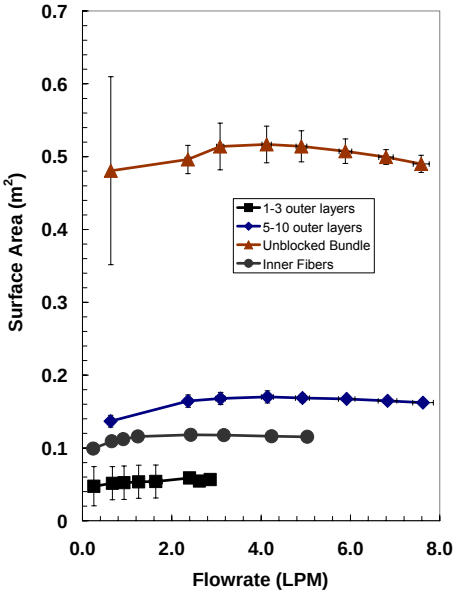

Figure 5.4: Generation I – Surface area measurements during selective perfusion experiments for different regions in the fiber bundle.

The actual surface area of the unblocked fiber bundle was 0.42 m^2 based on the number of fibers used to manufacture the fiber bundle producing an error of 16%. The measured surface area of the fiber regions is shown in Table 5-1.

Table 5-1: Surface area based on sweep gas flow measurements in selective perfusion experiments.

Fiber Layers (Generation I)	Measured Surface Area (m^2)
All layers	0.50 +/- 0.01 m^2
Outer 1-3 Layers	0.05 +/- 0.00 m^2
Outer 5-10 Layers	0.16 +/- 0.01 m^2
Inner 5-10 Layers	0.11 +/- 0.01 m^2

The CO_2 removal per area for the outer 1-3 layers increased with rotation from 286 +/- 4 ml/min/m^2 at zero rotation to 428 +/- 3 ml/min/m^2 at 1500 RPM (Figure 5.5). The inner 5-10 layers potted to the rotating core exhibited no increase in gas exchange with rotation and exhibited CO_2 removal per area of 221 ml/min/m^2 at zero rotation to 231 +/- 2 ml/min/m^2 at 1500 RPM.

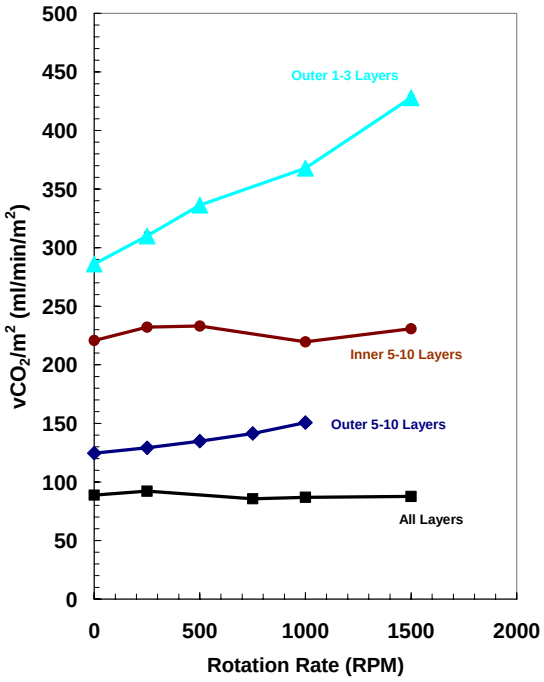

Figure 5.5: Selective perfusion in Generation I at a water flowrate of 1.5 L/min.

The selective perfusion experiments were consistent with the model prediction in Generation I. The shear stress generated by the stationary housing surrounding the bundle resulted in relative angular velocity within the outer 1-3 layers of the fiber bundle resulting in a 50% increase at 1500 RPM over the stationary bundle. Deeper into the fiber bundle 5-10 layers, gas exchange was still a function of rotation, but only increased by 20%. The fibers adjacent to the rotating diffuser (inner 5-10 layers) exhibited no effect of gas exchange with rotation because the shear stress at the wall did not penetrate deep enough into the fiber bundle. We are uncertain as to the source of the error in the surface area measurements. We speculated that entrance and exit effects of the sweep gas flowing through the fibers may have contributed to the error, but these effects would be on the order of $\sim\rho V_{gas}^2 \sim 10^{-6}$ mmHg at the highest flowrate. The measured pressure drop was on the order of 2 mmHg, so we eliminated minor losses as the cause of the error. The method of blocking the fibers with pressure sensitive adhesive rings may have introduced error because the rings were cut with a razor blade making the jagged edges at the periphery of the rings. When viewed under the microscope, partial fibers were blocked which would not have been taken into account in the surface area calculation. We believe the error in surface area calculation prevents direct comparison of gas exchange rates between different fiber regions, but does not affect comparisons of gas exchange rates for a given region at different rotation rates. The gas exchange rate curves in Figure 5.5 may shift up or down depending on the surface area, but the effect of rotation was not affected by the error in surface area measurement.

We used silicone sealant to block off outer fibers in the Generation II prototype in an attempt to better seal the fiber layers than with the tape in Generation I. The outer layers were blocked leaving the inner layer open for gas flow. The surface area calculated from the sweep gas pressure drop measurements in Generation II prototype decreased with sweep gas flowrate and on average was 0.01 +/- 0.00 m^2 (Figure 5.6). The inner layer adjacent to the rotating core exhibited an increase in CO_2 removal with rotation from 834 +/- 2 ml/min/m^2 at zero rotation to 1186 +/- 1 ml/min/m^2 at 1500 RPM (Figure 5.7). Relative angular velocity was present in the inner fiber layer but drops to zero as fluid moves radially through the bundle.

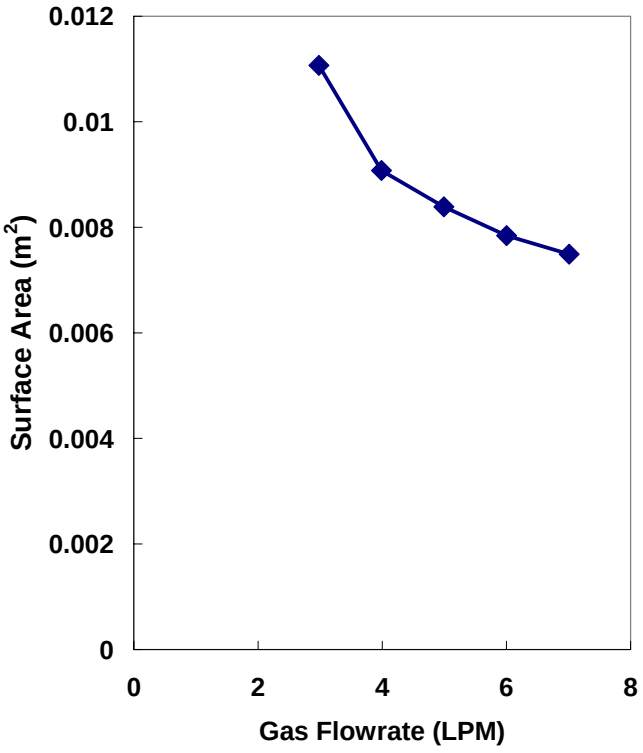

Figure 5.6: Surface area of Generation II inner layer based on pressure drop versus sweep gas flowrate measurements.

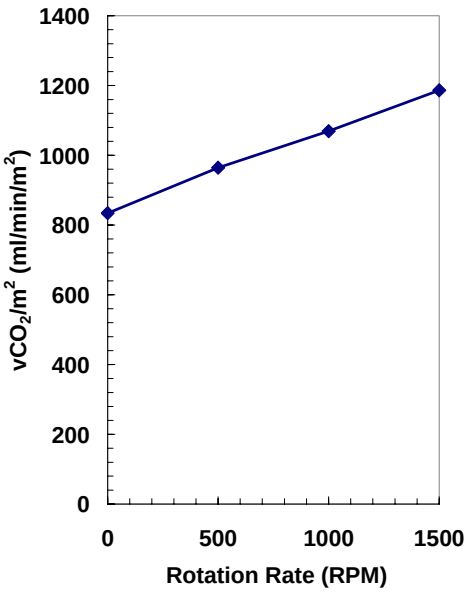

Figure 5.7: Selective perfusion of Generation II.

5.4 MODEL PREDICTIONS – GENERATION III

We evaluated the model predictions in the Generation III device which had a longer, thinner fiber bundle than the Generation I and II prototypes and had shear stress imposed at both the inner and outer surface due to stationary surfaces on either side of the bundle. The boundary conditions at the inner and outer radius of the fiber bundle were constant shear stress $\tau = \frac{\mu\omega\overline{R}}{\overline{\delta}_{gap}}$ where $\overline{R}$ is the average radius of the bundle (3.4 cm) and $\overline{\delta}_{gap}$ is the average gap thickness between the stationary surfaces and the fiber bundle (0.3 cm). Figure 5.8 is a plot of the relative velocity in the Generation III design normalized to the radial velocity within the bundle at 1500 RPM versus the normalized radial distance into the bundle. At the inner radius of the bundle (r/h = 0), the model

predicted that the fluid enters the fiber bundle with a relative velocity that is 90 times the radial velocity. The model predicted that the relative velocity quickly drops to nearly zero within the first 20% of the bundle then increases as the fluid reaches the outer radius near the outer stationary wall. The model predicted fluid entrainment in the bundle with most of the relative angular velocity and gas exchange occurring at the inner and outer fiber layers. The gas exchange prediction is shown in Figure 5.9 with the gas exchange measurements. The model predictions were within 5% of the experimental measurements. Based on the model predictions, we expected that only the two inner and two outer layers to exhibited gas exchange enhancement during rotation of the fiber bundle. Due to entrainment of the fluid beyond the second layer, we expected gas exchange to be independent of rotation for the middle three layers. We evaluated the penetration of relative angular velocity into the fiber bundle through selective perfusion experiments.

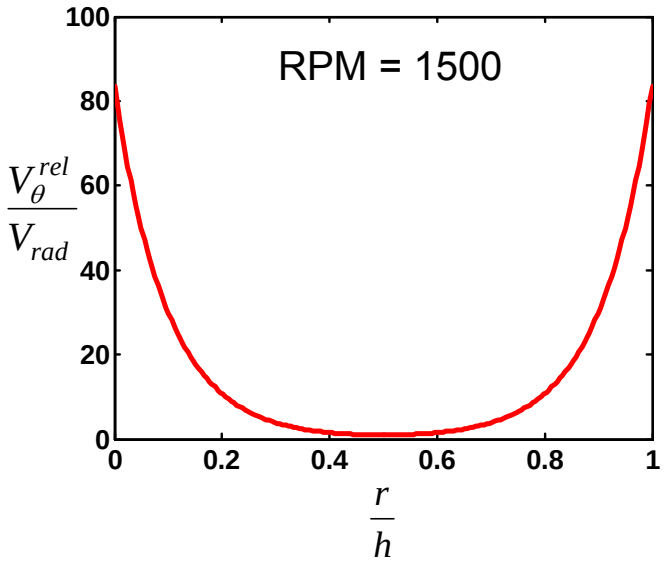

Figure 5.8: Generation III – Normalized relative velocity as a function of normalized radial distance into fiber bundle.

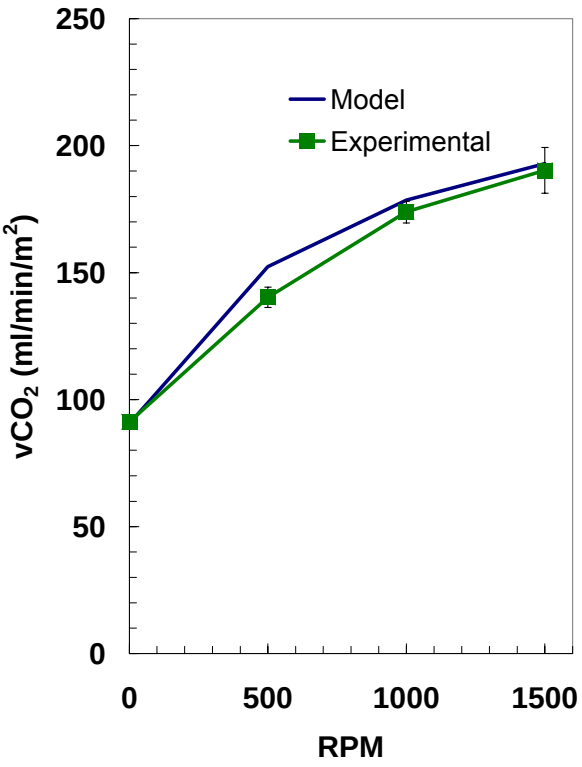

Figure 5.9: Theoretical CO_2 removal as a function of rotation rate.

5.5 SELECTIVE PERFUSION – GENERATION III

We selectively perfused gas through different fiber regions by blocking off layers with silicone sealant at the potted ends. The surface area of the unblocked fiber region in Generation III was estimated by viewing the fiber potting under a microscope and counting the number of unblocked fibers to reduce the error in surface area measurements that were encountered in the Generation I selective perfusion studies. Three different fiber layers were tested: the inner fiber layer adjacent to the stationary diffuser, the middle layer of fibers, and the outer fiber layer adjacent to the stationary

housing (Figure 5.10). The selective perfusion studies for Generation III were performed at 3.0 L/min and 37º C. The sweep gas flow was 6.5 L/min for each fiber region.

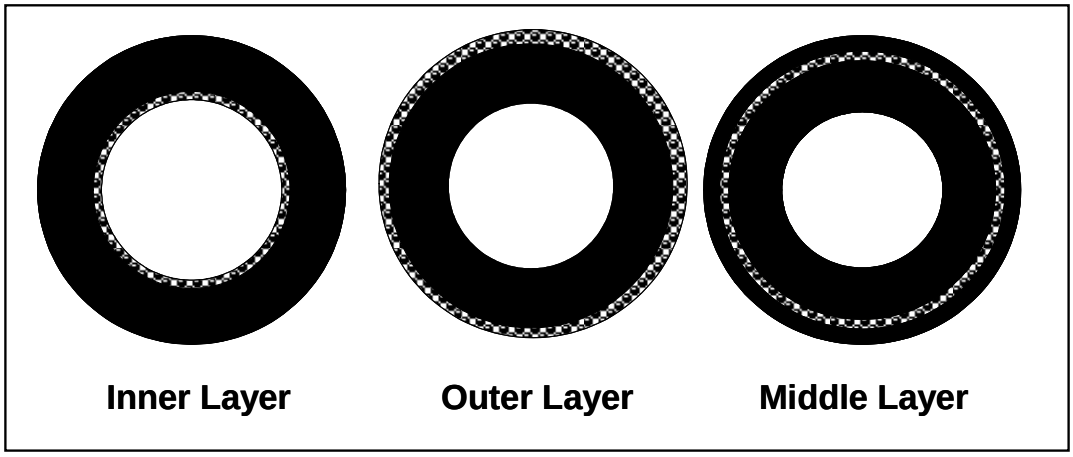

Figure 5.10: Selective perfusion for Generation III.

The gas exchange per area increased for each fiber layer as a function of rotation rate of the bundle (Figure 5.11). The middle layer exhibited the greatest overall gas exchange of nearly 650 ml/min/m^2 at 1500 RPM. The gas exchange per area varied at zero RPM from 151 +/- 4 ml/min/m^2 for the outer fibers, 208 +/- 1 ml/min/m^2 for the inner fibers, and 233 ml/min/m^2 for the middle fibers. Although we blocked off the fibers with silicone, we attribute the variation in gas exchange at zero RPM to the error in the surface area estimation. The middle layer of fibers was blocked off by two silicone regions which may not have fully blocked the fibers near the middle layer. Any additional open fibers would contribute to gas exchange, but not be included in the surface area determination. The effect of rotation is significant in all layers of the fiber bundle, but the magnitude of the gas exchange in each layer may contain significant error due to the surface area variation.

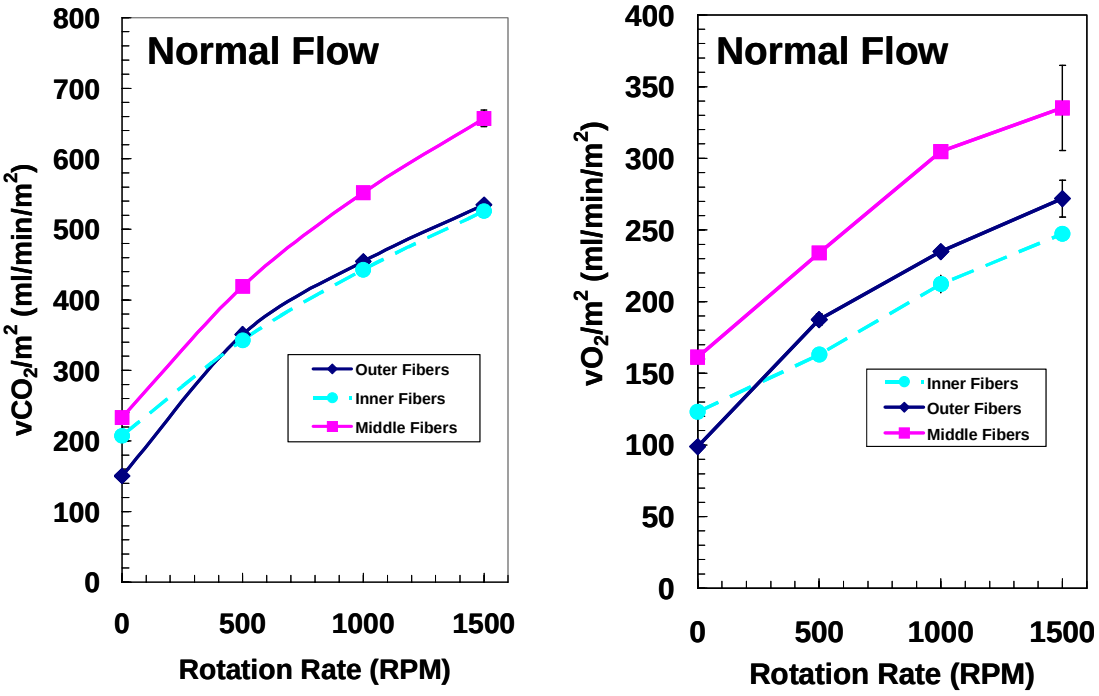

Figure 5.11: Selective perfusion for the original fiber bundle for normal flow. Left: CO_2 removal per area; Right: O_2 supplied per area.

The gas exchange in the outer layer was the highest when the data was normalized as the percent increase over zero rotation (Figure 5.12). The inner fiber layer CO_2 removal increased 153% at 1500 RPM compared to zero RPM, the middle fiber layer increased 182%, and the outer layer increased 255%.

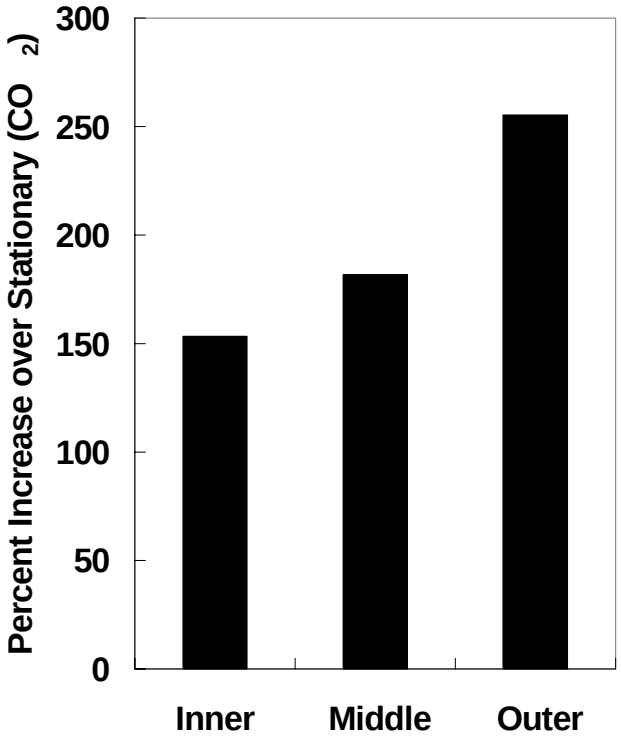

Figure 5.12: Percent increase over stationary case for different layers of the fiber bundle.

The large effect of rotation in the middle fiber layer was not predicted by the mathematical model of relative velocity, yet the gas exchange predictions matched the experimental measurements to within 5%. The model appears to have over predicted relative velocity near the stationary walls and under predicted relative velocity within the middle layers of the fiber bundle. The over prediction at the inner and outer layers of the bundle would suggest that the shear stress at the boundary between the fibers and the gap was not correct. The Brinkman viscosity in the porous media model is a correction factor to allow the assumption of continuous shear stress between the fluid in the gap surrounding the fiber bundle and the fluid in the fiber bundle. The correlation we used was based on spherical particles in a packed bed reactor and this may not be the

correct effective viscosity for an oxygenator fiber bundle. We believed that the model could be made more accurate by determining the correct effective viscosity for the oxygenator fiber bundle. The relative velocity in the middle fiber layers was dictated by the permeability of the fiber bundle. The Blake-Kozeny approximation of permeability may not have been valid for the PRAL fiber bundle. By determining the correct permeability, we believed that the model could be made more accurate and correctly predict the relative velocity profile within the bundle. Despite the discrepancy between the model and the gas exchange results, the model appeared to capture the physics of gas exchange enhancement due to the rotating fiber bundle.

Increasing the relative velocity in the fiber bundle may be achieved by reducing the drag force per volume, $F_D = \frac{\mu}{k}(U - V_\theta)$ acting on the fluid elements. One way to decrease the drag force is by increasing the permeability of the fiber bundle. One way to increase the permeability of the fiber bundle is to increase the porosity. In Chapter 6.0, the effect of increasing the fiber bundle porosity is explored in the mathematical model, and then tested experimentally by manufacturing fiber bundles with increased porosity.

5.6 SUMMARY

A mathematical model was developed to calculate the relative velocity in the fiber bundle based on an angular momentum balance. The relative velocity is a function of the relative magnitudes of the shear and drag forces acting on the fluid within the bundle. The fiber bundle was modeled as a porous medium using an empirical

permeability coefficient that was a function of the fiber bundle porosity. In the Generation I prototype, the model predicted that the relative velocity was zero throughout the entire fiber bundle except in the outer fiber layer next to the stationary outer housing. The model agreed with the experimental result that gas exchange was not a function of rotation in the Generation I prototype. We tested the model prediction that relative velocity was present in the outer layers by performing selective perfusion experiments where the inner fiber layers were blocked and gas exchange was measured in only the outer layers. The selective perfusion experiments were consistent with the model prediction. The outer 1-3 layers exhibited an increase in gas exchange with rotation while the inner layers did not.

In the Generation III prototype, the model predicted that relative velocity was present in the inner and outer 20% of the fiber bundle and zero in the middle of the fiber bundle. The gas exchange predictions were within 5% of the experimental measurements. The selective perfusion experiments were not consistent with the model prediction that the relative velocity is near zero in the middle of the bundle. Experimentally, the middle layer of fibers exhibited a 175% increase in gas exchange at 1500 RPM over the stationary case. We speculated that the model was not accurately predicting the relative velocity because the length scale of the porous media model was on the order of magnitude as the penetration distance of the relative velocity. Since the gas exchange predictions were within 5%, we believed that the model was overpredicting the relative velocity at the inner and outer surfaces and underpredicting the relative velocity in the middle layers. Despite the discrepancy between the model and selective perfusion experiments, the model appeared to explain the mechanism behind gas exchange

enhancement in the PRAL. We used the model to investigate the effect of increasing the fiber bundle porosity to increase the penetration of relative velocity into the bundle. These studies are discussed in Chapter 6.

6.0 EFFECT OF FIBER BUNDLE POROSITY ON GAS EXCHANGE

6.1 INTRODUCTION

The mathematical model discussed in Chapter 5 predicted that the drag force of the rotating fiber bundle entrained the fluid elements within the bundle reducing the relative angular velocity between the fibers and the fluid. We hypothesized that increasing the spacing between the fibers (porosity) would decrease the drag force and generate higher relative velocity to increase the overall gas exchange efficiency of the device. In order to decrease the drag force in the model, the porosity was increased from 0.43 to 0.83 by increasing the fiber bundle thickness from 0.2 cm to 0.4 cm (decreasing the inner radius of the bundle from 3.3 cm to 3.1 cm) to simulate more spacing between the fiber layers. The model predictions of relative velocity are shown in Figure 6.1 for the Generation III prototype with a porosity of 0.43 and the bundle with a porosity of 0.83. According to the model, as porosity is increased, the fluid becomes less entrained within the rotating bundle. The predicted normalized relative velocity at the inner radius increased from 90 for a porosity of 0.43 to over 500 for a porosity of 0.83. The penetration of relative velocity into the fiber bundle also increased with higher porosity. The relative velocity went to nearly zero within the first 20% of the fiber bundle when the porosity was 0.43. When the porosity was 0.83, the model predicted that the relative velocity remained high in the bundle for the first 40% of the bundle.

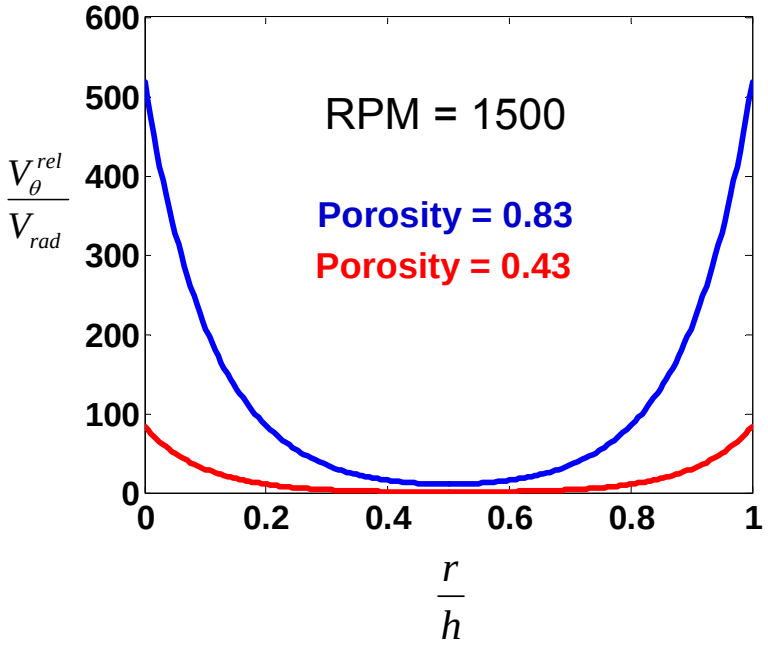

Figure 6.1: Mathematical model predictions of relative velocity in the fiber bundle for porosities of 0.83 (top line) and 0.43 (bottom line).

The gas exchange prediction as a function of rotation is shown in Figure 6.2. The model predicted a 50% increase in gas exchange at no rotation and a 40% increase in gas exchange at 1500 RPM for the bundle with the higher porosity. The model predicted that with a porosity of 0.83, the fiber bundle removes all CO_2 in the water above 500 RPM. Therefore, the CO_2 removal above 500 RPM in Figure 6.2 reached a plateau of 112 ml/min. We tested this prediction by fabricating fiber bundles with increased porosity.

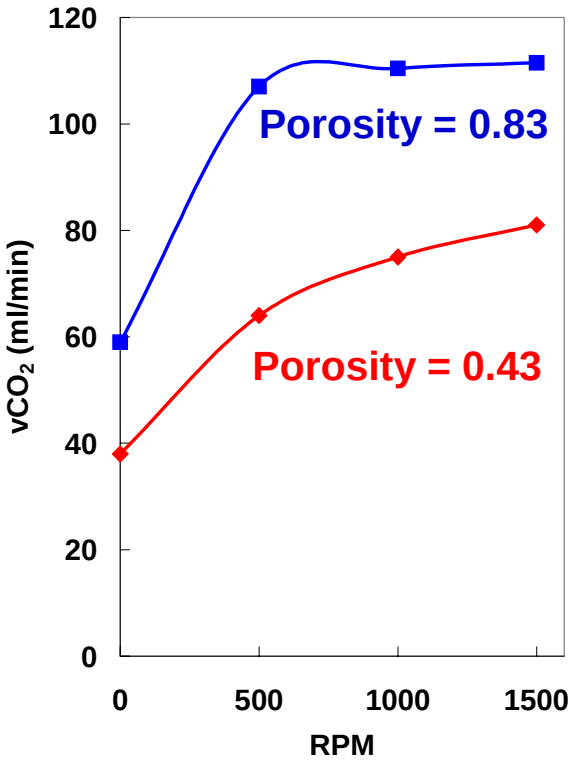

Figure 6.2: Mathematical model predictions of gas exchange in the fiber bundle for porosities of 0.83 (top line) and 0.43 (bottom line).

The model prediction that an increase in porosity at zero rotation results in higher gas exchange seems counter-intuitive. Gas exchange at zero rotation is dictated by the radial velocity, $V_{rad} = \frac{Q}{2\pi r \varepsilon L}$. An increase in porosity from 0.43 to 0.83 would decrease the radial velocity by a factor of nearly 2. In order to increase porosity, the thickness of the bundle was increased from 0.2 cm to 0.4 cm. The increased thickness of the bundle increases the residence time that a fluid particle spends in the fiber bundle. The residence time is given by $t_{res} = \frac{V_{bundle}}{Q}$ where V_{bundle} is the volume of the fiber bundle. An increase fiber bundle thickness of 0.2 cm results in a 93% increase in residence time. Therefore, the increased residence time in the higher porosity bundle resulted in an

increased gas exchange prediction at zero rotation. We tested the mathematical model prediction of increased gas exchange with porosity by manufacturing fiber bundles with increased porosity.

6.2 METHODS

We manufactured four fiber bundles, two with a porosity of 0.43 and two with a porosity of 0.83. All fiber bundles were made with fibers that had an outer diameter of 300 μm. Felt strips 0.8 mm thick were cut to the same width as the potting region of the bundle (1 cm). The strips were placed into the fiber bundle in the potted region during manufacturing by laying the strips on the fiber mat and winding the strips and mat together onto the porous support cage. Felt material was used because of its porous nature to allow the potting glue to saturate and hold the strips in place forming radial gaps between each row of fibers (Figure 6.3). The strips increased the spacing between the fibers layers in the radial direction and hence increased fiber bundle porosity. A summary of the fiber bundle dimensions is given in Table 6-1. The 'Original' bundle was wrapped without spacers using 54 fiber per inch mat. The porosity was 0.43 and the surface area was 0.42 m^2. The bundle labeled 'Spacers' had 0.8 mm thick felt strips placed between each fiber layer. Figure 6.3 is a microscopic view of the fiber bundle potting for the Original bundle and the Spacers bundle. The strips can be seen between each fiber layer.

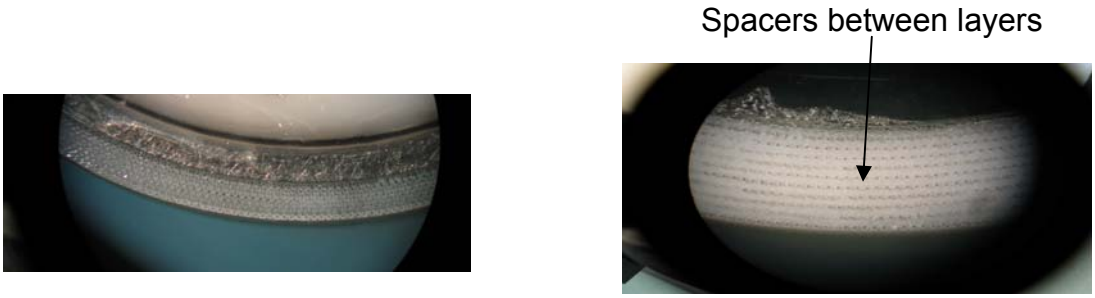

Figure 6.3: Microscopic view of (a) Original fiber bundle (no spacers); and (b) Bundle with spacers.

The 'Varied Porosity' device was fabricated to investigate the effect of the spacing between fibers in both the radial and angular directions. This bundle consisted of 17, 35, and 54 fiber per inch mats in 11 total rows: the inner and outer layer of fibers were 17 fibers per inch, the next three rows from the inner and outer layers were 35 fibers per inch, and the middle three rows were 54 fibers per inch. The surface area of this bundle was also 0.42 m^2 and the porosity was 0.83. Another bundle was fabricated to investigate the effect of the wefts which hold the fibers evenly spaced. This bundle had the same dimensions as the Original bundle, but every other row of wefts was removed.

Table 6-1: Fiber bundle characteristics.

	Original	Spacers	Varied Porosity	Wefts Removed
Surface Area (m^2)	0.42	0.5	0.42	0.42
Porosity	0.43	0.83	0.83	0.43
Layer spacing (mm)	N/A	0.8	0.8	N/A
Fiber Spacing (fpi)	54	54	17,35,54	54
Wefts Present	Yes	Yes	Yes	½ removed

6.3 GAS EXCHANGE RESULTS IN WATER – EFFECT OF POROSITY

Porosity did not increase the gas exchange efficiency of the PRAL. The gas exchange for the four fiber bundles in water flowing at 3 L/min is shown in Figure 6.4 for rotation rates from 0 to 1500 RPM. All four fiber bundle designs exhibited an increase in gas exchange with rotation. At 1500 RPM, the Original design had the highest CO_2 exchange efficiency of 190 +/- 9 ml/min/m^2 and the Varied Porosity bundle had the lowest CO_2 efficiency of 172 +/- 7 ml/min/m^2. The O_2 gas exchange efficiency trended the same as the CO_2 efficiency with the Original design exhibiting the highest O_2 exchange efficiency of 120 +/- 2 ml/min/m^2 and the Varied Porosity bundle exhibiting the lowest O_2 efficiency of 103 +/- 0 ml/min/m^2 at 1500 RPM.

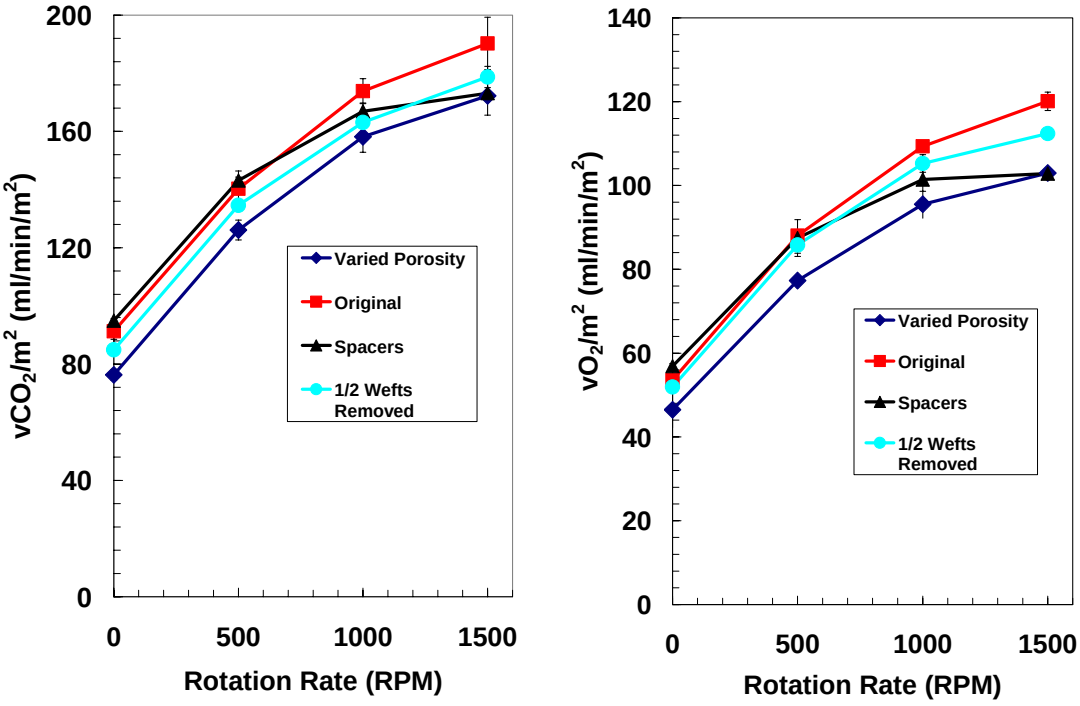

Figure 6.4: CO_2 and O_2 transfer in water for different fiber bundle designs.

The gas exchange results in Figure 6.4 contradicted the model prediction that an increase in fiber bundle porosity would increase the gas exchange efficiency of the PRAL. We attributed the discrepancy to the length scale of the porous media model being the same as the length scale of the fiber strips that were placed in the bundle. The diameter of an individual fiber (0.3 mm) was the length scale of the model compared to the thickness of the felt strips of 0.8 mm. Since both length scales were on the same order of magnitude, the model was not able to accurately resolve the penetration distance of relative velocity in the fiber bundle. A computational fluid dynamics (CFD) model was developed to look at the flow around individual fibers undergoing shear induced flow. The CFD model enabled us to investigate the effect of adding spacers between fiber bundle layers and resolve the penetration distance of relative velocity into the bundle.

6.4 CFD MODEL

We developed a CFD model of individual fibers undergoing shear flow and compared the model to the analytical model developed in Chapter 5. The purpose of the model was to simulate the moving fibers next to the stationary housing to investigate the penetration of relative velocity in the fiber bundle and compare the prediction to the porous media model. The geometry of the CFD model of the Original fiber bundle is shown in Figure 6.5.

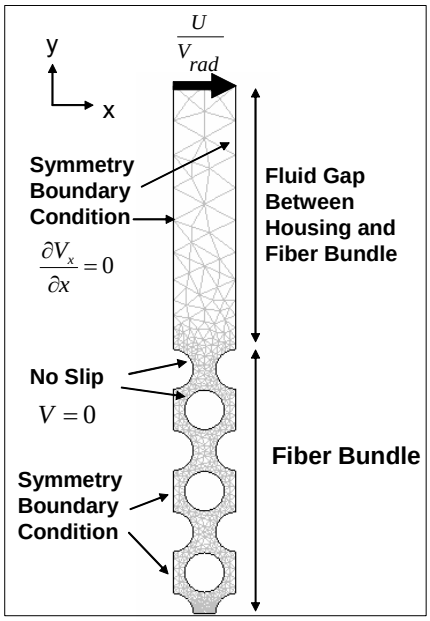

Figure 6.5: Mesh of fiber bundle used in CFD model.

The geometry consisted of seven fiber layers, a fluid gap above the fibers, and moving solid wall above the gap. The dimensions were chosen to model the dimensions of the fibers, gap, and housing in the PRAL. The moving wall above the fibers generates shear induced relative velocity between the fluid and the fibers similar to rotating the fiber bundle of the PRAL. The x-direction velocity was normalized to the radial velocity and corresponded to the angular velocity in the PRAL. The symmetry boundary condition $\frac{\partial V_x}{\partial x} = 0$ was applied on all vertical surfaces. The geometry was made from 5040 elements. FEMLAB software®, a finite element-based partial differential equation solver was used to solve the Navier-Stokes equations neglecting gravity forces:

$$\rho \frac{D\vec{v}}{Dt} = -\nabla P - \mu \nabla^2 \vec{v} \qquad \textbf{(6.1)}$$

The no-slip velocity condition was imposed on the surface of each fiber as shown in Figure 6.5. The Original bundle and the Spacer bundle were simulated, and the data was plotted as the relative angular velocity normalized to the radial velocity.

6.5 CFD MODEL RESULTS

The x-direction (angular) velocity contours are shown in Figure 6.6 for the Original Bundle (left) and the bundle with Spacers (right). The model predicted that the fluid velocity went to zero within the first layer of fibers for both bundles and remained zero throughout all layers of the fiber bundle. Therefore, the relative angular velocity did not penetrate past the first fiber row. Figure 6.7 is a comparison between the analytical and the CFD model predictions of the normalized angular velocity versus the distance into the bundle. The analytical model predicted that the normalized relative velocity decreased from 90 to 20 in the first fiber row. The CFD model predicted that the relative velocity decreased from 14 to 0 halfway into the first row of fibers. The comparison between the analytical model and the CFD model for the Spacers bundle is shown in Figure 6.8. The analytical model predicted that the normalized relative velocity decreased from 500 to 325 in the first fiber row whereas the CFD model predicted the angular velocity dropped from 14 to 0 within the first fiber row.

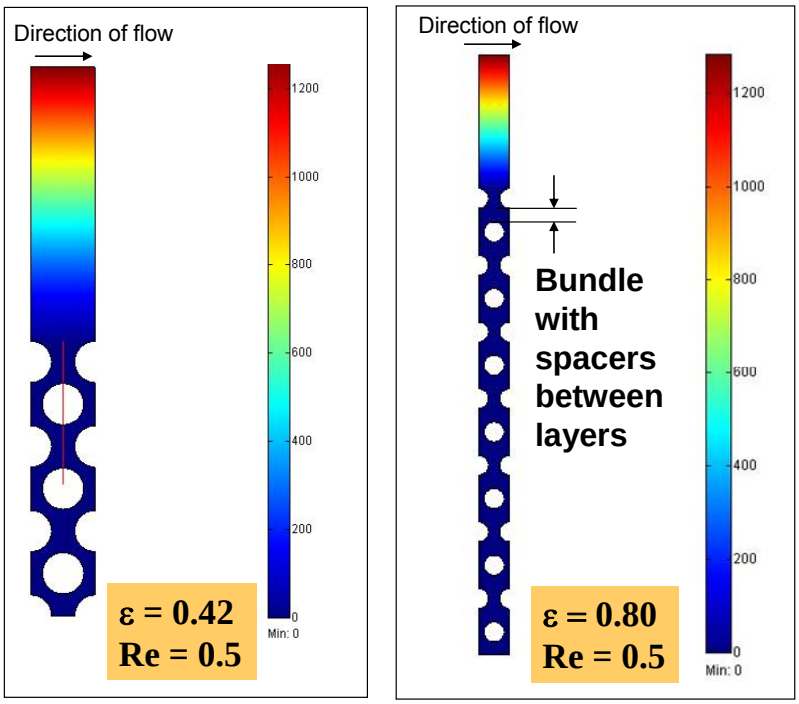

Figure 6.6: CFD Velocity profiles of Original Bundle (left) and Bundle with Spacers (right).

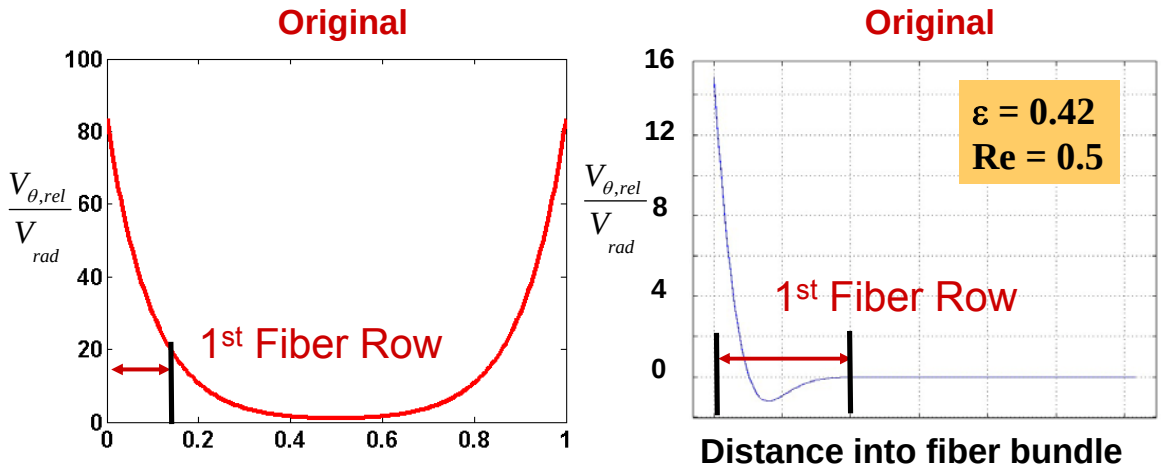

Figure 6.7: Comparison of angular relative velocity prediction for original fiber bundle: analytical model (left) and CFD model (right).

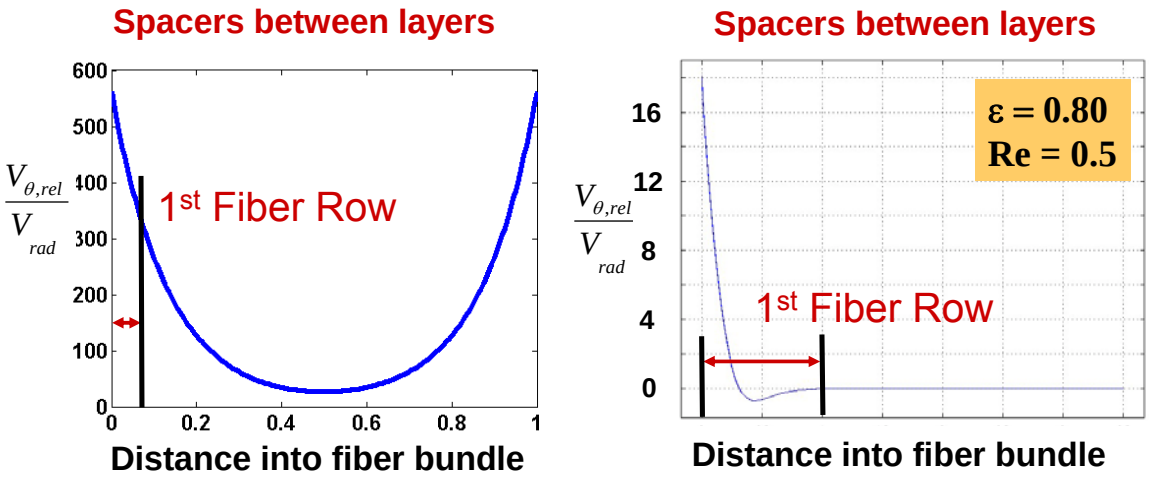

Figure 6.8: Comparison of angular relative velocity prediction for Spacers fiber bundle: analytical model (left) and CFD model (right).

The large discrepancy between the analytical model and the CFD model predictions confirmed that the scale of the porous media model could not resolve the effect of adding spacers to the fiber bundle. The CFD model was consistent with the experimental result that adding increasing the porosity of the fiber bundle by adding spacers did not increase the relative velocity in the fiber bundle and therefore did not increase gas exchange. However, the CFD model did not explain why the middle layers of fibers exhibited an increase in gas exchange with rotation in the selective perfusion studies presented in Chapter 5. We hypothesized that the rotating fiber bundle was creating recirculation currents (Taylor vortices) in the outer gap resulting in relative velocity throughout all layers of the fiber bundle. We tested this hypothesis using selective perfusion experiments in the Original fiber bundle by introducing flow in the outer gap surrounding the fiber bundle instead of the radially through the fiber bundle (Figure 6.9). If Taylor vortices were the cause of increased gas exchange then the inner and middle fibers would exhibit an increase in gas exchange with rotation when flow

was introduced in the outer gap. If Taylor vortices were not the cause of increased gas exchange, then the inner and middle fiber layers would not exhibit and increase in gas exchange with rotation when flow was introduced in the outer gap.

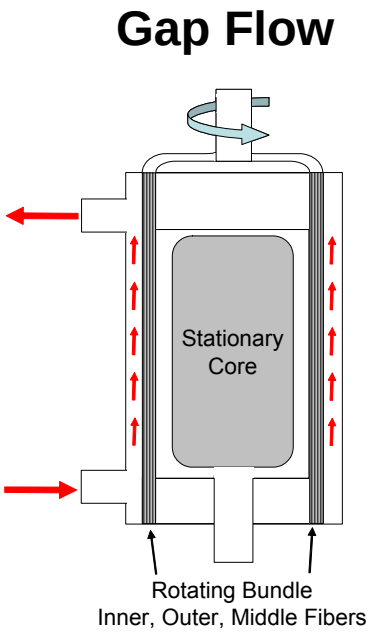

Figure 6.9: Schematic of gap flow during selective perfusion studies.

The gas exchange studies were performed using the same setup as that described in Chapter 3. The gas exchange rates for the gap flow selective perfusion experiments for the inner, middle, and outer layers are shown in Figure 5.10. The gas exchange increased with rotation for all layers of the fiber region suggesting that vortices in the outer gap penetrate into the fiber bundle and enhance gas exchange (Figure 6.10). Due to the uncertainty in surface area of the unblocked fiber layers (see Chapter 5), the data was normalized as the percent increase over zero rotation (Figure 6.11). The gas exchange in the outer layer was higher than the middle and inner when the data was normalized in this manner. At 1500 RPM, the inner layer increased 162% over the

stationary case, the middle layer increased 199%, and the outer layer increased 251% over the stationary case.

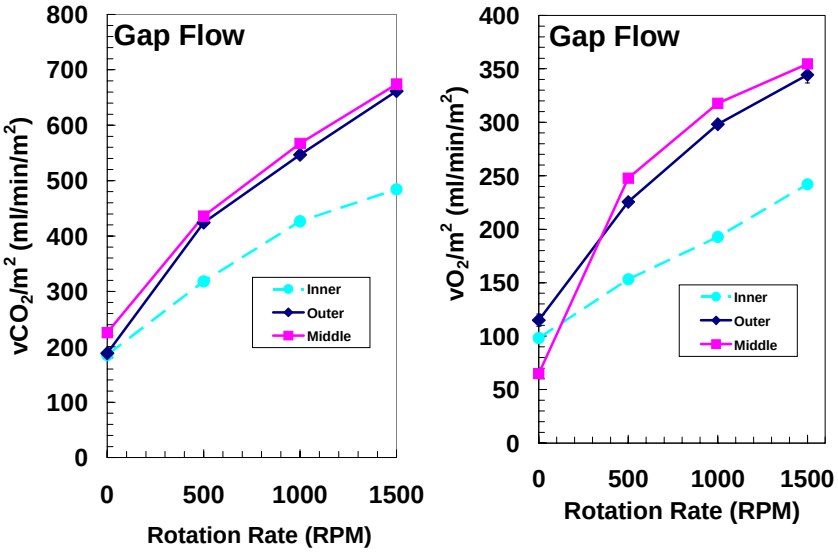

Figure 6.10: Selective perfusion for the original fiber bundle for gap flow. Left: CO_2 removal per area; Right: O_2 supplied per area.

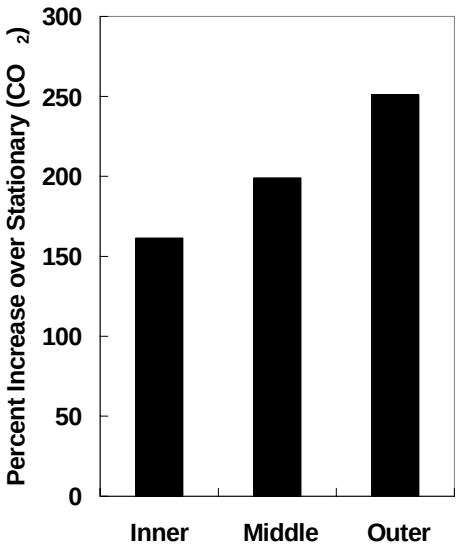

Figure 6.11: Percent increase in CO_2 removal per area over stationary case with flow introduced in the outer gap.

Taylor vortices caused by the rotating fiber bundle appear to be the cause of increased gas exchange in the PRAL. The vortices form in the gap between the rotating bundle and stationary outer housing and penetrate throughout the fiber bundle. The effect of the vortices on gas exchange decreased from the outer to inner layers (Figure 6.11). As fiber bundle thickness increases, the penetration of vortices would likely decrease which explains why gas exchange was not a function of rotation in the thicker fiber bundles in the Generation I and II prototypes.

We investigated the fluid dynamics in the PRAL using flow visualization and Particle Image Velocimetry (PIV) to gain a better understanding of the mechanism for increased gas exchange in the PRAL.

6.6 PARTICLE IMAGE VELOCIMETRY (ADAPTED FROM [84])

We used particle image velocimetry to investigate the flow field in the gap between the rotating fiber bundle and the stationary outer housing. The results presented in this section were obtained in a direct collaboration with Stephanus Budilarto, Ph.D. We used the images to determine the magnitude of fluid velocity. We fabricated a flat surface from clear acrylic that mounted onto the side of the PRAL housing halfway between the inlet and outlet of the device to enable optical access into the device. We used a Nd:YAB laser (Solo PIV III 15 Hz, New Wave Research Inc., Fremont, CA) that emitted a 532-nm laser pulse. A Kodak CCD camera (Megaplus ES 1.0, Eastman Kodak Company, San Diego, CA) and a 60 mm cylindrical lens (Edmund Optics, Barrington, NJ) was used to capture two sequential images within microseconds apart. XCAP-

standard v.2.2 imaging software (EPIX Inc, Buffalo Grove, IL) was used to operate the camera. Neutrally buoyant fluorescent polymer microspheres (35-6c, Duke Scientific, Palo Alto, CA) were used as the tracing particle to measure the flow field in the PRAL, which was filled with water and de-aired. The inlet and outlet of the device were clamped off, and the fiber bundle was rotated at 130, 500, and 1500 RPM. The digital camera was located directly above the PRAL with the focal region on the flat surface above the gap between the rotating fiber bundle and outer housing. An optical long pass glass filter (OG 550, Edmund Optic Inc., Barrington, NJ) was placed in front of the camera to eliminate the reflection of the laser light on the fiber bundle surface.

The fluid velocity in the outer gap was calculated from the two acquired images using fuzzy logic enhanced PIV software (PIVPROC 6.53) developed by Wernet and the US NASA Glenn Research Center. The images were divided into 64X64 pixels with 50% overlapped interrogation areas. The average instantaneous velocity in each interrogation area was calculated by dividing the average displacement of the particles by the time separation between images. Fifteen instantaneous pairs of images were used to calculate the ensemble-averaged velocity distribution of the fluid for each rotation rate.

6.7 PIV RESULTS

The fiber bundle rotation sets up Taylor vortices in the gap between the bundle and the stationary outer housing. The diameter of the vortices is roughly the width of the gap. At all rotation rates, the vortices are laminar. At 130 RPM and 500 RPM the vortices are

stable, and at 1500 RPM the vortices become wavy. Figures Figure 6.12 — Figure 6.14 are two images of velocity vectors for each bundle rotation rate at different time points and the same location in the gap between the rotating fiber bundle and the stationary outer housing. The maximum velocity for each rotation rate occurred at the point where the two vortices met. At 130 RPM, 500 RPM, and 1500 RPM, the maximum velocity was 0.9 cm/s, 4 cm/s, and 5 cm/s, respectively.

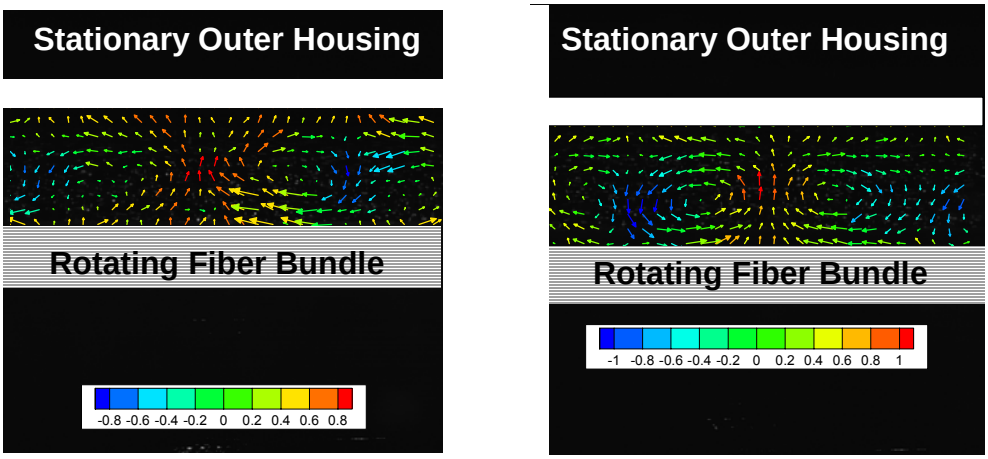

Figure 6.12: PIV measurements at 130 RPM.

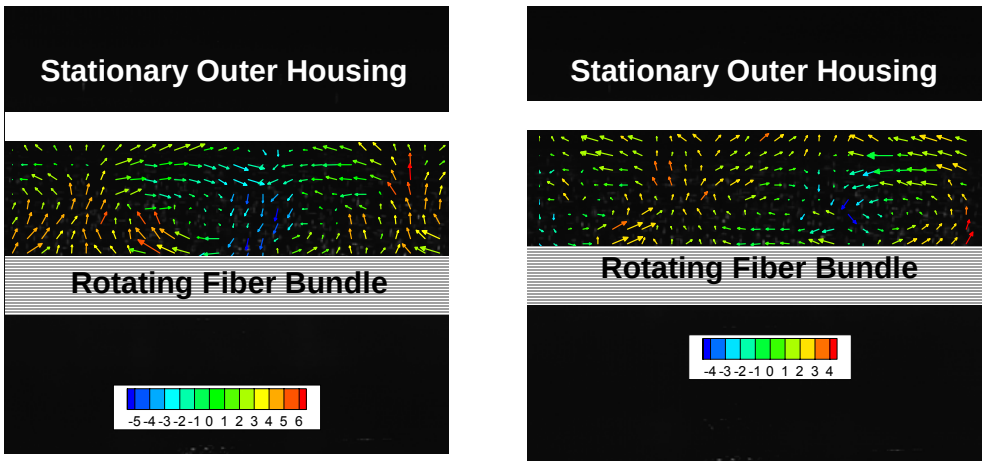

Figure 6.13: PIV measurements at 500 RPM.

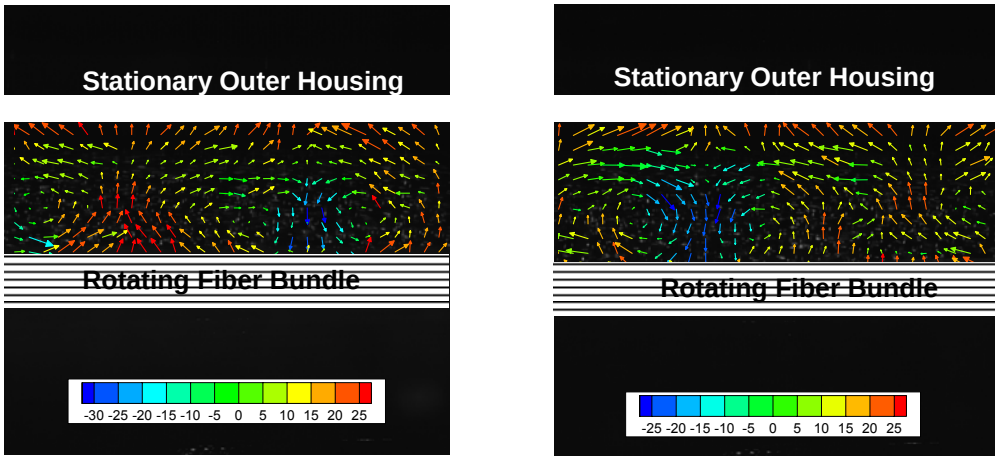

Figure 6.14: PIV measurements at 1500 RPM.

The PIV results are consistent with the current understanding of Taylor vortices in the literature [85]. Figure 6.15 is a representation of Taylor vortices in the gap between a rotating cylinder and stationary housing.

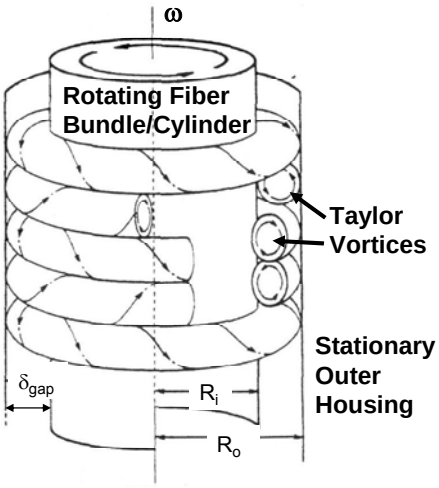

Figure 6.15. Schematic representation of Taylor Vortices.

The nature of the vortices changes with rotation rate from laminar and steady, to laminar and wavy, and finally turbulent. The thresholds for these flow regimes are determined by the Taylor number:

$$Ta = \frac{\varpi R_i (R_o - R_i)}{\upsilon}\left(\frac{R_o - R_i}{R_i}\right)^{1/2} \quad \textbf{(6.2)}$$

Steady Vortices: 40 < Ta < 800

Wavy Vortices: 800 < Ta < 2000

Turbulent Vortices: 2000 < Ta < 10000-15000

Turbulence: Ta > 15000

In the PRAL, the maximum Taylor number was 1300, and as shown in the PIV images, the flow was laminar. Although velocity measurements cannot be made within the fiber bundle, the vortices appear to be penetrating into the fiber bundle. The selective perfusion studies verified the penetration of the vortices since all layers of the Generation III fiber bundle exhibited gas exchange with rotation. We conclude that the Taylor vortices are the mechanism behind gas exchange enhancement in the PRAL.

The analytical model from Chapter 5 predicted that increasing the porosity of the fiber bundle would increase the relative velocity between the fibers and the fluid and therefore increase gas exchange efficiency. To test the model, we manufactured two fiber bundles with porosities greater than the Original PRAL fiber bundle and one fiber bundle with half of the wefts removed and measured the gas exchange of all the bundles in water. The gas exchange rates were the same for all fiber bundle designs thus contradicting the analytical model predictions.

6.8 SUMMARY

We developed a CFD model to investigate the penetration of relative velocity into the fiber bundle due to the shear flow in the case of a moving surface next to the fiber bundle. The plot of the velocity of the fluid in the bundle showed that the relative velocity between the fluid and the fibers goes to zero within the first layer of fibers. Increasing the spacing between the layers as we did in the 'Spacer' fiber bundle did not change the result that relative velocity is zero beyond the first fiber layer. The CFD model is consistent with the experimental result that adding spacers between the layers did not enable relative velocity to penetrate into the fiber bundle. We hypothesized that the enhanced gas exchange in the middle fiber layers was due to Taylor vortices that form in the gap between the rotating fiber bundle. We verified the presence of vortices using PIV and found that the magnitude of the velocity in the vortices is on the same order of magnitude as the radial velocity in the bundle.

7.0 HEMOLYSIS

7.1 INTRODUCTION

Hemolysis, or the destruction of red blood cells, is a concern for any blood contacting medical device. Hemolysis occurs when a blood cell is exposed to shear stress for a long enough period of time to rupture the cell. After cell rupture, the free hemoglobin binds with haptoglobin, and the hemoglobin-haptoglobin complex is then scavenged and degraded by monocytes or macrophages. However, if the levels of plasma free hemoglobin exceed 130-160 mg/dL in vivo, the scavenging mechanisms become saturated, hemoglobinuria occurs, and organ failure soon follows [86, 87].

Hemolysis has been studied extensively in the blood pump industry. Many variables play a role in the design of the pump and have an impact on hemolysis. For example, the seals and bearings have been shown to cause hemolysis due to heat generation caused by the friction of the rotating shaft against the seal [88, 89]. The clearance between the impeller and the casing has been shown to affect hemolysis because of the exposure of blood cells to high shear stress. The shape and rotation rate of the impeller also has an impact on hemolysis [90, 91].

Computational fluid dynamics (CFD) has become an important tool for designing blood pumps. Investigators have calculated the pathlines of particles flowing through the pump and predicted hemolysis from an empirically derived correlation involving shear stress and exposure time of a blood element moving along the pathline [92-107]. Investigators have been able to redesign the geometry of the pump to reduce hemolysis by reducing the exposure time of blood elements to shear stress.

For CFD simulations of the PRAL, computational power is not sufficient to model each individual fiber within the rotating fiber bundle. One approach to overcoming computational limitations is to approximate the fiber bundle as a porous media. Shear stress within the bundle would be calculated based on an average superficial velocity as an approximation to the local velocity around the fibers in the rotating bundle. Another approach is to model the individual fibers in a smaller section of the fiber bundle. This approach would more accurately resolve the velocity around the individual fibers, and would require proper scale-up of the domain to accurately predict the influence of the entire bundle on hemolysis. We believe that the shear stress within the bundle may not be traumatic to blood cells due to the entrainment of the fluid in the rotating fiber bundle. A more important application of CFD in the PRAL would be to investigate the shear stress in the gap between the rotating bundle and stationary outer housing. The exposure time of a fluid particle to shear stress in this gap varies as the particle moves through the vortices in the gap. Future studies of the PRAL using CFD will focus on determining the magnitude of shear stress in the gap to predict hemolysis. CFD will be a useful tool for reducing hemolysis in the PRAL. Blood experiments must still be performed to fully understand the impact of design changes on hemolysis.

This chapter details the in vitro evaluation of hemolysis in the PRAL and several variables that we investigated for their contribution to hemolysis. These variables included the seals, the shear stress in the outer gap between the fiber bundle and housing, the shear stress in the inner gap between the diffuser and fiber bundle, the support cage, and the outlet port. We concluded that the seals did not contribute significantly to hemolysis. The shear stress in the gap between the rotating fiber bundle and stationary outer housing did not contribute to hemolysis, but the surface roughness of the fiber bundle may be responsible for increased levels of hemolysis. The inner gap between the rotating bundle and the stationary diffuser was not a source of hemolysis and neither was the outlet port. A support cage made of circular struts exhibited higher hemolysis than a support cage made of a porous sheet.

7.2 MATERIALS AND METHODS

The in vitro hemolysis evaluation of the PRAL was performed by comparing the level of plasma free hemoglobin generated by the PRAL to the level generated by a commercially available oxygenator. The control loop consisted of a blood reservoir (Affinity Blood Reservoir, Medtronic, Minneapolis, MN), a commercially available oxygenator (Terumo Capiox or the Cobe Optima) and a Biomedicus pump (BPX-80, Medtronic, Minneapolis, MN). The integral heat exchanger in the oxygenator was used to maintain the temperature at 37 C. The flowrate through the control loop was 4 L/min. The PRAL loop consisted of a main loop containing the same blood reservoir as the control loop, a Biomedicus pump, and a bypass loop which branched off of the main

loop via a Y-connector. The bypass loop contained a pediatric heat exchanger and the PRAL. The rationale for this setup was to simulate the in vivo situation where only a fraction of the cardiac output flows through the PRAL. The main loop simulated the cardiac output of the patient (4 L/min), and the bypass loop was run at 0.75 L/min to test how a fraction of the cardiac output through the PRAL would affect overall hemolysis. Schematics of the control and PRAL loops is shown in Figure 7.1.

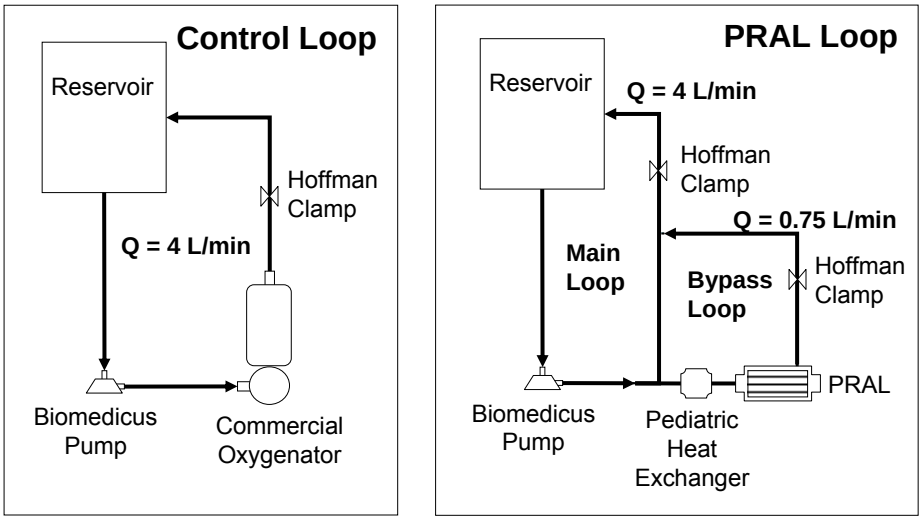

Figure 7.1. Schematic of mock circulatory loops used for in vitro hemolysis testing: control loop (left); PRAL loop (right).

Blood was collected at a local slaughterhouse and anticoagulant citrate dextrose (ACD) was added in a concentration of 9:1 (blood:ACD) to prevent clotting. The blood was filtered with 40 μm pore size filters (Pall Biomedical, Inc., Fajardo, PR) on the day of collection to remove any hair or extraneous particles due to the collection process, and Gentamycin (0.1 g/mL) was added to prevent infection. Blood was added to each loop and circulated until the temperature reached 37 C. The priming volume of each loop was 1.5 L. The fiber bundle was rotated at 1500 RPM, and the flowrate was adjusted

with a Hoffman clamp. Samples (4 ml) were drawn from each loop every half hour for the first 2 hours and every hour thereafter for the duration of the 6-hour evaluation. Each sample was used to measure hematocrit and plasma free hemoglobin. Hematocrit was measured with a capillary tube spun down for 3 minutes in a microhematocrit centrifuge (International Equipment Co., IEC MB, Needham Hts, MA). The remainder of the sample was spun down in a centrifuge at 3400 RPM for 15 minutes. The supernatant plasma was siphoned off into an Eppendorf tube and spun down again at 10000 RPM for another 15 minutes. The purified plasma was transferred to a cuvette and analyzed in a spectrophotometer (Thermo Spectronic Genesys 5) at a wavelength of 540 nm. The absorption of light by the spectrophotometer was calibrated to known levels of PfHb.

We measured the increase in PfHb over time for the PRAL device, and then changed one variable and repeated the test to determine the effect of the variable on hemolysis. Reassembly of the PRAL was required to test each variable, so different batches of blood were used for each test, and the tests were performed on different days with the same control loop for each test. To determine the effect of the seals, we removed the seals and replaced them with delrin rings leaving a 0.005” clearance between the rings and the rotating shaft. Saline was perfused into the gap at a flowrate of 10 ml/hr to prevent blood from contacting the bearings. To test the effect of shear stress in the outer gap, we cut the fibers out of the device and rotated the porous support cage. In a separate test, we increased the gap from 2 mm to 6 mm by reducing the fiber bundle diameter from 7.0 cm to 6.2 cm. The effect of the surface roughness of the fiber bundle was investigated by testing a smooth solid core cylinder made of acrylic with the same

dimensions as the fiber bundle (outer radius 7.0 cm). The effect of the inner gap on hemolysis was investigated by removing the stationary center diffuser. Two different cage designs were investigated to determine their contribution to blood damage in the PRAL. One cage was made of six stainless steel struts, and the second cage was fabricated from a porous stainless steel sheet formed into a cylinder. The two cage designs are shown in Figure 7.2.

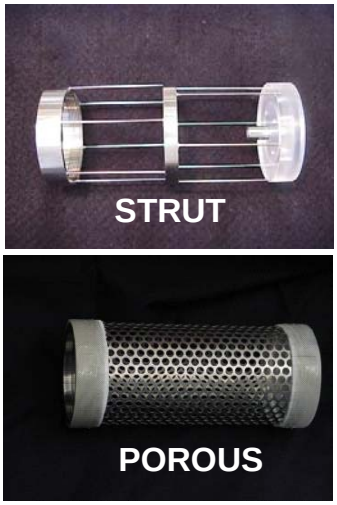

Figure 7.2: Two fiber support structure designs (cages).

The effect of the cage was evaluated in an earlier PRAL prototype with only 0.25 m^2 surface area and the setup did not contain a bypass loop. All other tests contained the bypass loop and the surface area was 0.42 m^2 if fibers were present. Both loops were flushed with tap water immediately after the test to rinse any remaining blood out of the circuit.

The normalized index of hemolysis (NIH) is one common index of blood damage. For the control loop, NIH was expressed according to the equation

$NIH = \frac{\Delta PfHb \cdot V \cdot (1 - HCT/100)) \cdot 100}{\Delta t \cdot Q}$ where ΔPfHb was the change in plasma free hemoglobin level, V was the priming volume of the circuit, HCT was the Hematocrit of the blood sample, Q was the flowrate of blood, and Δt was the time duration of the test. In clinical practice, the flowrate through the pump and oxygenator in the control loop, is at or near the cardiac output of the patient. Therefore, in these studies the NIH for the control loop was normalized to the flowrate through the device, Q. During clinical use of the PRAL, only a fraction of the cardiac output will flow through the PRAL and will then mix with the venous return of the patient. The total liberated hemoglobin in the blood of the patient will be only a fraction of that caused by the PRAL. Therefore, the increase in plasma free hemoglobin in these studies was normalized by the cardiac output in a typical patient, or the flowrate through the main loop, Q_M. The NIH for the PRAL loop was defined as $NIH_P = \frac{\Delta PfHb \cdot V \cdot (1 - HCT/100)) \cdot 100}{\Delta t \cdot Q_M}$ where Q_M was the flow through the main loop. Normalizing the data by Q_M enabled a more appropriate comparison between the control oxygenator that captures all cardiac output of the patient and the PRAL which only captures a fraction of the cardiac output of the patient.

7.3 RESULTS AND DISCUSSION

The hemolysis of the PRAL was compared to a commercially available oxygenator that is routinely used in applications such as CPB and ECMO. The rationale for these experiments was that if in vitro hemolysis levels in the PRAL were comparable to hemolysis levels in a commercially used oxygenator then the PRAL would be more

likely to be safe to use in vivo from a blood damage standpoint. In the comparison test between the PRAL and the commercial oxygenator, we found that the increase in PfHb in the PRAL was substantially higher than in the control loop. The PfHb levels for the PRAL with the fiber bundle rotating at 1500 RPM increased from 34 mg/dL to 333 mg/dL (Figure 7.3) with a NIH_P of 0.24. The increase in PfHb in the control loop was from 34 mg/dL to 81 mg/dL, with an NIH of 0.03 g/100L.

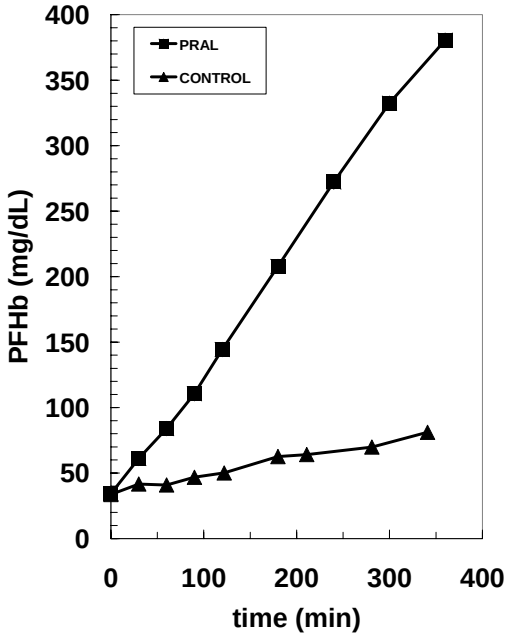

Figure 7.3: Hemolysis for the PRAL.

The increase in PfHb in the PRAL relative to the control indicated that blood damage could be a serious concern in the PRAL. We systematically evaluated specific components within the PRAL for their contribution to hemolysis. The first variable tested was the seals that prevent blood from entering the gas pathway. The hemolysis test was repeated with the three blood contacting seals removed from the PRAL. The PfHb level versus time for the PRAL without the seals is shown in Figure 7.4. Removing the

seals did not reduce hemolysis in the PRAL. The plasma free hemoglobin level increased from 30 mg/dL to 332 mg/dL. The seals were determined not to be the source of hemolysis in the PRAL since PfHb increased the same as when the seals were present.

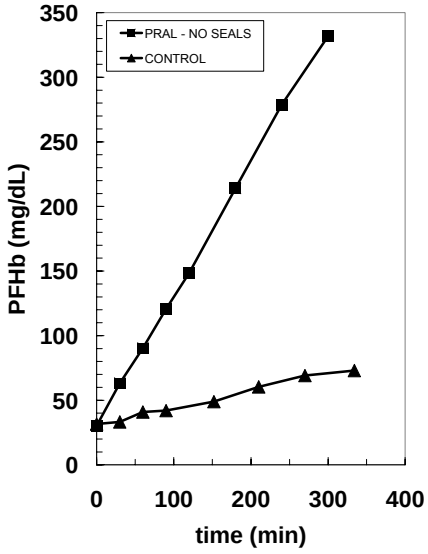

Figure 7.4: Hemolysis for the PRAL without seals.

Heat generation is a common problem in blood pumps that contain seals around a rotating shaft [108, 109]. Infusion of heparinized saline around the rotating shaft can flush the area with fresh fluid to reduce heat and stagnation [110, 111]. Seals made of ferromagnetic fluid are another solution that shown promise in minimizing blood damage [109]. Finally, a magnetic coupling could also be used to rotate the bundle to eliminate the seal and bearing altogether [112, 113]. Seals are necessary in the PRAL to protect the bearings from blood contact and prevent air embolism from the sweep gas. The current design of the PRAL contains four seals, three of which contact blood. Two of the seals are placed into the endcaps of the device and the third seal is seated between the

stationary core and the rotating fiber bundle. Clinically available blood pumps have incorporated a fluid purge system to wash the seal, which reduces heat generation and stasis next to the seal [114-116]. We investigated the role of the seals on hemolysis in the PRAL by removing the three blood contacting seals and purging saline through the gaps to prevent blood from contacting the bearings. The bearing between the rotating bundle and stationary core could not be purged with fluid and did contact blood. The increase in plasma free hemoglobin was the same with or without the seals. The bearing that was contacting blood was in a region between the stationary core and the rotating fiber bundle seated into the gas pathway cap by 3 mm. We believe that although blood was contacting this bearing, hemolysis was not affected by this bearing since it was seated 3 mm into the gas pathway cap between the stationary core and rotating bundle. We did not investigate the flow patterns in this region, but we believe that blood would have a difficult time perfusing this region. Therefore, heat generation or blood destruction remained localized to this region and did not affect overall plasma free hemoglobin levels.

The next variable that was tested was the outer gap between the rotating bundle and stationary outer housing. This gap was increased from 2 mm to 6 mm in an attempt to reduce the shear stress in the gap. The PfHb level over time is shown in Figure 7.5 and increased from 24 mg/dL to 316 mg/dL.

The PRAL with the increased gap of 6 mm had the same hemolysis as the PRAL with the 2 mm gap. Chapter 8 details a model describing the effect of increasing the gap size on shear stress. The model predicted that increasing the gap from 2 mm to 6 mm decreased the shear stress by 20%. We believe that the shear stress in the large gap

was still above the threshold to cause hemolysis resulting in substantial blood damage relative to the control.

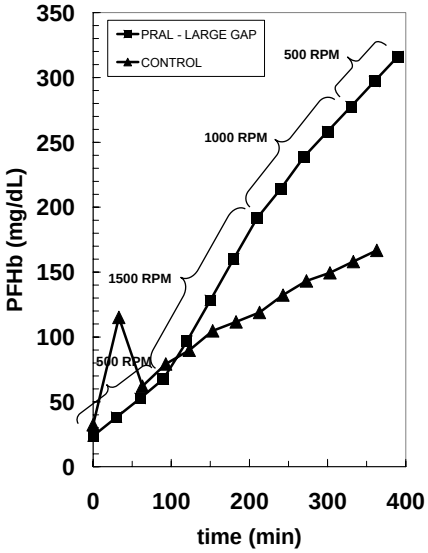

Figure 7.5: Hemolysis for the PRAL with a 6 mm outer gap.

The next experiment was performed to investigate the role of the fibers on blood damage. The PRAL was tested with the fibers removed from the porous cage. A large decrease in hemolysis was observed when the fibers were removed from the PRAL. The PfHb from went from 17 mg/dL to 98 mg/dL over 6 hours (Figure 7.6). We hypothesized that the roughness of the fiber bundle was responsible for increased shear stress in the gap between the rotating fiber bundle and stationary outer housing. We manufactured a smooth solid cylinder with the same radius as the fiber bundle (3.5 cm) to test the effect of roughness on hemolysis.

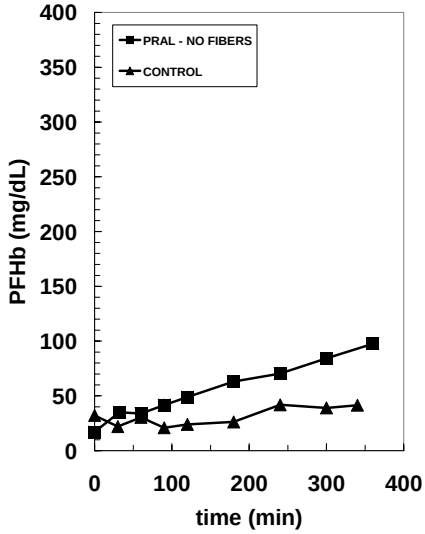

Figure 7.6: Hemolysis for the PRAL without fibers.

The PfHb level for the solid core was the same as the PRAL with the fibers removed (Figure 7.7).

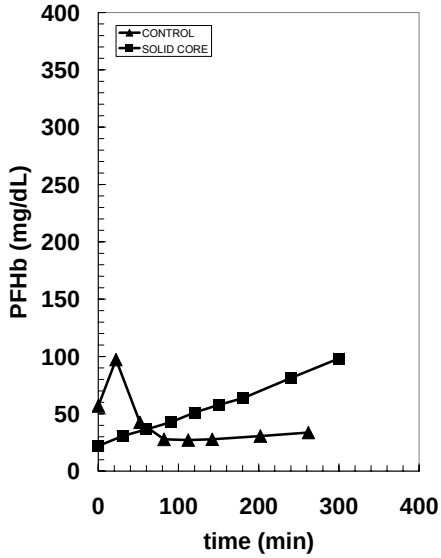

Figure 7.7: Hemolysis for the smooth cylinder.

The plasma free hemoglobin levels were greatly reduced when the fibers were removed from the PRAL. We suspect that for the device without fibers the high porosity of the

cage did not create Taylor vortices so the shear stress in the gap between the rotating cage and outer housing was much lower than when the fibers were present. However, this does not necessarily imply that Taylor vortices cause hemolysis. The solid cylinder model generated Taylor vortices but had similar plasma free hemoglobin levels as the porous cage. Therefore, we suspect that the rotating fiber bundle creates higher shear stress due to the rough surface of the bundle compared to the smooth surface of the solid cylinder model. Surface roughness has been shown to be a contributing cause of hemolysis in blood pumps [117-121]. Maruyama et al measured the shear stress in a couette viscometer and found the shear stress doubled when the roughness on cylinder was increased from 0.2 μm to 2 μm [117]. Van den Berg et al measured the effect of surface roughness on power dissipation in Taylor vortex flow and found that surface roughness increased the friction and therefore the shear stress in Taylor flow similar to the roughness of a pipe surface increases the shear stress in turbulent pipe flow [122]. In Chapter 8, we describe the effect of surface roughness on power dissipation measurements.

A summary of the blood damage presented as NIH_p due to the seals and fibers is shown in Table 7-1. We also tested the effect of the shear stress in the inner gap between the diffuser and rotating bundle by removing the stationary diffuser.

Table 7-1: Summary of NIH_p showing effect of seals and fibers in the PRAL.

Device Description	NIH Control Loop (g/100L)	NIH_p (g/100L)
Complete PRAL Device	0.03	0.24
PRAL w/o Seals	0.03	0.22
PRAL w/o Fibers	0.01	0.06
Smooth Cylinder	0.01	0.07

Removing the diffuser had no impact on hemolysis as PfHb levels increased from 48 mg/dL to 238 mg/dL (Figure 7.8).

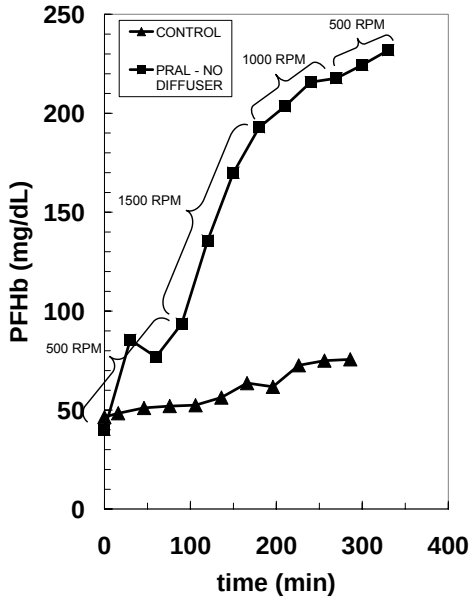

Figure 7.8: Hemolysis for the PRAL without diffuser.

Figure 7.9 is the plasma free hemoglobin versus time for the strut cage design which increased from 11 mg/dL to 645 mg/dL. The PRAL with the strut cage caused substantial blood damage relative to the control compared to the PRAL with the porous cage.

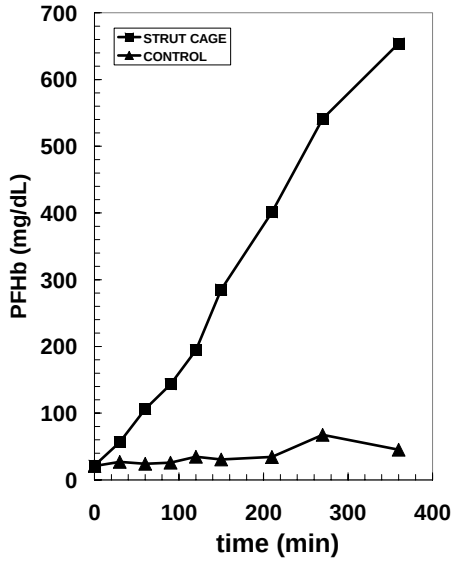

Figure 7.9: Hemolysis for the PRAL with the strut cage.

One hypothesis for the high hemolysis was that the strut cage caused localized eddies and turbulence in the wake of the struts during rotation. The flow past the struts can be described by the Reynolds number ~$(\omega R)d_s/\nu$ where ω is the rotation rate of the cage, R is the radius of the fiber bundle cage (33 mm), d_s is the strut diameter (1.5 mm), and ν is the kinematic viscosity of blood (0.023 cm^2/s). Figure 7.10 is an illustration of flow past a cylinder for a Reynolds number of 26 [123]. The flow becomes separated into two vortices in the strut wake as flow moves left to right past the cylinder. Above a Reynolds number of 100, the flow transitions into turbulence in the wake behind the cylinder. At a fiber bundle rotation rate of 1500 RPM, the Reynolds number for flow past a strut is on the order of 1000 causing flow separation and turbulence. Turbulent flow would result in higher shear stress than seen in the porous cage design and may explain the high levels of hemolysis the strut design.

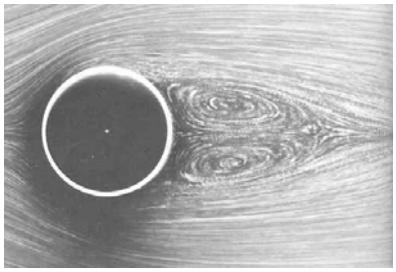

Figure 7.10: Flow around a cylinder at Reynolds number of 26.

One possible solution to reduce hemolysis caused by the fiber bundle may be to change the orientation of the fibers. Currently, the fibers are oriented so that their main axis is parallel to the axis of rotation of the bundle. However, the fibers could be wrapped in a longitudinal orientation circumferentially around the support cage, which may result in an overall reduction in the shear stress on the fibers. The change in orientation may alter the penetration of the Taylor vortices into the bundle resulting in lower overall shear stress.

Another possible solution may be to rotate a smooth, solid cylindrical core next to a stationary fiber bundle. In this design, Taylor vortices would be generated by the rotating core which would increase gas exchange, but shear stress would be lower. Van den Berg measured the power dissipation for the case of a rotating smooth cylinder within a rough stationary cylinder [122]. At all rotation rates, the rotating smooth cylinder produced lower power dissipation and therefore lower shear stress than when the rotating cylinder was roughened and the housing was smooth. The power data was normalized into a friction factor correlation and we estimate that we could expect to see a 20% decrease in shear stress by changing to a rotating smooth cylinder and a stationary fiber bundle.

The outlet port of the PRAL is a 3/8” barb-fitting tangent to the outer housing. We hypothesized that this region could be traumatic to red blood cells because of the nature of the flow in this area. The blood elements transition from being in Taylor-vortex flow caused by the rotating bundle to the outlet port. Medtronic has shown that the shape of the outlet port of the Biomedicus BP-80 pump has a dramatic effect on hemolysis [105]. Through CFD analysis of the pump outlet, Medtronic redesigned the port into a ‘cut-water’ geometry, which reduced hemolysis by 20%.

We investigated the effect of the outlet port by gluing a 2-layer patch of fibers over the outlet port and testing the hemolysis of the solid core model in an attempt to reduce the chaotic nature of the flow as it transitions to pipe flow in the outlet. We hypothesized that the two layers of fibers would create more uniform flow through the outlet port due to the resistance of the fiber layers. The PfHb levels over time for the PRAL with and without the fiber layers over the outlet port were the same (data not shown). We also increased the diameter of the outlet port from a 3/8” barb to a ½” barb. We hypothesized that by increasing the diameter; we could slow that flow down and reduce the shear stress in the vicinity of the outlet port. No difference in PfHb levels was observed for the two different port sizes (data not shown). We concluded that the outlet port was not a major source of hemolysis in the PRAL.

Although PfHb levels were much higher for the PRAL device relative to the control, several comments are warranted concerning in vitro plasma free hemoglobin tests. To our knowledge, the plasma free hemoglobin levels measured in vitro do not correlate to the performance of the device in vivo, nor does the NIH have any predictive ability as to how a medical device will perform in vivo. In vitro PfHb levels are affected by many

factors including but not limited to flowrate, blood loop priming volume, hematocrit, total protein concentration, and pH [124]. Investigators have attempted to normalize for some of the variables that can affect PfHb levels. The NIH for example was developed to analyze blood pumps that operate in flow ranges consistent with adult cardiac output. However, the NIH may not be applicable to medical devices that operate in low flow ranges. Tamari et al evaluated the effect of flowrate on the NIH in the Biomedicus BP-50 [125]. The NIH for a flowrate of 1.78 L/min was 0.029 +/- 0.005 g/100L whereas the NIH at a flowrate of 0.3 L/min was 0.135 +/- 0.022 g/100L with p=0.0000. Although the NIH is meant to normalize for the effect of flowrate on hemolysis, the NIH does not appear to be an appropriate comparison for devices that operate at different flow rates. We developed a bypass setup to better compare how the PRAL would perform in vivo relative to a device that operates near the cardiac output of the patient. The NIH_P provided a better comparison between the PRAL and the control oxygenator that captures the full cardiac output of the patient. The NIH_P was still considerably higher at 0.239 than the NIH of the control for each test indicating that hemolysis still needs to be addressed in the PRAL.

8.0 MECHANISMS FOR HEMOLYSIS

8.1 INTRODUCTION – OUTER GAP

Hemolysis is a function of shear stress and the time of exposure of red blood cells to that shear stress. When the shear stress exceeds a threshold value, the blood cell ruptures releasing hemoglobin. Several investigators have attempted to quantify the threshold level of shear stress and the exposure time that causes hemolysis. Leverett et al reported a threshold shear stress of 1500 dynes/cm^2 at an exposure time of 120 s for complete red blood cell destruction [126]. Sutera and Mehrjardi reported the threshold limit to be 2500 dynes/cm^2 at an exposure time of 240 s [127-129]. Paul et al found a threshold of 4250 dynes/cm^2 at an exposure time of 0.425 s and 3750 dynes/cm^2 at an exposure time of 1.4 s [130]. Mockros et al [32] summarized the available literature and developed a blood damage threshold based on time and shear stress: $\tau^2 = \frac{k_1}{t} + k_2$

where τ is the shear stress, t is the exposure time of red cells to that shear stress and k_1 and k_2 are empirical constants 10^4 dynes^{2}s/cm^4 and 2.2E6 dynes^2/cm^4, respectively. The threshold is shown in Figure 8.1 in the exposure time range of 0.001 s to 100 s. Above and exposure time of 0.1 s, the threshold shear stress for complete red blood cell damage is 1500 dynes/cm^2.

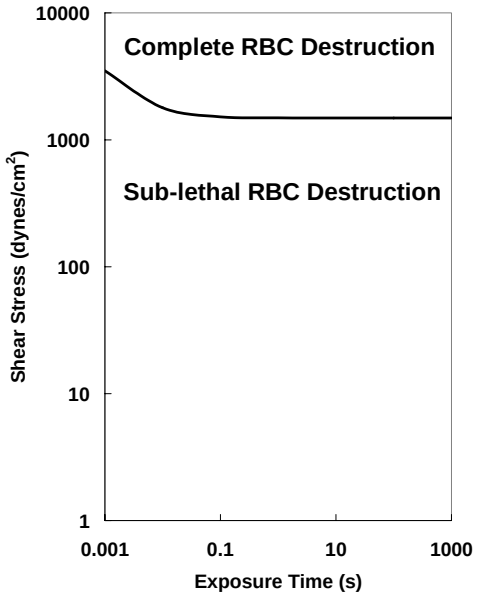

Figure 8.1: Threshold shear stress versus exposure time for complete red blood cell (RBC) destruction.

Another model has been used extensively to predict hemolysis from an empirically derived correlation involving shear stress and exposure time of a blood element moving along the pathline [92-107]. Hemolysis is expressed in terms of the change in plasma free hemoglobin (*ΔPfHb*) in mg/dL per total hemoglobin (*Hb*):

$$\frac{\Delta PfHb}{Hb} = 3.62 \times 10^{-7} \cdot \tau^{2.416} \cdot t^{0.785} \qquad \textbf{(8.1)}$$

where τ is the shear stress (Pa) acting on a fluid particle and *t* (s) is the amount of time that the fluid particle is exposed to that shear stress. This model has been used in conjunction with CFD to redesign blood pumps to reduce hemolysis. This chapter describes measurements of the shear stress in the gaps surrounding the rotating fiber bundle in an attempt to relate this shear stress to the available literature data concerning blood damage.

In Chapter 7, we evaluated the hemolysis in the PRAL and found that the primary cause of hemolysis in the PRAL appeared to be the roughness of the rotating fiber bundle. The solid cylinder and the rotating bundle both produce Taylor vortices in the outer gap, but the solid cylinder generated much lower PfHb levels than the fiber bundle. In this chapter, we measured the power dissipated into the fluid due to Taylor vortices for both the smooth solid cylinder and the fiber bundle and compared our measurements to a theoretical model. The shear stress in the outer gap was then calculated from the power measurements.

The shear stress acting on the fluid is due to the torque transferred by the motor to the rotating fiber bundle. In Taylor-vortex flow, the angular velocity decreases exponentially in the boundary layer adjacent to the rotating fiber bundle, remains constant in the center of the gap, and decreases exponentially to zero in the boundary layer adjacent to the stationary outer housing. The shear stress is maximum in the boundary layers and is very low in the region between the boundary layers where the fluid nearly rotates as a solid body (Figure 8.2) [131].

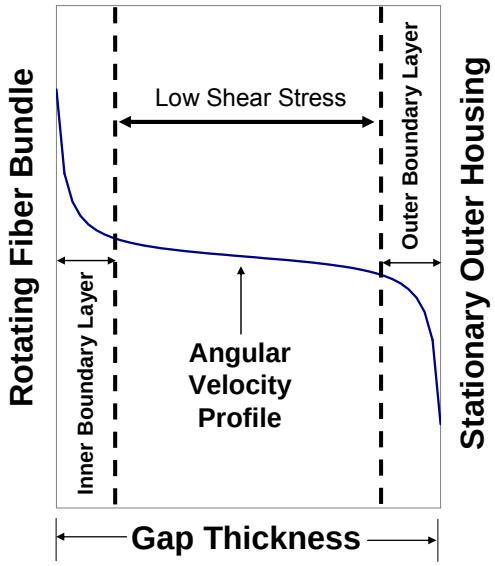

Figure 8.2: Schematic of angular velocity profile in Taylor vortex flow in the gap between the rotating fiber bundle and stationary outer housing.

The shear stress is a function of the boundary layer thickness, rotation rate, gap thickness, and torque exerted on the fluid.

Several investigators have developed empirical relationships to calculate the torque exerted on the fluid for co-rotating smooth cylinders, and from these relationships the shear stress can be determined [132]. The empirical relationship for the torque, T is:

$$T = 1.45\rho\upsilon^2 L \frac{\eta^{3/2}}{(1-\eta)^{7/4}} \mathrm{Re}^{1.5} \qquad 400 < \mathrm{Re} < 10000 \quad \textbf{(8.2)}$$

where $\eta = \frac{R_i}{R_o}$ is a dimensionless radii ratio and $\mathrm{Re} = \frac{\varpi R_i (R_o - R_i)}{\upsilon}$ is the angular Reynolds number. From the torque, the power dissipated into the fluid can be found by multiplying the torque and angular frequency: $P = \omega T$. The boundary layer thickness can be calculated by the following equation.

$$\delta = \frac{\pi R_i R_o \,\mathrm{Re}}{(R_o - R_i)G} \qquad \textbf{(8.3)}$$

where $G = \frac{T}{\rho \upsilon^2 L}$ is a dimensionless torque. Finally, the shear stress in the boundary layer is given by:

$$\tau = \rho \nu \frac{\gamma \omega R_i^2}{R_o \delta} \qquad \textbf{(8.4)}$$

where γ is the an empirically determined constant with a value of 0.5 [133]. We used this model to predict the power dissipation in the outer gap for the PRAL Generation III device. Figure 8.3 is the predicted power dissipation into the fluid surrounding the rotating fiber bundle for gap thicknesses of 2 mm and 6 mm. The fluid was water so that the model could be tested easily using a liquid with well known properties. Power dissipation increases with rotation rate and reaches 5.5 W for the 2 mm gap simulation. Increasing the gap to 6 mm decreased the power dissipation at 1500 RPM to 3.5 W. The shear stress predictions are plotted in Figure 8.4. The effect of increasing the gap size increased as the rotation rate increased. For the 2 mm gap, the shear stress at 1500 RPM was calculated to be 272 dynes/cm^2 compared to 175 dynes/cm^2 when the gap was 6 mm.

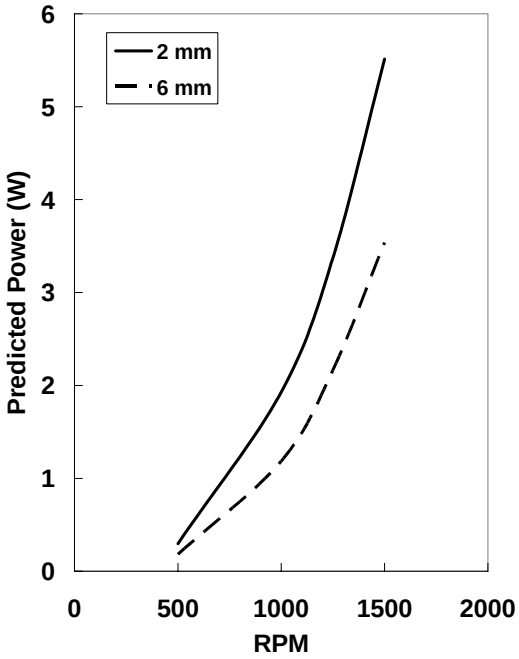

Figure 8.3: Model predictions of the power dissipated into the gap between a smooth rotating cylinder and stationary housing in Taylor vortex flow.

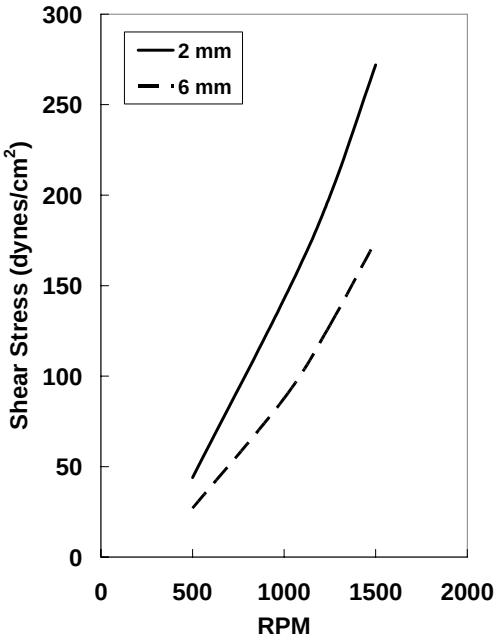

Figure 8.4: Model predictions of the shear stress in the gap between a smooth rotating cylinder and stationary housing in Taylor vortex flow.

8.2 METHODS

We tested the theoretical model using the Generation III device in water. The PRAL was placed in the pumping loop described in Chapter 3. A voltmeter was connected in parallel with the motor to measure the voltage input to the motor, and an ammeter was connected in series with the motor to measure the current input to the motor. The power input to the motor was determined by multiplying the voltage and current. Based on the efficiency of the motor obtained from the manufacturer specifications, the power delivered to the shaft was determined. We also measured the power dissipation for the smooth solid cylinder. The seals were removed during the assembly of the device to eliminate the power required to overcome the friction in the seals. After the device was assembled, the power consumed by the bearings was characterized by rotating the device in air and measuring the power input to the motor. Then, water was added to the device removing all air from the circuit. At each rotation rate, the power input to the motor was measured as well as the pressure and flow generated by the rotating fiber bundle. The power dissipated to the fluid through Taylor vortices was determined from the shaft power minus the pressure and flow work and minus the power consumed by the bearings.

8.3 RESULTS AND DISCUSSION – OUTER GAP

The power dissipation versus rotation rate for the fiber bundle, solid cylinder, and theoretical prediction with the 2 mm gap is shown in Figure 8.5. For the fiber bundle, the deviation between theory and experiment increased with rotation rate. At 500 RPM, we

calculated a theoretical dissipation of 0.3 W and measured a dissipation of 0.2 W. At 1500 RPM, we calculated a theoretical dissipation of 5.5 W and measured a dissipation of 15 W. The solid cylinder power dissipation trended with the theoretical prediction. The measured dissipation for the solid cylinder was 4.9 W at 1500 RPM (Figure 8.5).

We calculated the shear stress in the outer gap based on the power dissipation measurements (Figure 8.6). The theoretical shear stress at 1500 RPM was 272 dynes/cm^2 compared to 728 dynes/cm^2 for the fiber bundle and 243 dynes/cm^2 for the solid cylinder.

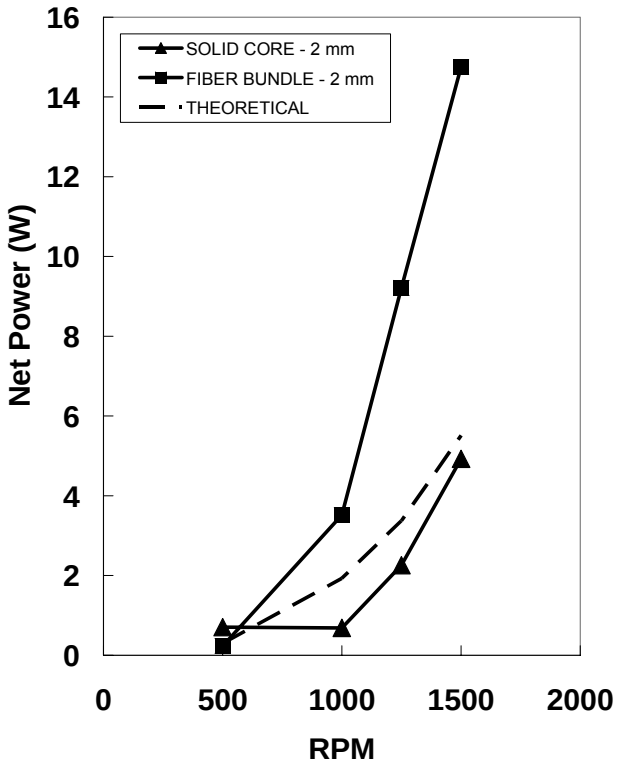

Figure 8.5: Net power dissipated for a 2 mm outer gap versus rotation rate.

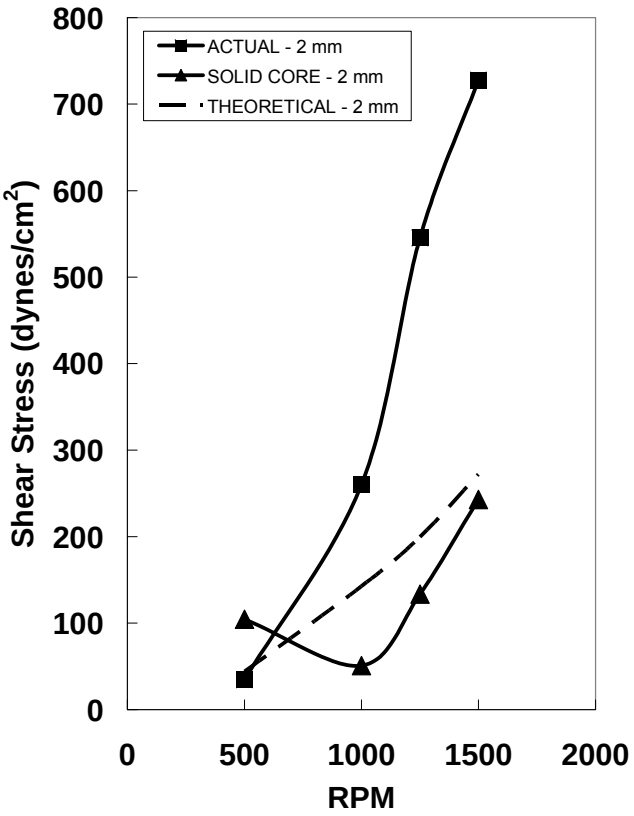

Figure 8.6: Shear stress for a 2 mm outer gap versus rotation rate.

For the bundle with the 6 mm gap, the theoretical and measured power dissipation into the water is shown in Figure 8.7. At 1500 RPM, the theoretical power dissipation was 3.5 W compared to a measured value of 10.8 W. The shear stress based on the theoretical and measured power was 175 dynes/cm^2 and 530 dynes/cm^2, respectively (Figure 8.8).

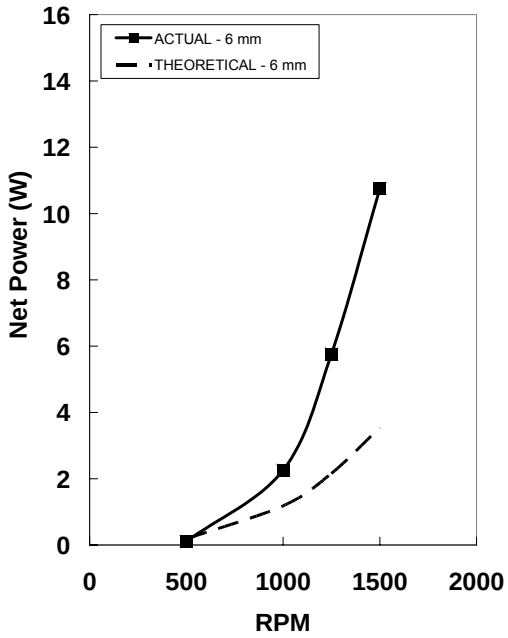

Figure 8.7: Net power dissipated for a 6 mm outer gap versus rotation rate.

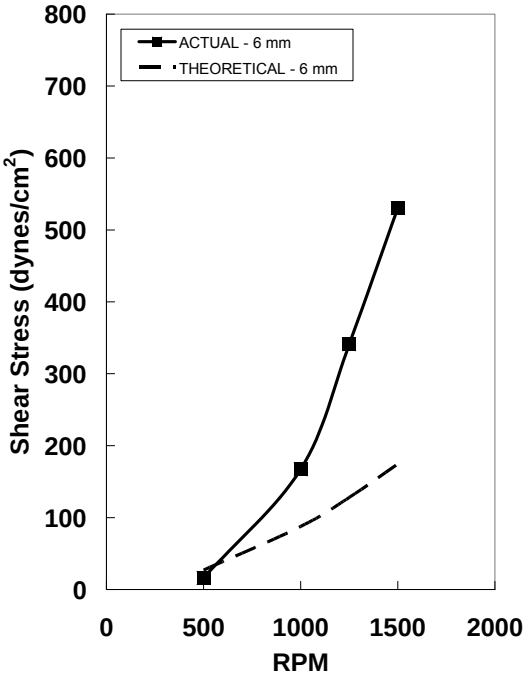

Figure 8.8: Shear stress for a 6 mm outer gap versus rotation rate.

Van den Berg et al investigated the effect of cylinder roughness on power dissipation by placing 0.3 cm strips in a longitudinal orientation circumferentially around the rotating cylinder. They developed a correlation for power dissipation versus rotation rate and found the roughness of the rotating cylinder increased the Reynolds number dependence from 1.5 to 1.88 [122]. We compared the correlation for rough cylinders to the bundle with the 6 mm gap because the gap ratio R_i/R_o was within 10% of the Van den Berg device.

The effect of roughness on power dissipation is shown in Figure 8.9 with the measured power from the 6 mm gap device and the prediction using the smooth cylinder correlation and the rough correlation. The power dissipation of the 6 mm device lies between the smooth and rough cylinder correlation. The fibers have a diameter of 0.03 cm compared to the 0.3 cm strips used by van den Berg, so we expect that since our roughness was less than that of van den Berg, our device would lie somewhere between the smooth and rough cylinder predictions.

The increased shear stress in the fiber bundle compared to the solid core is consistent with the hemolysis results in Chapter 7. The roughness of the fiber bundle generates high shear stress and therefore higher hemolysis in the gap between the rotating bundle and stationary housing.

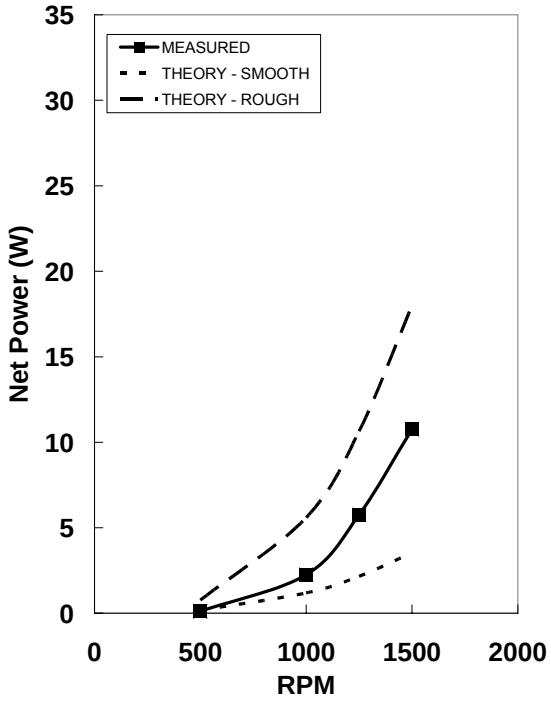

Figure 8.9: Effect of roughness on net power dissipated to the fluid.

From the power measurements, we calculated the shear stress, boundary layer thickness, and exposure time. Based on a measured power dissipation of 15 W at 1500 RPM, the shear stress exerted on a fluid particle is 740 dynes/cm^2. The model prediction in water was 270 dynes/cm^2, under predicting the measurements by a factor of 2.7. The model prediction in blood was obtained by increasing the viscosity by a factor of 3 resulting in a shear stress of 368 dynes/cm^2 at 1500 RPM. We multiplied the shear stress prediction in blood by 2.7 resulting in a shear stress of 994 dynes/cm^2. A more accurate prediction of the shear stress in blood could be obtained by repeating these tests in a glycerol-water solution with a viscosity matching that of blood. However, our measurements in water were adequate for the purpose of determining the effect of roughness on shear stress.

The exposure time of blood elements to this shear stress was calculated by dividing the volume of blood in the two boundary layers by the blood flowrate through the device. The boundary layer thickness was calculated using Equation 8.3 to be 0.02 cm. For the PRAL at 0.75 L/min, the resulting exposure time was 1.1 s. For the exposure time of 1.1 s in the PRAL, the threshold shear stress is 1500 dynes/cm^2. We calculated that the maximum shear stress in the PRAL was 994 dynes/cm^2 or 50% below the threshold reported in the literature. However, the thresholds reported in the literature are for complete red cell destruction. The bovine blood in our experiments had a hematocrit of 30-35% resulting in a total hemoglobin concentration of 12000 mg/dL. With a maximum PfHb concentration reaching 380 mg/dL after 6 hours, the shear stress in the PRAL is well below that which causes complete red cell destruction.

These measurements of shear stress were used in the blood damage model to predict hemolysis in a single pass through the PRAL:

$$\frac{\Delta PfHb}{Hb} = 3.62 \times 10^{-7} \left(99.4\right)^{2.416} \left(1.1\right)^{0.785} = 0.026 \qquad \textbf{(8.5)}$$

Over a 6 hour period, blood flowing at 0.75 L/min would make 180 passes through the device yielding $\frac{\Delta PfHb}{Hb} = 4.7$ per pass. If the total hemoglobin concentration was assumed to be 12000 mg/dL, the model predicts that complete red cell destruction should have occurred before the end of the 6 hour test. The over prediction by the model may be attributed to the application of the model to an average shear stress in the gap. The model was developed for predicting blood damage along a known fluid pathline. We attempted to use the average shear stress and exposure time of a fluid

particle in the outer gap. This simplification may not be valid. Future work using this model should employ CFD to calculate the shear stress along the pathline of a fluid particle in the outer gap to more accurately predict blood damage.

8.4 INTRODUCTION – INNER GAP

In Chapter 6, we also evaluated the hemolysis of the PRAL with and without the stationary center diffuser to test the effect of the shear stress in the inner gap. The PfHb increase was the same with or without the core so we concluded that the shear in the inner gap was not the main source of hemolysis in the PRAL. This chapter describes measurements of power dissipation in the inner gap. From these power measurements, we calculated the shear stress in the inner gap using a model found in the literature.

The region between the stationary inner core and the rotating bundle is similar to the classic case of a stationary inner cylinder surrounded by a rotating outer cylinder [80]. The radial pressure gradient generated by rotation is balanced by centrifugal forces creating a more stable flow than the case of a rotating inner cylinder surrounded by a stationary outer cylinder. However, above a critical Reynolds number, shown in Figure 8.10, the flow becomes turbulent. In the PRAL, the Reynolds number at 1500 RPM is above the threshold for turbulent flow. We analyzed the shear stress in this gap using an empirical relationship from the literature.

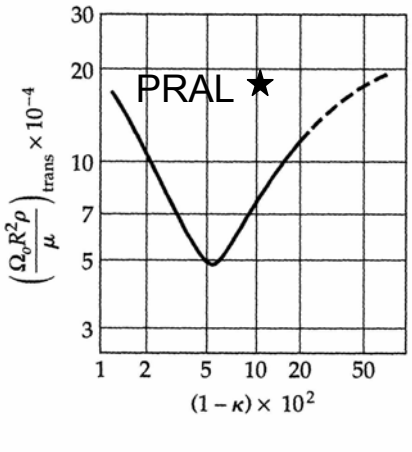

Figure 8.10: The PRAL is above the threshold for turbulence in the inner gap.

Koeltzsch et al developed a relationship for calculating the shear stress in turbulent flow between a stationary inner cylinder and rotating outer cylinder [134]. The device used in the Koeltzsch study was larger than the PRAL (R_o = 5.7 cm compared to R_o = 3.3 cm in the PRAL), but the ratio of the outer to inner diameter was the same, R_o/R_i = 1.14. The correlation is a function of the friction coefficient C_f, the Reynolds number, and the ratio of the outer and inner radii:

$$\frac{R_{out}}{R_{in}}\frac{1}{\sqrt{C_f}} = 8.14\log\left(\mathrm{Re}_{out}\sqrt{C_f} + 260.53\left(\frac{R_{out}}{R_{in}} - 1\right)\right) \qquad \textbf{(8.6)}$$

where the Reynolds number is defined as $\mathrm{Re} = \frac{(R_{out} - R_{in})R_m\omega_{out}}{\upsilon}$. We solved for the friction coefficient using GOALSEEK in Microsoft Excel and found the shear stress through the relationship:

$$\tau = \frac{1}{2}C_f \rho U_{out}^2 \qquad \textbf{(8.7)}$$

The theoretical power dissipation in the gap between the rotating fiber bundle and the stationary diffuser is shown in Figure 8.11. The power increased with rotation rate up to 3.8 W. The theoretical shear stress in the inner gap as a function of rotation rate is shown in Figure 8.12. The shear stress increased to 273 dynes/cm^2.

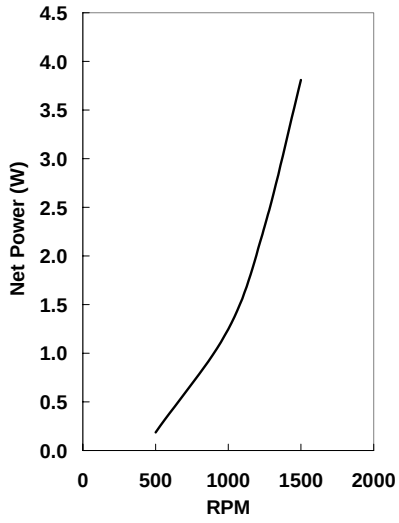

Figure 8.11. Theoretical power dissipation in the inner gap.

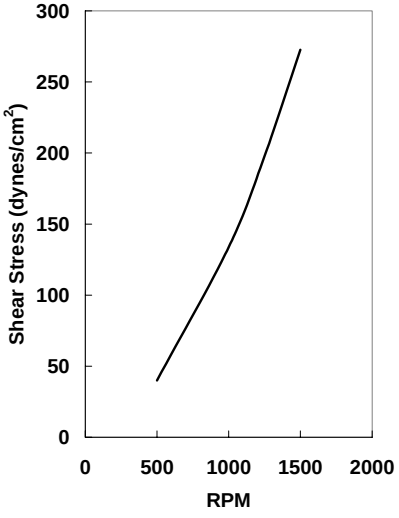

Figure 8.12: Theoretical shear stress in the inner gap.

We measured the power dissipation in the inner gap to better understand the hemolysis result from Chapter 7 that the inner gap is not a source of blood damage in the PRAL. We tested the inner gap shear stress model in water by measuring the power dissipation using the same setup used in the outer gap measurements and comparing the measurements to the model prediction. We evaluated the PRAL with and without the stationary center diffuser. The difference in power dissipation between these two tests was the power dissipated into the inner gap due to the turbulence in the inner gap.

8.5 RESULTS AND DISCUSSION – INNER GAP

The inner gap shear stress model predicted that 3.7 W will be dissipated into the inner gap at 1500 RPM. The shear stress based on this power dissipation would be 380 dynes/cm^2. The power measurements of the PRAL with and without the center diffuser are shown in Figure 8.13. The difference between these measurements, or the net power dissipated into the inner gap is shown in Figure 8.14. At 1500 RPM the net power measured for the device with the core was 15 W, and the net power for the device without the core was 13 W leaving power dissipation into the inner gap of 2 W. The calculated shear stress based on the measured power dissipation was 143 dynes/cm^2.

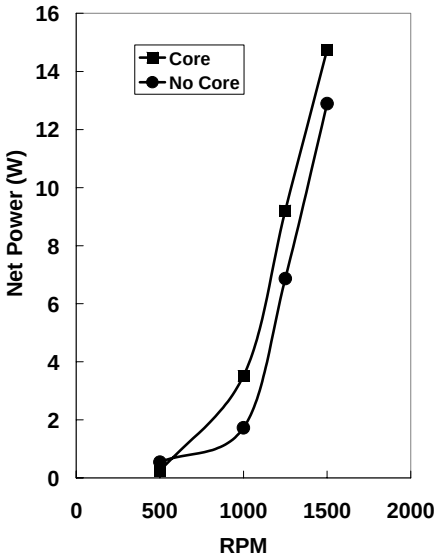

Figure 8.13: Net power dissipated for the PRAL with and without the diffuser.

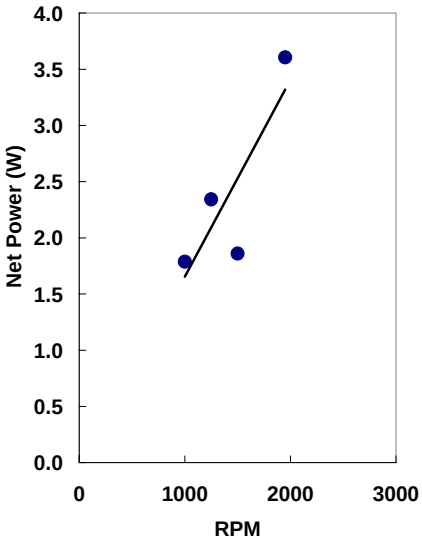

Figure 8.14: Net power dissipated due to the turbulence in the inner gap.

Our measurements of shear stress were more than 2 times lower than the model prediction. We attribute the difference to the radial flow present in the PRAL that was not present in the device used by Koeltzsch. We speculate that the radial flow generated by the rotating bundle may have prevented full turbulence from forming in the

inner gap resulting in lower shear stress. The shear stress of 143 dynes/cm^2 may still contribute to hemolysis in the PRAL, but this shear is still substantially lower than that in the outer gap and therefore is not the main source of hemolysis in the PRAL.

8.6 SUMMARY

In the hemolysis tests in Chapter 7, a smooth rotating cylinder produced less blood damage than the rotating fiber bundle. We hypothesized that the roughness of the fiber bundle was producing higher shear stress than the smooth cylinder. We evaluated this hypothesis by measuring the power dissipation into the fluid for both the smooth cylinder and the rotating fiber bundle and compared the results to theoretical predictions. We also measured the power dissipation for the fiber bundle with a larger gap between the rotating bundle and stationary housing. Based on the power measurements, we calculated the shear stress in the gap.

Our power measurements were consistent with the hypothesis that the roughness of the fiber bundle causes increased shear stress in the outer gap. The power dissipation of the fiber bundle at 1500 RPM was higher than the solid core by a factor of 3 (15 W versus 4.9 W). We believe the roughness of the fiber bundle to be the main cause of hemolysis in the PRAL.

9.0 MODELING CO_2 REMOVAL IN A BLOOD OXYGENATOR

9.1 INTRODUCTION

Blood oxygenators are routinely used in coronary artery bypass (CABG) surgery to maintain physiologic O_2 and CO_2 levels in the blood. Additionally, blood oxygenators have been used to reduce ventilator settings by temporarily assisting the native lungs allowing the lungs time to heal. A blood oxygenator is comprised of thousands of microporous hollow fiber membranes manifolded into a bundle structure. Sweep gas, usually pure oxygen or air, flows through the lumens of the fibers while blood flows on the outside of the fibers. O_2 diffuses out of the fiber and into the blood while CO_2 diffuses out of the blood into the fiber. The gas exchange efficiency of the device is dictated by the concentration gradient of O_2 and CO_2 between the blood and the sweep gas and by the size of the boundary layer that forms on the blood side of the fibers [135-137].

One approach to designing an efficient blood oxygenator is through trial and error by building and testing prototypes. The trial and error process can be expensive, labor-intensive, and may take many years before producing a more efficient oxygenator. More recently, computational fluid dynamics (CFD) models have been developed in an attempt to reduce the number of iterations between experiments and final prototypes. The fiber bundle is modeled as a porous medium since modeling the individual fibers in

a bundle is computationally impractical [138-140]. Using CFD, Gage et al was able to predict pressure drop versus flowrate through the fiber bundle by determining the fiber bundle permeability a priori [139]. Others have used CFD to find regions of flow stasis within the oxygenator and predict localized areas of thrombus deposition [140-142]. The use of CFD to optimize an oxygenator requires expensive software packages and computer hardware, and requires a priori knowledge of the performance of the oxygenator to accurately predict gas exchange.

Mockros and Leonard [136] developed a semi-empirical model to predict oxygen exchange rates in blood based on gas exchange results obtained in water. The model assumed one-dimensional flow through the fiber bundle and utilized a mass transfer correlation based on a heat transfer analogy found in the literature [143]. The correlation contained two empirical constants that were determined experimentally in water. The correlation was used to predict gas exchange in blood by incorporating an 'effective diffusivity' to account for the binding of oxygen to hemoglobin not present in water. The advantage of the model was that the oxygenator could be designed using water as the test fluid without the complexity and expense of using blood. The model has been validated at various flowrates, inlet oxygen saturations, and blood temperatures [81, 82].

The purpose of this study was to develop a mathematical model to predict carbon dioxide removal rates in hollow fiber membrane oxygenators analogous to the Mockros model for oxygen exchange. Carbon dioxide is present as bicarbonate in the plasma and red blood cells (90%), bound to hemoglobin (5%), and dissolved (5%) [144]. Dissolved CO_2 can rapidly be converted to bicarbonate (HCO3) and vice versa in the presence of the enzyme carbonic anhydrase in the red cells. The rapid rate of reaction

between CO_2 and HCO3 enabled the assumption of equilibrium between all forms of CO_2 in the model proposed in this paper. The assumption of equilibrium for all forms of CO_2 in the blood is analogous to the assumption of equilibrium between oxygen and hemoglobin in the O_2 model [32, 76, 136].

The model was developed to predict both O_2 and CO_2 transfer rates in two fiber bundle modules of different lengths and thicknesses. The modules were manufactured and the first module was tested in water to obtain the empirical coefficients for the mass transfer correlation. The correlation was used to predict gas exchange in blood for both modules. The modules were then tested in blood, and the gas exchange results were compared to the model predictions.

9.1.1 Transport Equations – Oxygen

The derivation of the mass transfer equations for O_2 exchange in blood by a membrane oxygenator have been described by Mockros and others [19, 32, 76, 81, 82, 136], and will be summarized here. The model assumed that the gas side and membrane mass transfer resistances are negligible [135]. Dissolved O_2 is assumed to be in equilibrium with O_2 bound to hemoglobin at all locations within the oxygenator because the reaction rate of O_2 binding to hemoglobin is much higher than the rates of diffusion and convection of O_2 [145]. The change in O_2 concentration in the blood as it flows through the fiber bundle can be determined from an overall mass balance on O_2:

$$Q\frac{dC_{O2}}{dr} = 2\pi rLk_{O2\_b}a_v(P_{g\_02} - P_{O2}) \qquad \textbf{(9.1)}$$

In this equation, Q is the flowrate of blood through the fiber bundle, C_{O2} is the concentration of O_2 in the blood (dissolved O_2 and bound to hemoglobin), r is the radial coordinate, L is the bundle thickness, a_v is the surface area per volume of the fiber bundle, k_{O2} is the mass transfer coefficient for oxygen, (P_{g_O2}-P_{O2}) is the difference in partial pressure between the gas within the lumens of the fibers and the blood. The gas partial pressure in the fiber, P_{g_O2}, is assumed to be constant along the length of the fibers. The left hand side of Equation 1 represents the convection of dissolved gas into and out of the bundle, and the right hand side represents the amount of O_2 transported into the blood by the fibers. In the overall mass balance, molecular diffusion of O_2 is small relative to convection of O_2 and is therefore neglected as a means of entering and exiting the bundle.

The concentration of O_2 is expressed as a combination of the dissolved component and the O_2 bound to hemoglobin: $C_{O2} = \alpha_{O2} P_{O2} + C_T S_{O2}$ where α_{O2} is the solubility of oxygen in blood, C_T is the maximum capacity of bound O_2 in blood assuming 100% hemoglobin saturation (S_{O2}) [76]. This model can be used to predict gas exchange in water by setting C_T to zero since only dissolved O_2 is present and using the solubility of O_2 in water, α_{O2_w}. The differential equation governing O_2 transfer in blood becomes:

$$\frac{dP_{O2}}{dr} = \frac{2\pi k_{O2\_b} a_v r L}{\alpha_{O2} Q (1 + \frac{C_T}{\alpha_{O2}} \lambda_{O2})} (P_{g\_O2} - P_{O2}) \qquad \textbf{(9.2)}$$

where $\lambda_{O2} = \frac{dS_{O2}}{dP_{O2}}$ is the slope of the oxyhemoglobin dissociation curve. The mass transfer coefficient (k_{O2}) is determined from an analogous heat transfer correlation for

flow perpendicular to a bundle of tubes [81, 82, 136]. This empirical correlation has the form [81]:

$$Sh = a\,\mathrm{Re}^{b}\,Sc^{1/3} \qquad \textbf{(9.3)}$$

where Sh is the Sherwood number, Re is the Reynolds number, and Sc is the Schmidt number. The coefficients a,b depend on the fiber bundle geometry and are determined experimentally in water. The Sherwood number is defined as: $Sh = \frac{k_{O2\_w} d_h}{\alpha_{O2\_w} D_{O2\_w}}$ where k_{O2_w} is the mass transfer coefficient for oxygen in water, and D_{O2_w} is the diffusivity of the dissolved O_2. The Reynolds number is defined as $\mathrm{Re} = \frac{\rho V d_h}{\mu}$ where d_h is the hydraulic diameter characteristic of the fiber bed packing [146], ρ is the fluid density and μ is the fluid viscosity. Since the bundle is modeled as a porous medium, the superficial velocity (V) is used: $V = \frac{Q}{2\pi r L}$. In water, the Sc number is defined as: $Sc = \frac{\nu_w}{D_{O2\_w}}$ where ν_w is the kinematic viscosity of the water. In blood, the mass transfer correlation must account for the binding of O_2 by hemoglobin. This is accomplished by incorporating an effective diffusivity in the Schmidt number, but not in the Sherwood number [24, 76, 81]: $Sc = \frac{\nu_b}{D_{eff}}$ where ν_b is the kinematic viscosity of the blood, and D_{eff} is the effective diffusivity defined as:

$$D_{eff} = \frac{D_{O2}}{1 + \frac{C_T}{\alpha_{O2}} \lambda_{O2}} \qquad \textbf{(9.4)}$$

The mass transfer coefficient for blood becomes:

$$k_{O2\_b} = a\alpha_{O2}\left(\frac{Q}{2\pi rL}\right)^{b} d_h^{b-1} \nu^{1/3-b} D_{O2}^{2/3}\left(1+\frac{C_T}{\alpha_{O2}}\lambda_{O2}\right)^{1/3} \quad \textbf{(9.5)}$$

This expression is inserted into Equation 2 which can then be integrated to give the concentration profile of O_2 in blood within the fiber bundle. The concentration of O_2 exiting the bundle is then used to calculate the total gas transferred by the blood oxygenator:

$$\dot{V}_{O2} = Q_b\left(C_{O2}^{out} - C_{O2}^{in}\right) \quad \textbf{(9.6)}$$

The values used in the O_2 model are shown in Table 9-1.

Table 9-1: Physical Constants for O_2.

Parameter	Description	Value
α_{O2_w}	Solubility of O_2 in water	3.16E-5 ml O_2 ml^{-1} $mmHg^{-1}$
α_{O2}	Solubility of O_2 in blood	3.0E-5 ml O_2 ml^{-1} $mmHg^{-1}$
D_{O2}	Diffusivity of O_2 in water	2.8E-5 cm^2 s^{-1}
D_{O2}	Diffusivity of O_2 in blood	1.8E-5 cm^2 s^{-1}
S_{in}	Inlet Saturation	65 mmHg
C_T	Hemoglobin binding capacity	0.167 ml O_2/ml blood
P_{G_O2}	Average partial pressure of O_2 in sweep gas	700 mmHg

9.1.2 Transport Equations – Carbon Dioxide

The model for carbon dioxide removal in a membrane oxygenator must account for CO_2 in the form of bicarbonate ions, bound to hemoglobin, and dissolved. In the tissues, CO_2

diffuses down its concentration gradient into the plasma then enters the red cell [144, 147]. In the red cell, CO_2 is hydrated into carbonic acid in the presence of the enzyme carbonic anhydrase (Reaction 1 below). Carbonic acid is then dissociated into hydrogen ion and bicarbonate (Reaction 2):

$$CO_2 + H_2O \overset{\text{Carbonic Anhydrase}}{\overset{1}{\Leftrightarrow}} H_2CO_3 \overset{2}{\Leftrightarrow} H^+ + HCO_3^-$$

HCO3 exits the red cell and enters the plasma in exchange for chloride ion when the concentration of HCO3 builds up in the red cell. As blood flows through the oxygenator, dissolved CO_2 diffuses from the plasma across the fiber membrane and is removed by the sweep gas. As CO_2 is removed from the plasma by the oxygenator, bicarbonate diffuses into the red cell where it is converted to CO_2 through the reverse reactions above. The CO_2 diffuses back across the red cell membrane into the plasma where it is removed by the oxygenator. The presence of carbonic anhydrase increases the rate of conversion between CO_2 and HCO3 so that equilibrium can be assumed between all forms of CO_2 in the blood (see discussion) [148, 149]. This analysis for CO_2 removal in the membrane lung assumes that carbonic anhydrase in the red blood cells is available in sufficient quantity to catalyze the CO_2/HCO_3 reaction throughout the CO_2 transport process. In the overall mass balance for CO_2, the concentration of total CO_2 (ml CO_2/ml blood) can be expressed in terms of partial pressure through the relationship [31]: $C_{CO2} = qP_{CO2}^t$ which is an empirical fit of the CO_2 dissociation curve. The constants *q* and *t* are fit parameters with values of 0.128 and 0.369, respectively. The mass balance on CO_2 can be expressed by the following equation.

$$Q(qtP_{CO2}^{t-1})\frac{dP_{CO2}}{dr} = -2\pi r k_{CO2} a_v L(P_{CO2} - P_{G\_CO2}) \quad \textbf{(9.7)}$$

The mass transfer correlation takes the same form for CO_2 as O_2 (Equation 9.3), but the Sh and Sc numbers must be defined appropriately to account for all forms of CO_2 present in the blood. For O_2, oxyhemoglobin is transported by convection only, since the hemoglobin molecule resides in the red blood cell resulting in negligible diffusion of oxyhemoglobin. The diffusivity in the Sh number for O_2 accounts for the diffusion of dissolved O_2 (Equation 9.4). For CO_2, the diffusivity in the Sherwood number must account for the diffusion of bicarbonate in addition to the diffusion of dissolved CO_2 (see Boundary Conditions in Appendix). This leads to a facilitated diffusivity in the Sh number that is not present in the O_2 model:

$$D_f = D_{CO2} + \frac{D_{HCO3}}{\alpha_{CO2}}\frac{\partial C_{HCO3}}{\partial P_{CO2}} \quad \textbf{(9.8)}$$

The term $\frac{\partial C_{HCO3}}{\partial P_{CO2}}$ is the change in bicarbonate ion concentration with respect to the change in pCO2. The large amount of HCO_3 relative to the total CO_2 (90%) enables $\frac{\partial C_{HCO3}}{\partial P_{CO2}}$ to be approximated as the slope of the CO_2 dissociation curve [31]:

$$\frac{\partial C_{HCO3}}{\partial P_{CO2}} \cong \frac{\partial C_{CO2}}{\partial P_{CO2}} \cong qtP_{CO2}^{t-1} \equiv H \quad \textbf{(9.9)}$$

Therefore, the facilitated diffusivity becomes:

$$D_f = D_{CO2} + \frac{D_{HCO3}}{\alpha_{CO2}}H \quad \textbf{(9.10)}$$

In this equation H is the slope of CO_2 dissociation curve. In the Schmidt number, the diffusivity must account for the convection of CO_2 carried as bicarbonate and bound to hemoglobin and therefore becomes an 'effective diffusivity' similar to that defined by Vaslef for O_2 [81]:

$$D_{eff} = \frac{D_f}{1 + \frac{1}{\alpha_{CO2}} \lambda_{CO2}} \qquad \textbf{(9.11)}$$

where $\lambda_{CO2} = \frac{\partial C^b_{CO2}}{\partial P_{CO2}}$ is the change in concentration of the chemically bound CO_2 (as bicarbonate and bound to hemoglobin). The change in bound CO_2 can be approximated with the slope of the CO_2 dissociation curve (H) because of the large amount of CO_2 present as bicarbonate and bound to hemoglobin (95%). Once the relationships for facilitated diffusion and effective diffusivity are inserted into the mass transfer correlation, the mass transfer coefficient in blood becomes for CO_2:

$$k_{CO2\_b} = a\alpha_{CO2}\left(D_{CO2} + \frac{D_{HCO3}}{\alpha_{CO2}} H\right)^{2/3} d_h^{(b-1)} \left(\frac{Q}{2\pi r L}\right)^b \upsilon^{(1/3-b)} \left(1 + \frac{1}{\alpha_{CO2}} H\right)^{1/3} \qquad \textbf{(9.12)}$$

This expression can be inserted into Equation 9.7 which can then be integrated to give the concentration profile of CO_2 in blood within the fiber bundle. Once the concentration profile is known, the total CO_2 removal of the blood oxygenator can be determined:

$$\dot{V}_{CO2} = Q_b \left(C^{in}_{CO2} - C^{out}_{CO2}\right) \qquad \textbf{(9.13)}$$

The parameters used in the CO_2 model are shown in Table 9-2.

Table 9-2: Physical Constants for CO_2.

Parameter	Description	Value
α_{CO2_w}	Solubility of CO_2 in water	7.5E-4 ml CO_2 ml^{-1} $mmHg^{-1}$
α_{CO2}	Solubility of CO_2 in blood	6.62E-4 ml CO_2 ml^{-1} $mmHg^{-1}$
D_{CO2_w}	Diffusivity of CO_2 in water	1.92E-5 cm^2 s^{-1}
D_{CO2}	Diffusivity of CO_2 in blood	7.39E-6 cm^2 s^{-1}
D_{HCO3}	Diffusivity of HCO_3 in blood	4.62E-6 cm^2 s^{-1}
P_{in}	Inlet pCO_2	45 mmHg
P_{G_CO2}	Average partial pressure of CO_2 in sweep gas	4 mmHg
ν_w	Kinematic viscosity of water	6.63E-3 cm^2 s^{-1}
ν_b	Kinematic viscosity of blood	0.023 cm^2 s^{-1}
Q	Blood Flowrate	0.5-2.75 L min^{-1}

9.2 METHODS

An oxygenator module was fabricated to compare the model predictions to experimental measurements of gas exchange. The coefficients (a,b) in the mass transfer correlation were determined through gas exchange rates measured in water. The coefficients were used to determine the mass transfer coefficient for O_2 and CO_2. The solution to Equation 9.2 and Equation 9.77 was determined numerically using the built-in ordinary differential equation solver in Matlab based on the Runga-Kutta method [150]. The inlet partial pressure of O_2 and CO_2 were specified as 40 mmHg and 50 mmHg, respectively. The concentration of O_2 was determined by the program and input into Equation 9.6 to calculate oxygen exchange. The concentration of CO_2 exiting the bundle was also determined by the program and input into Equation 9.13 to calculate CO_2 removal. The gas exchange was then measured in vitro using blood and compared to the model. A

second module was manufactured with a shorter, thicker bundle but the same overall surface area as the first module.

9.2.1 Prototype Description

An oxygenator module was fabricated with a gas exchange surface area of 0.42 m^2 (Figure 9.1). The fiber bundle was composed of uncoated microporous polypropylene fibers weaved into a mat. The fibers had an outer diameter of 300 μm and an inner diameter of 240 μm (Celgard, ARX30240, Charlotte NC). The fibers were wrapped and potted to a cylindrical support structure. The center diffuser was fabricated from clear acrylic, and four 10 mm holes were machined in the upstream end of the diffuser for fluid to be distributed into the fiber bundle. The housing that surrounded the fiber bundle was made from a stock piece of clear acrylic with two threaded endcaps that prevented the module from leaking. The blood inlet was located in the center of the upstream endcap and was screwed to the center core for blood to enter the fiber bundle. The blood outlet was located at the distal end of the acrylic housing. Gas entered and exited the fiber lumens through side ports in the endcaps. A schematic of the module is shown in Figure 9.1.

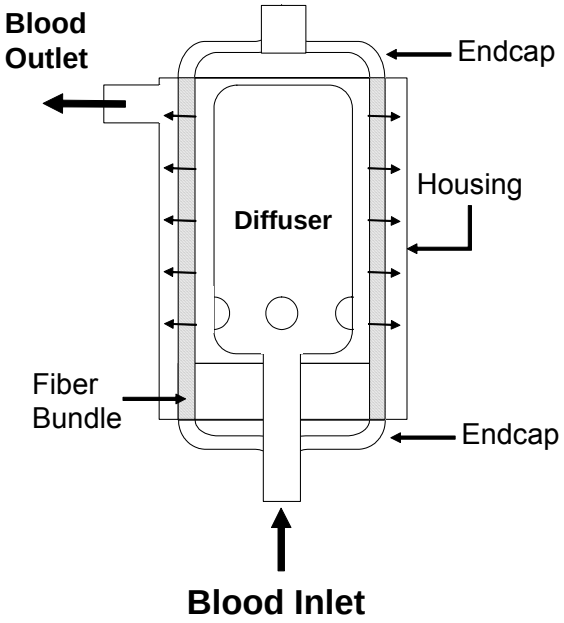

Figure 9.1 – Schematic of oxygenator module.

The gas pathway was separated from the liquid pathway by 3/8" ID nitrile seals (P/N 6119, Chicago Rawhide, Chicago, IL). A second module was fabricated having a shorter, thicker fiber bundle using the same procedures and materials as the first module. The geometrical differences between the long bundle (first module) and the short bundle (second module) are summarized in Table 9-3.

Table 9-3. Characteristics of Prototype Fiber Bundle Modules.

	First Module	Second Module
Length (cm)	13	4
Fiber Diameter (cm)	0.03	0.03
Outer Diameter (cm)	7	6.6
Inner Diameter (cm)	6.6	4.6
Bundle Thickness (cm)	0.2	1
Surface Area (m^2)	0.42	0.42
Porosity	0.43	0.53
Number of Fibers	3428	11141

9.2.2 In vitro gas exchange

A flow loop was constructed for testing in water or blood that consisted of a reservoir: a 12 L bucket for water, or a blood transfusion bag (Affinity Venous Reservoir Bag, Medtronic MN for blood tests), a centrifugal pump (March Manufacturing, Glenview, IL for water; Biomedicus BP-80X, Medtronic, Minneapolis, MN for blood), a commercial oxygenator (Affinity, Medtronic, Minneapolis, MN), and the module prototype (Figure 9.2).

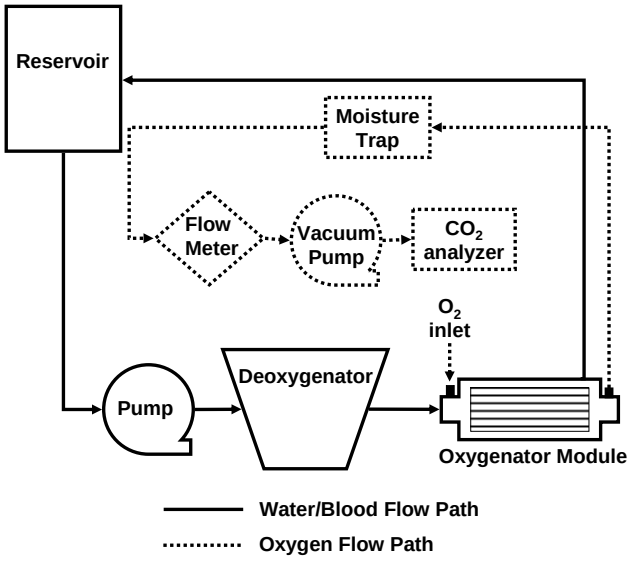

Figure 9.2 – Gas exchange characterization loop for water and blood.

Tubing connected the outflow port of the reservoir to the inlet of the centrifugal pump. The pump was used in conjunction with a Hoffman clamp to set the flowrate. Sweep gas through the commercial oxygenator was a N_2/CO_2 mix adjusted with a gas blender (Cole-Parmer Instrument Company, Vernon Hills, IL) to set the inlet conditions in accordance with the Association for the Advancement of Medical Devices (AAMI) standards [75]: O_2 inlet saturation 65 +/- 5% and inlet pCO_2 of 45 +/- 5 mmHg. The test

fluid, either water or blood flowed from the centrifugal pump to the commercial oxygenator into the module and then back to the reservoir. The flowrate was measured using a flow probe (Transonic Systems, Inc, Ithaca, NY) that was calibrated for both water and blood. O_2 partial pressures at the inlet and outlet of the device were measured using a blood-gas analyzer (ABL-505 Radiometer Copenhagen, Denmark). The concentration and saturation of hemoglobin was measured with an OSM3 Hemoximeter (Radiometer). Pure oxygen sweep gas flowed under vacuum through the module fiber lumens at 6.5 L/min in water and 8.5 L/min in blood. The gas then flowed through a moisture trap consisting of a beaker immersed in ice and through a Top Trak flow meter (Sierra Instruments, Inc., Monterey, CA). A Barnant vacuum pump and needle valve were used to maintain constant sweep gas flow through the module. A CO_2 analyzer (Physiodyne, Quogue, NY) was used to measure the concentration of CO_2 exiting the gas stream of the module. The blood was collected from a local slaughterhouse and filtered with 40 μm pore size filters (Pall Biomedical, Inc., Fajardo, PR) on the day of collection to remove any hair or extraneous particles due to the collection process, and Gentamycin (0.1 g/mL) was added to prevent infection. The flowrate through the module in water was varied between 1.0 - 5.5 L/min, and in blood the flowrate through the long bundle module was 0.75, 1.5, 2.2 L/min. In the short bundle module, the blood flowrate was 0.75 L/min. The flowrates were chosen in random order and each gas exchange measurement was repeated at least twice.

Oxygen transfer rates in blood (V_{O2}) were calculated using the following relationship [20]:

$$\dot{V}_{O2} = Q\left[\alpha_{O2}(P_{O2}^{out} - P_{O2}^{in}) + C_T \Delta S\right] \quad \textbf{(9.14)}$$

In equation 9.14, Q is the blood flow rate, α_{O2} is the solubility of O_2 (3.16E-4 ml O_2/ml blood/cmHg), and $(P_{O2}^{out} - P_{O2}^{in})$ is the difference in partial pressure between the inlet and outlet of the device. C_T is the hemoglobin binding capacity of blood (0.167 ml O_2/ml blood), and ΔS is the change in saturation of the hemoglobin from the inlet to the outlet. O_2 transfer in water was calculated by setting ΔS equal to zero in Equation 8.14 and using a solubility of 3.16E-5 ml O_2/ml H_2O/mmHg [76]. Carbon dioxide removal rate (V_{CO2}) was calculated from the sweep gas flowrate (Q_{OUT}^{STP}) and CO_2 fraction (F_{CO2}) exiting the module:

$$\dot{V}_{CO2} = Q_{OUT}^{STP} F_{CO2} \qquad \textbf{(9.15)}$$

Variations in the inlet pCO2 can affect the overall gas exchange of the device. For example, an inlet pCO2 of 45 mmHg will have a lower CO_2 removal rate than a pCO2 of 50 mmHg because this 5 mmHg difference in inlet conditions corresponds to a 10% difference in concentration gradient across the fiber membranes. Therefore, the CO_2 exchange (V_{CO2}^{*}) was normalized to an inlet pCO2 of 50 mmHg to reduce the variability associated with fluctuating inlets [20, 63]:

$$\dot{V}_{CO2}^{*} = \dot{V}_{CO2} \frac{50}{pCO_2^{INLET}} \qquad \textbf{(9.16)}$$

If the inlet value differed by more than 45 +/- 5 mmHg, the inlet concentration was adjusted by changing the sweep gas through the commercial oxygenator and the sample was taken again.

In water, the mass transfer coefficient was determined from the VCO_2 and VO_2 data:

$$k_{CO2\_w} = \frac{\dot{V}_{CO2}}{A\Delta P_{LM\_CO2}} \qquad k_{O2\_w} = \frac{\dot{V}_{O2}}{A\Delta P_{LM\_O2}} \qquad \textbf{(9.17)}$$

where A is the fiber bundle membrane area, ΔP_{LM} is the log mean partial pressure difference between the water flowing outside of the fibers and the gas flowing on the inside of the fibers. The concentration of gas inside the fibers was assumed constant. For CO_2 P_g was assumed to be 4 mmHg, and for O_2 P_g was assumed to be 700 mmHg.

The gas exchange data was used to develop the mass transfer correlation of the form: $Sh = a\,\mathrm{Re}^b\,Sc^{1/3}$ where *Sh* is the Sherwood number, *Re* is the Reynolds number, and *Sc* is the Schmidt number. The Sherwood correlation was plotted on a log-log scale and the model parameter values *a,b* were determined through a linear curve fit. The values for *a,b* were then input into Equation 9.5 and Equation 9.12 to determine the mass transfer coefficient for O_2 and CO_2 in blood, respectively. Once the mass transfer coefficient was determined, the concentration profile within the fiber bundle was calculated and used to predict gas exchange.

9.3 RESULTS

The gas exchange experiments in water were used to develop a mass transfer correlation to predict both O_2 and CO_2 exchange in blood at various flowrates. The gas exchange rates in water as a function of flowrate through the first module (long, thin bundle) are shown in Figure 9.3.

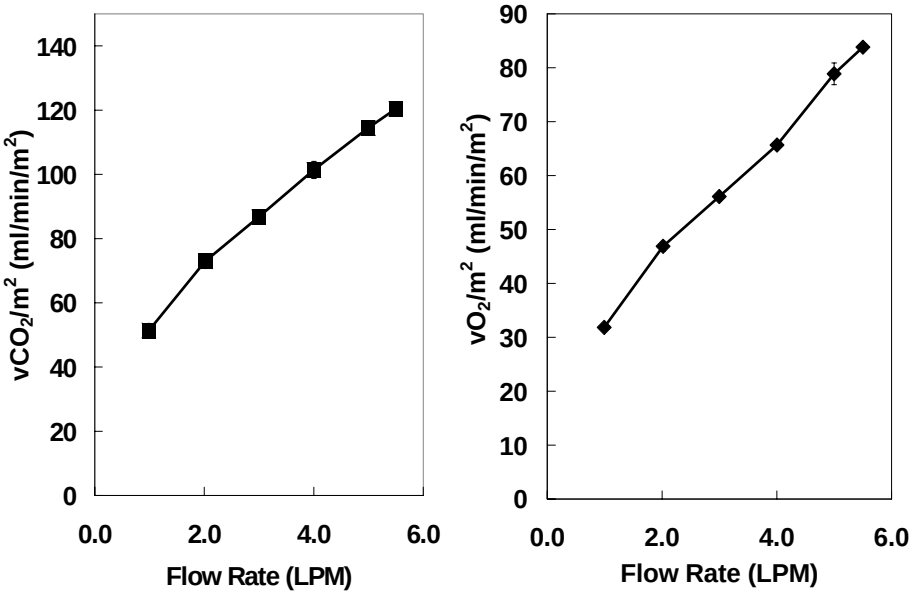

Figure 9.3 – Gas exchange rates versus flowrate for the first module (long, thin bundle) in water. Left: CO_2 removed. Right: O_2 supplied.

The CO_2 removal rates ranged from 51 +/- 0.2 ml/min/m^2 at 1 L/min to 120 +/- 1.6 ml/min/m^2 at 5.5 L/min. The O_2 supplied to the water ranged from 32 +/- 0.4 ml/min/m^2 at 1 L/min to 84 +/- 0.5 at 5.5 L/min. The dimensionless correlation developed from the water gas exchange experiments is plotted in Figure 9.4. The O_2 and CO_2 data collapsed onto a single curve, and a nonlinear regression was used to determine the value of the constant *a* to be 0.54 and the constant *b* to be 0.42.

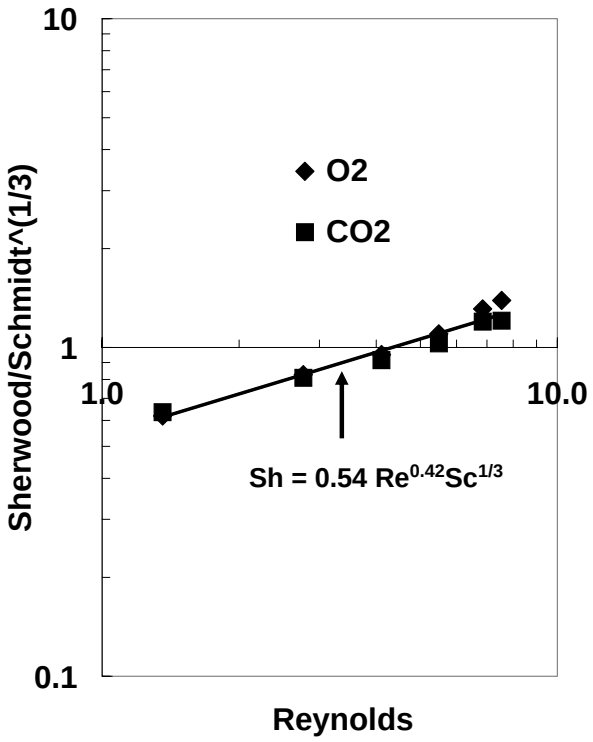

Figure 9.4 – Dimensionless mass transfer correlation for the first module.

Therefore, the mass transfer correlation used to calculate gas exchange in blood was:

$$Sh = 0.54\,\mathrm{Re}^{0.42}\,Sc^{1/3} \qquad \textbf{(9.18)}$$

Model predictions and experimental measurements of CO_2 removal for the first module in blood as a function of flowrate are shown in Figure 9.5. The model predicted CO_2 removal of 50 ml/min at a blood flowrate of 0.75 L/min compared to a measured value of 53 +/- 1 ml/min. The model predicted an increase in CO_2 removal with flowrate to 82 ml/min at 2.2 L/min compared to the measured value of 75 +/- 2 ml/min. The model predictions were within 6% of the measured value at 0.75 L/min and within 9% of the experimental measurements at 2.2 L/min. The model prediction of CO_2 removal without accounting for the facilitated diffusion is shown as a dashed line on Figure 9.5. In the

model prediction, the facilitated diffusivity was replaced by the diffusivity of dissolved CO_2. The model underpredicted CO_2 removal by over 65% when the facilitated diffusivity was not taken into account.

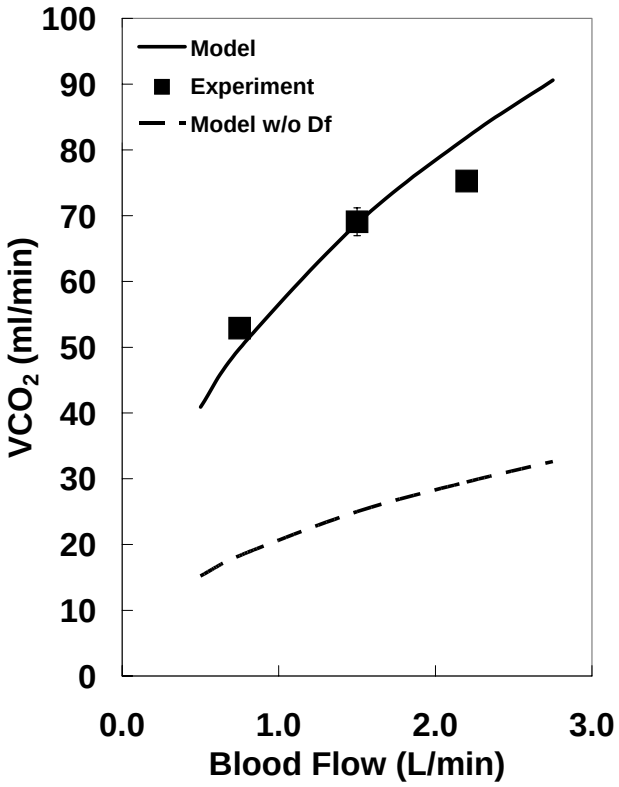

Figure 9.5 – Comparison of measured (symbols) and predicted (line) CO_2 removal in blood for the first module at various flowrates. The dashed line is the model without accounting for the diffusion of HCO3. The prediction is equivalent to using the O_2 model to predict CO_2 removal where the facilitated diffusion was replaced with the diffusivity for dissolved CO_2.

Model predictions and experimental measurements of O_2 exchange for the long module in blood are shown in Figure 9.6. The model predicted an O_2 exchange rate of 29 ml/min compared to a measured value of 29 +/- 1 ml/min at 0.75 L/min. The model predicted an O_2 exchange rate of 53 ml/min at 2.2 L/min compared to the measured value of 48 +/- 2 ml/min. For O_2, the model predictions were within 1% of the measured

value for O_2 at 0.75 L/min and within 10% of the experimental measurements at 2.2 L/min.

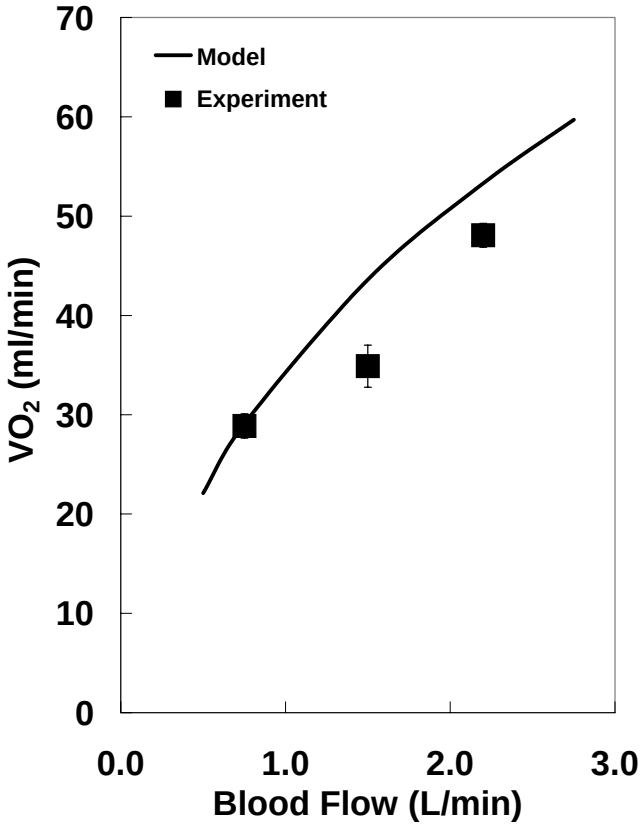

Figure 9.6 – Comparison of measured (symbols) and predicted (line) O_2 transfer in blood for the first module versus flowrate.

The mass transfer correlation determined for the first module was applied to the second module which was thicker than the first module (1 cm vs. 0.2 cm) and shorter (4 cm vs 13 cm). Gas exchange predictions and experimental measurements of CO_2 removal in the second module at 0.75 L/min are shown in Figure 9.7.

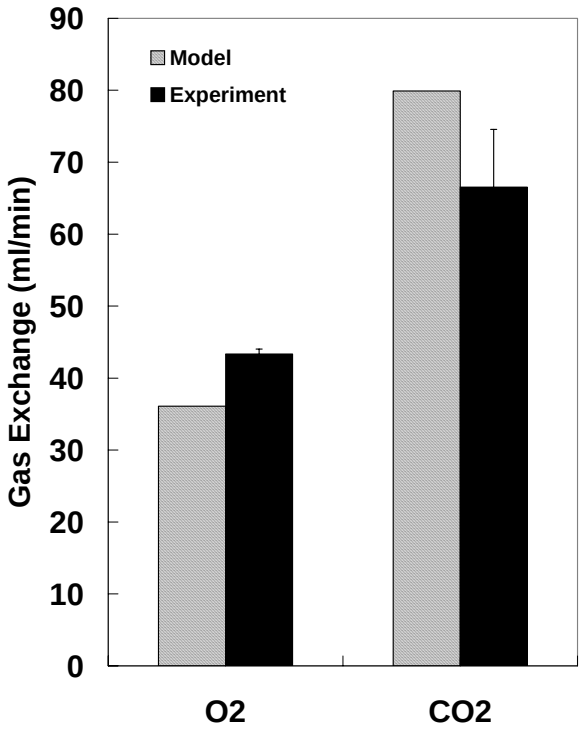

Figure 9.7 – Comparison of measured (filled bars) and predicted (dashed bars) CO_2 and O_2 transfer in the second module (short, thick bundle).

The model predicted a CO_2 removal of 80 ml/min compared to the measured value of 67 +/- 8 ml/min. For O_2, the model predicted an O_2 transfer rate of 36 ml/min compared to the measured value of 43 +/- 1 ml/min.

9.4 DISCUSSION

A mathematical model has been developed to predict CO_2 removal rates in blood from removal rates measured in water. The approach to modeling CO_2 removal rates was analogous to one developed by Mockros for predicting O_2 exchange rates. The dimensionless mass transfer correlation was shown to collapse onto one universal curve for both O_2 and CO_2 in water. The correlation was used to predict both O_2 and

CO_2 exchange in blood by incorporating an appropriate facilitated diffusivity for CO_2 to account for the diffusion of CO_2 stored as bicarbonate.

A simple analytical approach to analyzing convection-diffusion in hollow fiber membrane oxygenators does not presently exist, so mass transfer correlations are used to predict gas exchange. In this work, appropriate definitions for the Sherwood and Schmidt numbers were determined to account for the diffusion of CO_2 in the blood transported as HCO3. The facilitated diffusivity is present in the Sherwood number for CO_2 which arises from the boundary condition at the wall of the fiber (See Appendix – Equation A.11). This is in contrast to the definition of the Sherwood number for O_2 in that the diffusivity only accounts for the diffusion of dissolved oxygen. The O_2 that is transported from the fibers into the blood binds to hemoglobin but has a negligible diffusing capacity since hemoglobin is present inside the red blood cell. The importance of incorporating the facilitated diffusivity for CO_2 was shown by replacing the facilitated diffusivity in the model with the diffusion coefficient for dissolved CO_2 (dashed line, Figure 9.5). In essence, the model then becomes the O_2 model applied to directly to CO_2. Clearly, the effect of the facilitated diffusion of CO_2 is important since the gas exchange predictions are well below the experimental results.

The model assumed equilibrium between dissolved CO_2 and HCO3 formed from the hydration of CO_2. This assumption was justified by comparing the half-time of the hydration reaction to the diffusion time of CO_2 through the plasma to the fiber membrane wall. The presence of carbonic anhydrase in the red blood cell accelerates the hydration reaction 13000 times faster than in the plasma where the enzyme is not present [147, 151]. The half-time for equilibration of CO_2 with bicarbonate in the red cell

is on the order of 0.045 s [151]. The half-time for the exchange of HCO3 out of the red cell to reach electrochemical equilibrium is 0.1 s [151]. The characteristic time of diffusion of dissolved CO_2 to the fiber membrane wall can be estimated as $t \sim \frac{\delta_{BL}^{\ 2}}{D_{CO2}}$ where δ_{BL} is the thickness of the boundary layer adjacent to the fiber wall. This thickness has been estimated to be approximately 10 μm [32] resulting in a characteristic diffusion time of 0.4 s, an order of magnitude longer than the hydration of CO_2 and the same order of magnitude as diffusion of HCO3 across the membrane wall. Although 0.1 s is not much less than 0.4 s, the assumption of equilibrium appears to be valid in the application of CO_2 removal by hollow fiber membranes. Sufficient time is therefore available for HCO3 to move rapidly across the cell membrane and be converted to CO_2 before diffusing to the fiber membrane where it is removed by the sweep gas. The assumption of equilibrium between CO_2 and HCO3 simplifies the model by allowing the diffusion of CO_2 and HCO3 to be incorporated into a facilitated diffusivity.

The value of the exponent on the Reynolds number in the mass transfer correlation varies in the literature. For example, the exponent on the Reynolds number has been reported in the range of 0.4 - 0.6 by several investigators [19, 76, 146]. These values are consistent with the finding of 0.42 in this study. Other investigators have reported exponent values in the range of 0.8 – 1.0 [81, 82, 136]. The discrepancy may be attributed to equilibration between the concentration of gas in the fibers and the dissolved gas in the water for the oxygenators used in the latter studies. If gas exchange rates are high enough for given water flowrate, the partial pressure of gas in

the fiber will equilibrate with the partial pressure of gas in the water. This phenomenon is known as 'flow limited' gas exchange. In the overall gas exchange equation for water: $V = Q\alpha(P_{out} - P_{in})$, P_{out} will not change for flowrates at or below the flow limit. Therefore, gas exchange will be directly proportional to the flowrate of water. As a result, the exponent on the Reynolds number will approach unity (b=1): $\dot{V} \sim k \sim \mathrm{Re}^b \sim Q^b$. The likelihood that gas exchange will be flow limited increases with fiber bundle surface area. The oxygenators used in the latter studies had large surface areas of 2.0 m^2 or greater. The value of 0.8-0.9 for the Reynolds number exponent may indicate that these oxygenators were operating near their flow limit and explain the discrepancy for the value of the Reynolds number exponent.

The CO_2 model presented here provides a method to predict gas exchange in blood oxygenators from gas exchange data obtained in water. We have shown that the mass transfer correlation determined in water collapsed onto a universal curve for O_2 and CO_2, and was also valid for two fiber bundle geometries of different lengths and thicknesses.

10.0 CONCLUSIONS

The goal of this project was to develop a system for removing 100-120 ml/min of CO_2 at blood flowrates of 0.75 L/min or less for the treatment of acute respiratory failure particularly acute exacerbations of COPD. We manufactured three Generations of PRAL devices that incorporated rotation to enhance gas exchange by increasing the relative velocity between the fibers and the fluid. The rotation also enabled the PRAL to pump blood. The Generation III prototype achieved a CO_2 removal rate of 101 ml/min in blood at 0.75 L/min thus meeting the target. This research has lead to the following conclusions:

- The resistance of the fiber bundle creates uniform radial flow regardless of the diffuser design.
- Blood is entrained in the fiber bundle during rotation leading to low relative angular velocity.
- Rotation of the PRAL fiber bundle creates Taylor vortices between the bundle and stationary outer housing.
- The vortices cause enhanced mixing between the fluid in the outer gap and the fluid in the fiber bundle resulting in increased gas exchange with rotation for all layers of the fiber bundle.
- In vitro hemolysis in the PRAL was substantially higher than a commercially available control oxygenator.

- The blood contacting seals were not the main source of hemolysis in the PRAL.

- The roughness of the fiber bundle causes increased shear stress in the outer gap resulting in high hemolysis levels compared to a smooth cylinder.

The PRAL device is currently being commercialized by Alung Technologies, Inc. and has been redesigned and renamed the Hemolung. The Hemolung contains a rotating core and a stationary fiber bundle. Preclinical data has been encouraging with comparable gas exchange to the PRAL, and hemolysis levels are comparable to a control oxygenator.

APPENDIX

The following is a derivation of the convection-diffusion equations for CO_2 in a blood continuum. The flowrate of dissolved CO_2 and bound CO_2 (bicarbonate and CO_2 bound to hemoglobin) due to convection through a differential element, dA can be expressed as:

$$C^d_{CO2} V_b \bullet ndA + C^b_{CO2} V_b \bullet ndA \quad \textbf{(A.1)}$$

The flowrate of dissolved (free) CO_2 and CO_2 stored as HCO3 due to diffusion through dA is:

$$- D_{CO2} \nabla C^d_{CO2} \bullet ndA - D_{HCO3} \nabla C_{HCO3} \bullet ndA \quad \textbf{(A.2)}$$

CO_2 bound to hemoglobin will have low diffusion capacity due to the large size of the hemoglobin molecule. The total flowrate of CO_2 through a differential volume element dV as dV → 0 is:

$$V_b \bullet \left(\nabla C^d_{CO2} + \nabla C^b_{CO2} \right) = D_{CO2} \nabla^2 C^d_{CO2} + D_{HCO3} \nabla^2 C_{HCO3} \quad \textbf{(A.3)}$$

The dissolved component of CO_2 will obey Henry's law and can be expressed in terms of partial pressure and solubility (α):

$$C^d_{CO2} = \alpha P_{CO2} \quad \textbf{(A.4)}$$

Using the chain rule and rearranging gives the transport equation for CO_2 in blood:

$$V_b \bullet \left(1 + \frac{1}{\alpha} \frac{\partial C^b_{CO2}}{\partial P} \right) \nabla P = \nabla \bullet \left(D_{CO2} + \frac{D_{HCO3}}{\alpha} \frac{\partial C_{HCO3}}{\partial P} \right) \nabla P \quad \textbf{(A.5)}$$

The right hand side of Eqn A.5 is the diffusion of dissolved CO_2 and HCO_3 and the left hand side is the convection of CO_2 in all forms. The term in parenthesis on the right hand side is a facilitated diffusion coefficient:

$$D_f = D_{CO2} + \frac{D_{HCO3}}{\alpha}\frac{\partial C_{HCO3}}{\partial P} \quad \textbf{(A.6)}$$

The convective-diffusion equation for CO_2 can be obtained by dividing the right hand side of Eqn A.5 by $1+\frac{1}{\alpha}\frac{\partial C^b_{CO2}}{\partial P}$ assuming a constant value for $\frac{\partial C^b_{CO2}}{\partial P}$:

$$V_b \bullet \nabla P = D_{eff}\nabla^2 P \quad \textbf{(A.7)}$$

The convective-diffusion equation leads to the definition of the effective diffusivity:

$$D_{eff} = \frac{D_{CO2} + \frac{D_{HCO3}}{\alpha}\frac{\partial C_{HCO3}}{\partial P}}{1+\frac{1}{\alpha}\frac{\partial C^b_{CO2}}{\partial P}} \quad \textbf{(A.8)}$$

Nondimensionalizing the governing equations provides insight as to why the effective diffusivity is used in the Schmidt number and the facilitated diffusivity is used in the Sherwood number. Letting $P^* = \frac{P}{P_c}, \nabla^* = d_h\nabla, V^* = \frac{V}{V_c}$ and substituting these definitions into Eqn A.9 leads to the dimensionless transport equation:

$$V^* \bullet \nabla^* P^* = \frac{D_{eff}}{d_h V_c}\nabla^{*2} P^* \quad \textbf{(A.9)}$$

The dimensionless group $\frac{D_{eff}}{d_h V_c}$ is the Peclet number. The solution to the convection-diffusion equation requires solving for the velocity in the Navier-Stokes equations.

Dimensional analysis on the Navier-Stokes equations for fluid motion leads to the definition for the Reynolds number, $\mathrm{Re} = \frac{Vd_h}{\nu}$. The coupling of the dimensionless Navier-Stokes equations and dimensionless convection-diffusion equations leads to a third dimensionless parameter, the Schmidt number:

$$Sc = \frac{Pe}{\mathrm{Re}} = \frac{\nu}{D_{eff}} \qquad \textbf{(A.10)}$$

The solution to the convective diffusion equation requires a boundary condition at the surface of the fibers. The flux across the fiber wall is due to the diffusion of dissolved CO_2 and bicarbonate ions. As the dissolved CO_2 is removed by the fibers, the bicarbonate is rapidly converted to CO_2 through the action of the enzyme carbonic anhydrase. At the fiber surface, the diffusional flux is:

$$N_{CO2} = -\alpha D_f \nabla P = k(P_{CO2} - P_{G\_CO2}) \qquad \textbf{(A.11)}$$

By introducing the dimensionless variables defined above with $P_c = P_{CO2} - P_{G\_CO2}$, the flux equation becomes:

$$-\frac{\alpha D_f}{d_h} \nabla^* P^* (P_{CO2} - P_{G\_CO2}) = k(P_{CO2} - P_{G\_CO2}) \qquad \textbf{(A.12)}$$

After rearranging, both sides become dimensionless and the left side of the equation is the definition of the Sherwood number, which incorporates the facilitated diffusivity.

$$Sh \equiv \frac{kd_h}{\alpha D_f} = \nabla^* P^* \qquad \textbf{(A.13)}$$

BIBLIOGRAPHY

1. ***Data and statistics*****. 2004 [cited Feb. 2005]; Available from: http://www.lungusa.org/site/pp.asp?c=dvLUK9O0E&b=33347.**

2. **Halbert, R.J., et al., *Interpreting COPD prevalence estimates: what is the true burden of disease?* Chest, 2003. 123(5): p. 1684-92.**

3. **Mannino, D.M., et al., *Chronic obstructive pulmonary disease surveillance--United States, 1971-2000.* MMWR Surveill Summ, 2002. 51(6): p. 1-16.**

4. ***Strategies in preserving lung health and preventing COPD and associated diseases. The National Lung Health Education Program (NLHEP).* Chest, 1998. 113(2 Suppl): p. 123S-163S.**

5. **Petty, T.L., *COPD in perspective.* Chest, 2002. 121(5 Suppl): p. 116S-120S.**

6. **Warren, P.M., et al., *Respiratory failure revisited: acute exacerbations of chronic bronchitis between 1961-68 and 1970-76.* Lancet, 1980. 1(8166): p. 467-70.**

7. **Niederman, M.S., *Introduction: mechanisms and management of COPD: we can do better--it's time for a re-evaluation.* Chest, 1998. 113(4 Suppl): p. 233S-234S.**

8. **Davidson, A.C., *The pulmonary physician in critical care. 11: critical care management of respiratory failure resulting from COPD.* Thorax, 2002. 57(12): p. 1079-84.**

9. **Hirvela, E.R., *Advances in the management of acute respiratory distress syndrome: protective ventilation.* Arch Surg, 2000. 135(2): p. 126-35.**

10. **Plant, P.K. and M.W. Elliott, *Chronic obstructive pulmonary disease * 9: management of ventilatory failure in COPD.* Thorax, 2003. 58(6): p. 537-42.**

11. **Sethi, J.M. and M.D. Siegel, *Mechanical ventilation in chronic obstructive lung disease.* Clin Chest Med, 2000. 21(4): p. 799-818.**

12. **Soto, F.J. and B. Varkey, *Evidence-based approach to acute exacerbations of COPD.* Curr Opin Pulm Med, 2003. 9(2): p. 117-24.**

13. **Peigang, Y. and J.J. Marini, *Ventilation of patients with asthma and chronic obstructive pulmonary disease.* Curr Opin Crit Care, 2002. 8(1): p. 70-6.**

14. **Gammon, R.B., M.S. Shin, and S.E. Buchalter, *Pulmonary barotrauma in mechanical ventilation. Patterns and risk factors.* Chest, 1992. 102(2): p. 568-72.**

15. **Amato, M.B., et al., *Effect of a protective-ventilation strategy on mortality in the acute respiratory distress syndrome.* N Engl J Med, 1998. 338(6): p. 347-54.**

16. **Kollef, M.H., *Non-invasive ventilation for chronic obstructive pulmonary disease.* Lancet, 2000. 356(9234): p. 956-7.**

17. **Heyland, D.K., et al., *The attributable morbidity and mortality of ventilator-associated pneumonia in the critically ill patient. The Canadian Critical Trials Group.* Am J Respir Crit Care Med, 1999. 159(4 Pt 1): p. 1249-56.**

18. **Ibrahim, E.H., et al., *The occurrence of ventilator-associated pneumonia in a community hospital: risk factors and clinical outcomes.* Chest, 2001. 120(2): p. 555-61.**

19. **Federspiel, W.J., T.J. Hewitt, and B.G. Hattler, *Experimental evaluation of a model for oxygen exchange in a pulsating intravascular artificial lung.* Ann Biomed Eng, 2000. 28(2): p. 160-7.**

20. **Golob, J.F., et al., *Acute in vivo testing of an intravascular respiratory support catheter.* Asaio J, 2001. 47(5): p. 432-7.**

21. **Makarewicz, A.J., L.F. Mockros, and R.W. Anderson, *A dynamic intravascular artificial lung.* ASAIO Journal, 1994. 40(3): p. M747-750.**

22. **Makarewicz, A.J., L.F. Mockros, and C. Mavroudis, *New design for a pumping artificial lung.* ASAIO Journal, 1996. 42(5): p. M615-619.**

23. **Vaslef, S.N., L.F. Mockros, and R.W. Anderson, *Development of an intravascular lung assist device.* ASAIO Trans, 1989. 35(3): p. 660-4.**

24. **Boschetti, F., et al., *Blood flow pulsatility effects upon oxygen transfer in artificial lungs.* Asaio J, 2003. 49(6): p. 678-86.**

25. **Mortensen, J.D., *An intravenacaval blood gas exchange (IVCBGE) device. A preliminary report.* ASAIO Transactions, 1987. 33(3): p. 570-573.**

26. **Mortensen, J.D., *Intravascular oxygenator: a new alternative method for augmenting blood gas transfer in patients with acute respiratory failure.* Artificial Organs, 1992. 16(1): p. 75-82.**

27. **Charoenkul, V., F. Giron, and E.C. Peirce, 2nd, *Respiratory support with a paracorporeal membrane oxygenator.* J Surg Res, 1973. 14(5): p. 393-9.**

28. **Lick, S.D., et al., *Paracorporeal artificial lung: perioperative management for survival study in sheep.* J Invest Surg, 2003. 16(3): p. 177-84.**

29. **Zwischenberger, J.B., et al., *The paracorporeal artificial lung improves 5-day outcomes from lethal smoke/burn-induced acute respiratory distress syndrome in sheep.* Ann Thorac Surg, 2002. 74(4): p. 1011-6; discussion 1017-8.**

30. **Zwischenberger, J.B. and R.H. Bartlett, *ECMO*. 1995: Extracorporeal Life Support Organization. 28.**

31. **Loeppky, J.A., U.C. Luft, and E.R. Fletcher, *Quantitative description of whole blood CO2 dissociation curve and Haldane effect.* Respir Physiol, 1983. 51(2): p. 167-81.**

32. **Vaslef, S. and R. Anderson, *The Artificial Lung*. 1 ed. Gas Exchange in the Venous System: Support for the Failing Lung. 2002, Georgetown: Landes Bioscience.**

33. **Zwischenberger, J.B., et al., *IVOX with gradual permissive hypercapnia: a new management technique for respiratory failure.* J.Surg.Res., 1994. 57(1): p. 99-105.**

34. **Cattaneo, G., A. Strauss, and H. Reul, *Compact intra- and extracorporeal oxygenator developments.* Perfusion, 2004. 19(4): p. 251-5.**

35. **Cattaneo, G.F. and H. Reul, *New fiber configuration for intravenous gas exchange.* Int J Artif Organs, 2005. 28(3): p. 244-50.**

36. **Cattaneo, G.F., et al., *Intravascular blood oxygenation using hollow fibers in a disk-shaped configuration: experimental evaluation of the relationship between porosity and performance.* Asaio J, 2006. 52(2): p. 180-5.**

37. **Zwischenberger, J.B., et al., *Intravascular membrane oxygenation and carbon dioxide removal with IVOX: can improved design and permissive hypercapnia***

achieve adequate respiratory support during severe respiratory failure? **Artif Organs, 1994. 18(11): p. 833-9.**

38. **Zwischenberger, J.B., W. Tao, and A. Bidani, *Intravascular membrane oxygenator and carbon dioxide removal devices: a review of performance and improvements.* Asaio J, 1999. 45(1): p. 41-6.**

39. **Gattinoni, L., et al., *Hemodynamics and renal function during low frequency positive pressure ventilation with extracorporeal CO2 removal. A comparison with continuous positive pressure ventilation.* Intensive Care Med, 1980. 6(3): p. 155-61.**

40. **Gattinoni, L., et al., *Treatment of acute respiratory failure with low-frequency positive-pressure ventilation and extracorporeal removal of CO2.* Lancet, 1980. 2(8189): p. 292-4.**

41. **Gattinoni, L., G. Iapichino, and T. Kolobow, *Hemodynamic, mechanical and renal effects during "apneic oxygenation" with extracorporeal carbon dioxide removal, at different levels of intrapulmonary pressure in lambs.* Int J Artif Organs, 1979. 2(5): p. 249-53.**

42. **Gattinoni, L., et al., *Clinical application of low frequency positive pressure ventilation with extracorporeal CO2 removal (LFPPV-ECCO2R) in treatment of adult respiratory distress syndrome (ARDS).* Int J Artif Organs, 1979. 2(6): p. 282-3.**

43. **Gattinoni, L., et al., *Low-frequency positive pressure ventilation with extracorporeal carbon dioxide removal (LFPPV-ECCO2R): an experimental study.* Anesth Analg, 1978. 57(4): p. 470-7.**

44. **Gattinoni, L., et al., *Control of intermittent positive pressure breathing (IPPB) by extracorporeal removal of carbon dioxide.* Br J Anaesth, 1978. 50(8): p. 753-8.**

45. **Kolobow, T., et al., *Control of breathing using an extracorporeal membrane lung.* Anesthesiology, 1977. 46(2): p. 138-41.**

46. **Kolobow, T., et al., *A new approach to the prevention and treatment of acute pulmonary insufficiency.* Int J Artif Organs, 1980. 3(2): p. 86-93.**

47. **Kolobow, T., et al., *The prevention of hyaline membrane disease (HMD) in the preterm fetal lamb through the static inflation of the lungs: the conditioning of the fetal lungs.* Trans Am Soc Artif Intern Organs, 1980. 26: p. 567-72.**

48. **Pesenti, A., et al., *Low frequency positive pressure ventilation with extracorporeal CO2 removal (LEPPV-ECCO2R) in acute respiratory failure (ARF): technique.* Trans Am Soc Artif Intern Organs, 1981. 27: p. 263-6.**

49. **Wang, D., et al., *Toward ambulatory arteriovenous CO2 removal: initial studies and prototype development.* Asaio J, 2003. 49(5): p. 564-7.**

50. **Zwischenberger, J.B., et al., *Percutaneous extracorporeal arteriovenous CO2 removal for severe respiratory failure.* The Annals of Thoracic Surgery, 1999. 68(1): p. 181-187.**

51. **Conrad, S.A., et al., *Total extracorporeal arteriovenous carbon dioxide removal in acute respiratory failure: a phase I clinical study.* Intensive Care Medicine, 2001. 27(8): p. 1340-51.**

52. **Jegger, D., et al., *Ex vivo evaluation of a new extracorporeal lung assist device: NovaLung membrane oxygenator.* Int J Artif Organs, 2005. 28(10): p. 985-99.**

53. **Zhou, X., et al., *Seventy-two hour gas exchange performance and hemodynamic properties of NOVALUNG iLA as a gas exchanger for arteriovenous carbon dioxide removal.* Perfusion, 2005. 20(6): p. 303-8.**

54. **Roberts, N., et al., *Venovenous extracorporeal membrane oxygenation for respiratory failure in inotrope dependent neonates.* Asaio J, 2003. 49(5): p. 568-71.**

55. **Zwischenberger, J.B., et al., *Complications of neonatal extracorporeal membrane oxygenation. Collective experience from the Extracorporeal Life Support Organization.* J Thorac Cardiovasc Surg, 1994. 107(3): p. 838-48; discussion 848-9.**

56. **Niimi, Y., et al., *The effects of heparin coating of oxygenator fibers on platelet adhesion and protein adsorption.* Anesth Analg, 1999. 89(3): p. 573-9.**

57. **Niimi, Y., et al., *Platelet adhesion to heparin coated oxygenator fibers under in vitro static conditions: impact of temperature.* Asaio J, 2001. 47(4): p. 361-4.**

58. **Niimi, Y., et al., *Protein adsorption and platelet adhesion on the surface of an oxygenator membrane.* Asaio J, 1997. 43(5): p. M706-10.**

59. **Takami, Y., et al., *Evaluation of platelet adhesion and activation on materials for an implantable centrifugal blood pump.* Artif Organs, 1998. 22(9): p. 753-8.**

60. **Federspiel, W.J., et al., *Ex vivo testing of the intravenous membrane oxygenator.* Asaio J, 2000. 46(3): p. 261-7.**

61. **Hattler, B.G., et al., *Development of an intravenous membrane oxygenator: A new concept in mechanical support of the failing lung.* The Journal of Heart and Lung Transplantation, 1994. 13: p. 1003-1008.**

62. **Hattler, B.G., et al., *Development of an intravenous membrane oxygenator (IMO): Enhanced intravenous gas exchange through convective mixing of blood around hollow fiber membranes.* Artificial Organs, 1994. 18(11): p. 806-812.**

63. **Svitek, R.G., B.J. Frankowski, and W.J. Federspiel, *Evaluation of a pumping assist lung that uses a rotating fiber bundle.* Asaio J, 2005. 51(6): p. 773-80.**

64. **Gaylor, J.D., et al., *Gas transfer and thrombogenesis in an annular membrane oxygenator with active blood mixing.* Trans Am Soc Artif Intern Organs, 1973. 19: p. 516-24.**

65. **Hill, J.D., et al., *Technique for achieving high gas exchange rates in membrane oxygenation.* Trans Am Soc Artif Intern Organs, 1974. 20A: p. 249-52.**

66. **Lewis, F.R., J.A. Tylke, and H.S. Winchell, *A combined membrane pump-oxygenator: design and testing.* Trans Am Soc Artif Intern Organs, 1974. 20A: p. 253-60.**

67. **Astolfi, D. and I. Christlieb, *[Artificial heart-lung: method of its preparation and assembling. I. Disk oxygenator (Kay-Cross) machines].* Cir Ginecol Urol, 1965. 19(3): p. 218-24.**

68. **Dietmann, K., et al., *[Construction principles and mechanism of action of a rotating disk oxygenator.].* Thoraxchirurgie, 1962. 9: p. 516-29.**

69. **Gille, J.P., et al., *[Extracorporeal purification of carbon dioxide: efficiency of a disk oxygenator during experimental hypercapnia].* Pathol Biol (Paris), 1969. 17(7): p. 371-7.**

70. **Makarewicz, A.J., L.F. Mockros, and R.W. Anderson, *A pumping artificial lung.* Asaio J, 1994. 40(3): p. M518-21.**

71. **Maloney, J., *Mass and Thermal Transfer Means for Use in Heart Lung Machines, dialyzers, and Other Applications.* USPTO, 1999.**

72. **Wu, Z.J., et al., *Progress toward an ambulatory pump-lung.* J Thorac Cardiovasc Surg, 2005. 130(4): p. 973-8.**

73. **Baldwin, J.T., et al., *The National Heart, Lung, and Blood Institute Pediatric Circulatory Support Program.* Circulation, 2006. 113(1): p. 147-55.**

74. **Mueller, X.M., et al., *A new concept of integrated cardiopulmonary bypass circuit.* Eur J Cardiothorac Surg, 2002. 21(5): p. 840-6.**

75. ***Cardiovascular implants and artificial organs - Blood-gas exchangers oxygenators*, in *AAMI standards and recommended practices: Biomedical equipment, Part 1: General safety and design; Equipment for therapy and surgery*. 1996, American National Standards Institute, Inc. p. 633-648.**

76. **Hewitt, T.J., B.G. Hattler, and W.J. Federspiel, *A mathematical model of gas exchange in an intravenous membrane oxygenator.* Ann Biomed Eng, 1998. 26(1): p. 166-78.**

77. **Perry, R., *Perry's Chemical Engineers' Handbook 7th Ed.* 1997.**

78. ***OriGen biomedical dual lumen catheters*. 2002 [cited Feb. 2005]; Available from: http://www.origenbio.com/cath.html.**

79. **Young, D.F., B.R. Munson, and T.H. Okiishi, *A Brief Introduction to Fluid Mechanics*. 1st ed. 1997, New York: John Wiley & Sons Inc.**

80. **Bird, R.B., W.E. Stewart, and E.N. Lightfoot, *Transport phenomena*. 2nd ed. 2002, New York: J. Wiley. xii, 895.**

81. **Vaslef, S.N., et al., *Use of a mathematical model to predict oxygen transfer rates in hollow fiber membrane oxygenators.* Asaio J, 1994. 40(4): p. 990-6.**

82. **Vaslef, S.N., et al., *Computer-assisted design of an implantable, intrathoracic artificial lung.* Artif Organs, 1994. 18(11): p. 813-7.**

83. **Eash, H.J., et al., *Evaluation of local gas exchange in a pulsating respiratory support catheter.* Asaio J, 2005. 51(2): p. 152-7.**

84. **Budilarto, S.G., et al., *Flow visualization study of a pulsating respiratory assist catheter.* Asaio J, 2005. 51(6): p. 673-80.**

85. **Lueptow, R.M. and A. Hajiloo, *Flow in a rotating membrane plasma separator.* Asaio J, 1995. 41(2): p. 182-8.**

86. **Mizuguchi, K., et al., *Does hematocrit affect in vitro hemolysis test results? Preliminary study with Baylor/NASA prototype axial flow pump.* Artif Organs, 1994. 18(9): p. 650-6.**

87. **Naito, K., K. Mizuguchi, and Y. Nose, *The need for standardizing the index of hemolysis.* Artif Organs, 1994. 18(1): p. 7-10.**

88. **Araki, K., et al., *Hemolysis and heat generation in six different types of centrifugal blood pumps.* Artif Organs, 1995. 19(9): p. 928-32.**

89. **Araki, K., et al., *Heat generation and hemolysis at the shaft seal in centrifugal blood pumps.* Asaio J, 1995. 41(3): p. M284-7.**

90. **Anai, H., et al., *An approach to reducing hemolysis in an axial-flow blood pump.* Asaio J, 1995. 41(3): p. M771-4.**

91. **Wakisaka, Y., et al., *A two stage axial flow pump. New approach to reduction of hemolysis.* Asaio J, 1995. 41(3): p. M584-7.**

92. **Apel, J., et al., *Assessment of hemolysis related quantities in a microaxial blood pump by computational fluid dynamics.* Artif Organs, 2001. 25(5): p. 341-7.**

93. **Arora, D., M. Behr, and M. Pasquali, *A tensor-based measure for estimating blood damage.* Artif Organs, 2004. 28(11): p. 1002-15.**

94. **Arvand, A., M. Hormes, and H. Reul, *A validated computational fluid dynamics model to estimate hemolysis in a rotary blood pump.* Artif Organs, 2005. 29(7): p. 531-40.**

95. **Burgreen, G.W., et al., *Computational fluid dynamics analysis of a maglev centrifugal left ventricular assist device.* Artif Organs, 2004. 28(10): p. 874-80.**

96. **Li, H. and W.K. Chan, *Inverse design and CFD investigation of blood pump impeller.* Crit Rev Biomed Eng, 2000. 28(1-2): p. 75-80.**

97. **Mitoh, A., et al., *Computational fluid dynamics analysis of an intra-cardiac axial flow pump.* Artif Organs, 2003. 27(1): p. 34-40.**

98. **Miyazoe, Y., et al., *Computational fluid dynamics analysis to establish the design process of a centrifugal blood pump: second report.* Artif Organs, 1999. 23(8): p. 762-8.**

99. **Song, X., et al., *Design and transient computational fluid dynamics study of a continuous axial flow ventricular assist device.* Asaio J, 2004. 50(3): p. 215-24.**

100. **Song, X., et al., *Studies of turbulence models in a computational fluid dynamics model of a blood pump.* Artif Organs, 2003. 27(10): p. 935-7.**

101. **Song, X., H.G. Wood, and D. Olsen, *Computational Fluid Dynamics (CFD) study of the 4th generation prototype of a continuous flow Ventricular Assist Device (VAD).* J Biomech Eng, 2004. 126(2): p. 180-7.**

102. **Throckmorton, A.L., et al., *Computational design and experimental performance testing of an axial-flow pediatric ventricular assist device.* Asaio J, 2005. 51(5): p. 629-35.**

103. **Untaroiu, A., et al., *Numerical and experimental analysis of an axial flow left ventricular assist device: the influence of the diffuser on overall pump performance.* Artif Organs, 2005. 29(7): p. 581-91.**

104. **Untaroiu, A., et al., *Computational design and experimental testing of a novel axial flow LVAD.* Asaio J, 2005. 51(6): p. 702-10.**

105. **Watanabe, N., et al., *Simulation of the BP-80 blood pump.* Artif Organs, 2001. 25(9): p. 733-9.**

106. **Yamane, T., et al., *Flow visualization in a centrifugal blood pump with an eccentric inlet port.* Artif Organs, 2004. 28(6): p. 564-70.**

107. **Yano, T., et al., *An estimation method of hemolysis within an axial flow blood pump by computational fluid dynamics analysis.* Artif Organs, 2003. 27(10): p. 920-5.**

108. **Tsukiya, T., et al., *Performance of a newly developed implantable centrifugal blood pump.* Asaio J, 2001. 47(5): p. 559-62.**

109. **Sekine, K., et al., *Development of a magnetic fluid shaft seal for an axial-flow blood pump.* Artif Organs, 2003. 27(10): p. 892-6.**

110. **Lemos, P.A., et al., *Usefulness of percutaneous left ventricular assistance to support high-risk percutaneous coronary interventions.* Am J Cardiol, 2003. 91(4): p. 479-81.**

111. **Vranckx, P., et al., *Clinical introduction of the Tandemheart, a percutaneous left ventricular assist device, for circulatory support during high-risk***

percutaneous coronary intervention. **Int J Cardiovasc Intervent, 2003. 5(1): p. 35-9.**

112. Nakazawa, T., et al., *Development and initial testing of a permanently implantable centrifugal pump.* Artif Organs, 1997. 21(7): p. 597-601.

113. Nakazawa, T., et al., *Hydraulic assessment of the floating impeller phenomena in a centrifugal pump.* Artif Organs, 1997. 21(1): p. 78-82.

114. Aragon, J., et al., *Percutaneous left ventricular assist device: "TandemHeart" for high-risk coronary intervention.* Catheter Cardiovasc Interv, 2005. 65(3): p. 346-52.

115. Giombolini, C., et al., *Percutaneous left ventricular assist device, TandemHeart, for high-risk percutaneous coronary revascularization. A single centre experience.* Acute Card Care, 2006. 8(1): p. 35-40.

116. Pitsis, A.A., et al., *Temporary assist device for postcardiotomy cardiac failure.* Ann Thorac Surg, 2004. 77(4): p. 1431-3.

117. Maruyama, O., et al., *Hemolysis caused by surface roughness under shear flow.* J Artif Organs, 2005. 8(4): p. 228-36.

118. Takami, Y., et al., *Effect of surface roughness on hemolysis in a pivot bearing supported Gyro centrifugal pump (C1E3).* Artif Organs, 1996. 20(11): p. 1155-61.

119. Takami, Y., et al., *Effect of surface roughness on hemolysis in a centrifugal blood pump.* Asaio J, 1996. 42(5): p. M858-62.

120. Takami, Y., et al., *Hemolytic effects of surface roughness of a pump housing in a centrifugal blood pump.* Artif Organs, 1997. 21(5): p. 428-32.

121. Takami, Y., et al., *Hemolytic effect of surface roughness of an impeller in a centrifugal blood pump.* Artif Organs, 1997. 21(7): p. 686-90.

122. van den Berg, T.H., *Smooth and rough boundaries in turbulent Taylor Couette flow.* Physical Review E, 2003. 68: p. 1-5.

123. Van Dyke, M., *An Album of Fluid Motion*. 1982: The Parabolic Press. 176.

124. Lund, L.W., B.G. Hattler, and W.J. Federspiel, *A comparative in vitro hemolysis study of a pulsating intravenous artificial lung.* Asaio J, 2002. 48(6): p. 631-5.

125. Tamari, Y., et al., *The effects of pressure and flow on hemolysis caused by Bio-Medicus centrifugal pumps and roller pumps. Guidelines for choosing a blood pump.* J Thorac Cardiovasc Surg, 1993. 106(6): p. 997-1007.

126. Leverett, L.B., et al., *Red blood cell damage by shear stress.* Biophys J, 1972. 12(3): p. 257-73.

127. Sandza, J.G., Jr., et al., *Subhemolytic trauma of erythrocytes: recognition and sequestration by the spleen as a function of shear.* Trans Am Soc Artif Intern Organs, 1974. 20 B: p. 457-62.

128. Sutera, S.P., P.A. Croce, and M. Mehrjardi, *Hemolysis and subhemolytic alterations of human RBC induced by turbulent shear flow.* Trans Am Soc Artif Intern Organs, 1972. 18(0): p. 335-41, 347.

129. Sutera, S.P. and M.H. Mehrjardi, *Deformation and fragmentation of human red blood cells in turbulent shear flow.* Biophys J, 1975. 15(1): p. 1-10.

130. Paul, R., et al., *Shear stress related blood damage in laminar couette flow.* Artif Organs, 2003. 27(6): p. 517-29.

131. Wereley, S. and R.M. Lueptow, *Velocity field for Taylor-Couette flow with an axial flow.* Physics of Fluids, 1999. 11(12): p. 3637-3649.

132. Lathrop, D.P., J. Fineberg, and H.L. Swinney, *Transition to Shear-Driven Turbulence in Couette-Taylor Flow.* Physical Review A, 1992. 46(10): p. 6390-6405.

133. Smith, G.P. and A.A. Townsend, *Turbulent Couette flow between concentric cylinders at large Taylor numbers.* J. Fluid Mech., 1982. 123: p. 187-217.

134. Koeltzsch, K., et al., *Drag reduction using surfactants in a rotating cylinder geometry.* Experiments in Fluids, 2003. 34(4): p. 515-530.

135. Federspiel, W., et al., *Temporary support of the lungs: The artificial lung*, in *The transplantation and replacement of thoracic organs*, D.K.C. Cooper, L.W. Miller, and G.A. Patterson, Editors. 1996, Kluwer Academic Publishers: Boston. p. 717-728.

136. Mockros, L.F. and R. Leonard, *Compact cross-flow tubular oxygenators.* Trans Am Soc Artif Intern Organs, 1985. 31: p. 628-33.

137. Wickramasinghe, S.R., et al., *Designing blood oxygenators.* Ann N Y Acad Sci, 2003. 984: p. 502-14.

138. Dierickx, P.W., D. De Wachter, and P.R. Verdonck, *Blood flow around hollow fibers.* Int J Artif Organs, 2000. 23(9): p. 610-7.

139. Gage, K.L., et al., *Predicting membrane oxygenator pressure drop using computational fluid dynamics.* Artif Organs, 2002. 26(7): p. 600-7.

140. Gartner, M.J., et al., *Modeling flow effects on thrombotic deposition in a membrane oxygenator.* Artif Organs, 2000. 24(1): p. 29-36.

141. Funakubo, A., et al., *Flow vectorial analysis in an artificial implantable lung.* Asaio J, 2003. 49(4): p. 383-7.

142. Yasuda, T., et al., *An investigation of blood flow behavior and hemolysis in artificial organs.* Asaio J, 2000. 46(5): p. 527-31.

143. Kays, W.M. and M.E. Crawford, *Convective heat and mass transfer*. 3rd ed. McGraw-Hill series in mechanical engineering. 1993, New York: McGraw-Hill. xxxii, 601 p.

144. Guyton, A.C., *Basic human physiology: normal function and mechanisms of disease*. 2d ed. 1977, Philadelphia: Saunders. xi, 931 p.

145. Spaeth, E.E., *Blood oxygenation in extracorporeal devices: theoretical considerations.* CRC Crit Rev Bioeng, 1973. 1(4): p. 383-417.

146. Wickramasinghe, S.R., M.J. Semmens, and E.L. Cussler, *Mass transfer in various hollow fiber geometries.* Journal of Membrane Science, 1992. 69(3): p. 235.

147. Forster, R.E., *Diffusion of gases in the lungs.* Physiologist, 1966. 9(2): p. 110-22.

148. Forster, R.E., et al., *Reaction of CO2 with human hemoglobin solution.* J Biol Chem, 1968. 243(12): p. 3317-26.

149. Holland, R.A. and R.E. Forster, 2nd, *Effect of temperature on rate of CO2 uptake by human red cell suspensions.* Am J Physiol, 1975. 228(5): p. 1589-96.

150. MatLab, *Version 6.2.* The MathWorks, 2003.

151. Forster, R.E. and E.D. Crandall, *Time course of exchanges between red cells and extracellular fluid during CO2 uptake.* J Appl Physiol, 1975. 38(4): p. 710-8.